ELECTRON-PARAMAGNETIC-RESONANCE SPECTROSCOPY STUDY OF RADIATION-DAMAGE-INDUCED CATHODOLUMINESCENCE IN QUARTZ, ATHABASCA BASIN

A Thesis Submitted to the College of Graduated Studies and Research in Partial Fulfillment of the Requirements for the Degree of Master in Sciences in the

Department of Geological Sciences

University of Saskatchewan

By

Sanda Botis

2005

Permission to use:

In presenting this thesis in partial fulfillment of the requirements for a Master degree in science from the University of Saskatchewan, I agree that the Libraries of this University may make it freely available for inspection. I further agree that permission for copying of this thesis in any manner, in whole or in part, for scholarly purposes may be granted by the professor or professors who supervised my thesis work, or, in absence, by the Head of the Department or the Dean of the College in which my thesis work was done. It is understood that any copying and publication of this thesis or parts for financial gain shall not be allowed without my written permission. It is also understood that due recognition shall be given to me and to the University of Saskatchewan in any scholarly use which may be made of any material in my thesis.

Request for permission to copy or to make other use of material in this thesis, in whole or in part, should be address to:

Head of the Department of Geological Sciences
University of Saskatchewan
114 Science Place
Saskatoon, Saskatchewan,
S7N 5E2 CANADA

Abstract

This thesis presents the results of a combined cathodoluminescence (CL) and electron paramagnetic resonance (EPR) spectroscopic study of quartz from the uranium-mineralized Athabasca Basin. CL imaging not only distinguishes detrital quartz grains from their secondary overgrowths but also is able to differentiate two generations of overgrowths in the Athabasca sandstones. Moreover, the Athabasca quartz samples are characterized by three types of bright CL: 1) haloes around U- and Th-bearing mineral inclusions, 2) patches associated with U-bearing minerals in matrices or pores and 3) continuous rims in samples with or without any visible U-bearing minerals. These three types of bright CL are all of constant widths of ~35-45 μm, indicative of bombardments of alpha particles emitted from the ^{238}U, ^{235}U and ^{232}Th decay series. CL spectral analyses show that the radiation damaged areas, relative to their undamaged hosts, are characterized by intense but broad emission bands at ~350 nm and 620-650 nm.

Detailed EPR measurements of the Athabasca quartz samples revealed six paramagnetic defects: one oxygen vacancy center (E_1'), three silicon vacancy hole centers (O_2^{3-}/H^+(I), O_2^{3-}/H^+(II) and O_2^{3-}/M^+) and two O_2^- peroxy centers. Moreover, dissolution experiments using concentrated HF showed that that the silicon vacancy hole centers and the peroxy centers are concentrated in the radiation-damaged rims/fractures, whereas the oxygen vacancy center (E_1') is evenly distributed in quartz grains. CL and EPR data of quartz samples after isochronal annealing experiments

suggest that the silicon vacancy hole centers and the peroxy centers are most likely responsible for the characteristic ultraviolet CL and the red CL, respectively.

CL haloes in detrital quartz grains are ubiquitous in the Athabasca sandstones. CL patches are also widespread but are best developed in altered sandstones close to the unconformity or faults/fractures. Continuous CL rims, however, are more restricted in occurrences and are best developed at the high-grade Cigar Lake and McArthur River deposits, where they are restricted to lithological boundaries and faults and are pervasively developed in mineralized samples and associated alteration haloes close to the unconformity. At the Key Lake deposit, continuous rims occur only in mineralized samples close to the unconformity. Continuous CL rims are absent in basement rocks below mineralization, including those at the Cigar Lake and McArthur River deposits. The occurrence of radiation damages in Athabasca quartz have also been confirmed by detailed EPR measurements, which are significantly more sensitive than CL imaging.

Continuous CL rims on Athabasca quartz grains most likely record bombardments of alpha particles emitted from U-bearing mineralization fluids. Therefore, their associations with the unconformity, lithological boundaries and faults provide direct evidence for those structures being the pathways for mineralization fluids. The exclusive occurrence of continuous CL rims on detrital quartz grains and the abundance of U-bearing minerals in both generations of overgrowths suggest that U mineralization must have commenced during early diagenesis and continued during the formation of overgrowths. The absence of significant radiation damages in altered

basement rocks supports the hypothesis that the basement was not a major source for uranium mineralization in the Athabasca basin. The common occurrence of CL haloes in euhedral quartz grains and CL patches associated with U-bearing minerals in faults, fractures and voids provide further (visual) evidence for late remobilization of uranium.

Acknowledgements

The research contained herein could not be carried without the assistance and support of many people.

I would like to thank my supervisor Dr. Pan for his support and guidance and for giving me the opportunity to explore the exciting world of mineralogy. I would like to thank him for being my friend and my family whenever I needed him.

I would like also to express my gratitude to Dr. Sergiy Nokhrin who gave me precious advices in EPR spectroscopy and helped me undergo the complicated problems of spectral simulations.

I would like to thank the technical staff Mr. Tom Bonli and Mr. Blane Novakovski for providing a friendly and cooperative work environment helping me with the sample preparation and analysis.

The funding of this study was provided by the Cameco Corporation and a NSERC Collaborative Research and Development (CRD) grant to Dr. Pan, an NSERC Discovery Grant to Dr. Pan and a University of Saskatchewan graduate scholarship.

TABLE OF CONTENTS

List of tables

List of figures

Chapter 1

Introduction and objectives

Cathodoluminescence (CL) imaging and spectroscopy is a method widely used to characterize mineral specimens from growth zoning to trace impurities, lattice defects and crystal distortions.

The application of CL in mineralogy started in the 1960s when Long and Agreell (1965), Sippel (1965) and Smith and Sternstrom (1965) wrote on the multiple possibilities of using CL for the characterization and better distinction of minerals and mineral modifications.

During the past few decades, CL has often been used to provide spectacular colour images (e.g. zircon for U-Pb geochronological studies), but these images were sometimes over interpreted (Machel, 2000). A good interpretation of CL images as well as the new tendencies of using CL as a quantitative method requires a good understanding of the various causes responsible for CL emission and therefore, fundamental research in this area is essential.

The determination of the nature of the luminescence centers is not, however, a trivial task. Correlations between the observation of specific luminescence bands and

particular impurity concentrations may give an indication of the source of emission but it is not proof of origin and can be sometime misleading. Therefore spectroscopic studies are of great use in determining the origin of the various luminescence emissions, including CL emission.

1.1 Study overview

Cathodoluminescence (CL) colours in quartz have long been applied to petrologic studies (e.g., growth zonation, twinning, fractures and provenance of mineral grains; Smith & Stenstrom 1965; Ramseyer et al. 1988; Owen 1988; Meunier et al. 1990).

Ramseyer et al. (1988) classified the CL colours in quartz into three main categories on the basis of their stability and intensity behaviour during electron bombardment: 1) short-lived violet, blue, blue-green, bottle-green and yellow luminescence colours; 2) long-lived brown luminescence colours with increasing intensity; and 3) long-lived red luminescence colour with an approximately stable intensity.

Surprisingly, perhaps, the mechanisms responsible for the CL colours of quartz are among the least well understood of those of the common minerals. Proposed hypotheses, not mutually exclusive, include:

1) presence of trace elements (Sprunt, 1981; Demars et al. 1996);

2) lattice ordering (Zinkernagel, 1978);

3) occurrence of defect-centres (Mitchell & Denure, 1973);

4) intrinsic properties of the SiO_4 tetrahedron (Hanusiak & White, 1975);

5) radiation damage (Siegel & Marrone 1981).

For example, Ramseyer et al. (1988) suggested that the most likely cause of the brown CL colour is damage to the quartz lattice induced by particle bombardment because artificially produced lattice dislocations or formations of unpaired, non-bonding electrons are known to induce such a luminescence colour. Ramseyer et al. (1988) also proposed that the short-lived blue and bottle-green luminescence colours are probably related to interstitial cations in the c-axis channels of the quartz lattice, whereas the yellow luminescence colour in authigenic quartz was thought to be related to trace elements incorporated during crystallization from oxidizing fluids. Jones & Embree (1976) proposed that a strong luminescence signal in the ultraviolet range at 260 nm is most likely related to a trapped hole in quartz.

Several studies have briefly described radiation-damage-induced CL colours in haloes or rims surrounding U-rich and Th-rich mineral inclusions in quartz (Zinkernagel 1978; Owen 1988; Ramseyer et al. 1988; Meunier et al. 1990). The three major radionuclides, ^{238}U, ^{235}U and ^{232}Th, each involve alpha-decay events causing emission of a ^{4}He core of distinct energies. The coloured haloes surrounding U-rich and Th-rich mineral inclusions in quartz and other minerals (e.g., biotite) have been shown to be related to alpha particle irradiation (Owen 1988; Meunier et al. 1990; Nasdala et al. 2001). For example, Owen (1988) and Meunier et al. (1990) have shown that the diameters of the concentric CL rings in haloes or rims surrounding U-rich and Th-rich minerals are closely related to the power of penetration of the most energetic

particles emitted from the ^{238}U, ^{235}U and ^{232}Th decay series (cf. Bragg & Kleeman 1905). Similarly, Odom & Rink (1989) demonstrated that giant coloured haloes in quartz (see also Laemmlein 1945) could be explained by radiation damage.

Other notable studies on radiation-induced-damages in quartz include Pascucci et al. (1983), Vance et al. (1986) and Martin et al. (1996), although most recent studies on radiation damage in minerals focused on the natural U-rich minerals (e.g., zircon, monazite, titanite, and pyrochlore), because they can provide information about containment of radioactive wastes in refractory phases over geologic times (Pan et al. 1993; Meldrum et al. 1998 and references therein).

More recently, Komuro et al. (2002) performed a high-energy He^{+} (4 MeV) implantation experiment on crystals of synthetic α-quartz, using a 3M-tandem ion accelerator in the Takasaki Research Centre, Japan Atomic Energy Research Institute. Komuro et al.'s (2002) experiment demonstrated that the alpha-particle-irradiated quartz crystals developed the characteristic CL rims with widths consistent with those predicted by Owen (1988). Moreover, Komuro et al. (2002) noted that the intensity of CL in the artificially irradiated quartz increases systematically with the radiation dose. Therefore, there is compelling evidence, both theoretical (Owen 1988) and experimental (Komuro et al. 2002), that CL colours in haloes (patches and rims) surrounding U- and Th-bearing mineral inclusions in quartz are induced by alpha-particle bombardment.

However, several questions remain regarding the nature of alpha-particle-induced radiation damages in quartz and the origin of the characteristic CL emission from the radiation-damaged haloes, patches and rims of this mineral.

The Mesoproterozoic Athabasca Basin of northern Saskatchewan is home to several world-class uranium deposits (including the high-grade McArthur River deposit), which collectively represents approximately 30% of the global production of this strategic metal (Ramaekers 1981; Zhang et al. 2001). As part of a broad study on cathodoluminescence in quartz from the Athabasca Basin, it has been noted that quartz samples from sandstones in this area are characterized by well-developed radiation-damage-induced CL, which occurs not only as haloes surrounding U- and Th-bearing minerals inclusions (e.g., uraninite, zircon and fluorapatite) but also as patches and/or continuous rims along the grain boundaries and fractures. These samples present an excellent opportunity to investigate the nature of radiation-damage in quartz and the mechanism of radiation-damage-induced CL in this mineral.

1.2 Research objectives

This thesis is part of a broad study on radiation-damage-induced cathodoluminescence (CL) in quartz grains associated with uranium deposits in the Athabasca Basin. The main purpose of this thesis is to investigate the nature of radiation damage in Athabasca quartz grains and the mechanism of radiation-damage-induced CL in this mineral through multidisciplinary analytical methods, including CL

microscopy, CL spectroscopy, electron paramagnetic resonance (EPR) spectroscopy and inductively coupled plasma mass spectrometry (ICP-MS).

Over the years, the primary tools for studying defect centers in quartz have been electron paramagnetic resonance spectroscopy and optical absorption spectroscopy. A major advantage of EPR spectroscopy is its ability to detect paramagnetic centers with sensitivity up to 10,000 times that of optical absorption spectroscopy (Rossman 1994). Therefore the analytical method chosen for the present study on the origin of radiation induced CL emission in quartz is EPR spectroscopy.

The EPR characteristics of defects in natural and synthetic quartz have been extensively analyzed and modeled. More than 100 different types of defect centers are known and based on their origin, the defect centers in quartz can be classified into two groups: 1) defects caused by foreign ions (foreign ion centers or interstitial defects) and 2) centers associated with vacant oxygen or vacant silicon positions. Extensive literature on paramagnetic defects in quartz allows a good understanding of the possible intrinsic and extrinsic defect centers in quartz and the experimental conditions that facilitate their observation.

Chapter 2 and 3 of this thesis are a synthesis of the fundamental theory of cathodoluminescence and EPR spectroscopy, with emphasis on application to the study of quartz. For fundamental research on the origin of CL emission, a good understanding of the cathodoluminescence phenomena as well as an understanding of the various radiation-induced defect centers (observed by EPR spectroscopy) is essential.

Specifically, this study reports on a detailed EPR spectroscopic study of radiation-induced paramagnetic centers in a CL-active quartz sample from the McArthur River deposit. Moreover, the present study analyzes the local distribution of radiation-induced centers in quartz, both in the geological profile of uranium mines in the Athabasca Basin, and in the local volume of the naturally irradiated sample.

For the detailed combined CL-EPR study on the origin of radiation-damage-induced CL quartz separates of a selected sample from the McArthur River deposit have been subjected to systematic isochronal annealing experiments and HF treatments followed by investigation by CL (imaging and spectroscopy) and EPR measurements. In particular, EPR experiments on the sample annealed at various temperatures were made using various microwave powers in order to characterize the radiation-induced paramagnetic defects on the basis of their saturation behaviour and thermal properties. Moreover, a comparison of the CL spectra and the thermal behaviours of the observed paramagnetic centers, together with compositional data from an inductively coupled plasma mass-spectrometry (ICP-MS) analysis, permitted correlations of the radiation-damaged-induced CL with specific paramagnetic centers.

The distribution of the radiation-induced centres in quartz samples from the Athabasca Basin has been studied using 31 samples from 3 different uranium mines and various depths throughout the basin. Recording irradiation events from U and Th decay series, the distribution of defect centers in the Athabasca Basin follows the pathway of the U-rich hydrothermal fluids offering new information on the genesis of these uranium deposits.

The local distribution of radiation-damage induced centers in a sample volume has been studied by an HF dissolution experiment. The distribution of the paramagnetic centers in the sample volume offers valuable information concerning alpha-particle irradiation providing additional information for solving the problem of correlation between the presence of specific paramagnetic defects and the various CL colours.

The sample preparation techniques are described in chapter 4 along with the chemical characterization of the sample selected for detailed investigation.

Chapter 5 and 6 present the results of the cathodoluminescence study and EPR analysis describing in detail the subsequent steps followed for a complete characterization of the causes responsible for the various CL emission bands of the radiation-damaged areas. The distribution of the radiation-induced centers is described by both CL and EPR analysis and emphasis is placed on correlation between the results of the two methods.

The primary results of this study and their geological implications are discussed in chapter 7 and 8. The correlation between the different cathodoluminescence emission types and the various defect centers is presented with emphasis on the thermal behavior of the analyzed samples. The origin of radiation-damage-induced CL in quartz, the distribution of the radiation damages and the implications for uranium mineralization in the Athabasca Basin is also discussed.

Chapter 2

Fundamentals of cathodoluminescence

Cathodoluminescence (CL) is one of the most common luminescence phenomena used for studying rocks and minerals in thin sections and can provide information that is not obtainable by any other available analytical techniques.

Cathodoluminescence of quartz is of particular importance due to the great abundance of this mineral in nature and its multiple technological applications.

Despite the extensive use of cathodoluminescence in geology, and the numerous studies existent on cathodoluminescence in silicates, the origin (and causes) of the various CL colours in quartz remains poorly understood.

2.1 Physics of cathodoluminescence

Conventional petrographic examination of geological samples makes use of the interaction of light with the mineral, either transmitted trough the mineral or reflected from the polished surface.

Cathodoluminescence is an additional way of looking at minerals in thin sections. The primary source of excitation in this case is an energetic electron beam and the response of the sample is in general emission of light.

The interaction of the electron beam with the sample results in a number of physical processes: the emission of secondary electrons (SE), back-scattered electrons (BSE), electron absorption ("sample current"), characteristic X-ray, and CL emission (Fig. 2.1). Much of the incident beam energy also goes in heating the sample.

The beam energy is at maximum at the point of entry and decrease with distance within the solid. At a certain distance within the solid, the energy will be at the optimum range for each of the mentioned processes.

The penetration depth of electrons and therefore their excitation depth depend on the energy of source (10-20 keV) and are in the range of 1-2 μm (Marshall 1988).

The cathodoluminiscence process

The basic cathodoluminescence phenomena imply the excitation of an electron to a higher state of energy. The electron remains just for a short period of time in this excited state, and then returns to a lower state of energy emitting a photon in the process.

The luminescence process in a crystal is very complex. Instead of having discrete energy levels, as in the case of free atoms, the available energy states form bands. In insulators the electrons in the valence band are separated by a large gap from the conduction band. In conductors, the valence band and the conduction band overlap significantly.

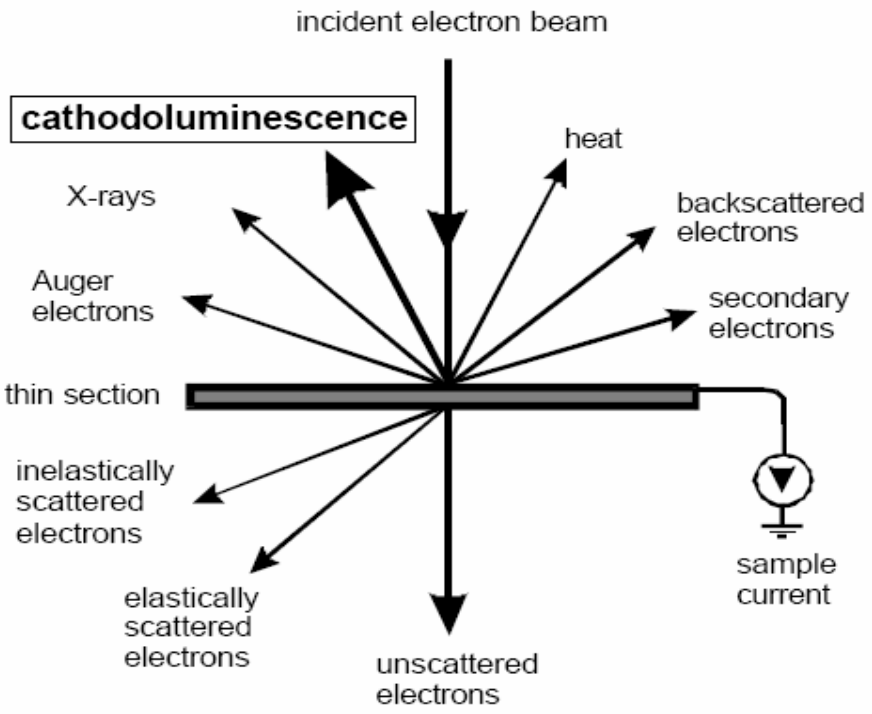

Figure 2.1: Schematic representation of the cathodoluminescence process (modified after Potts et al. 1995).

In quartz, which is a semiconductor, there is a small enough gap between the valence band and the conduction band that thermal and other excitation can bridge it. This gap is called the forbidden zone.

A precondition for cathodoluminescence is the existence of activators (lattice defects or impurities), which have energy levels in the forbidden zone and therefore increase the conductivity and change the optical properties of the crystal.

The luminescence centers can therefore be characterized by their energetic location in the forbidden zone and divided into electron traps near the conduction band (donor level) and recombination sites in the vicinity of the valence band (acceptor level) (Marfunin 1979).

When an energetic electron beam impinges on a solid an electron is excited from the ground state to a higher energy level. From this high-energy level, the electron will relax to a lower, more stable energy state through different possible mechanisms, depending on the specific luminescence centers present in the crystalline structure.

This electron can suffer a recombination or can even be trapped by a luminescent or non-luminescent center (Fig. 2.2.a). In the case of a radiative transition, a photon with energy hν is emitted. The trapped electron can be further on stimulated either thermally or optically to the conduction band and then recombine with an activator (Fig. 2.2.b). If the energy difference between the trap and the activator is small, a direct luminescent transition of the electron is possible (Fig. 2.2.c). The particular activator can also suffer excitation to several energy levels and multiple

luminescent relaxations as a consequence. All these transitions can give rise to emissions in the visible range of the spectrum and therefore constitute the basic of the cathodoluminescence phenomena.

Cathodoluminescence emission can result from a variety of defects in the crystal, like structural imperfection, poor ordering, radiation damage, shock damage, or impurities, defects that are playing the role of activators or recombination centers depending on their energetic properties.

Depending on the type of defects present in the crystalline structure, a general classification divides luminescence into two: a) intrinsic CL, which is characteristic to the crystal structure and b) extrinsic CL, which results from impurities.

2.1.1 Intrinsic luminescence

By definition, the intrinsic luminescence is produced by structural defects of a very pure crystalline lattice.

Many authors (e.g. Hall & Ribbe 1971, Sippel 1971) have discussed the causes of intrinsic luminescence, especially the intrinsic luminescence of silicates. They stated that an intrinsic luminescence in the blue region is common to nearly all silicates.

Even though the broad band in the blue region is often observed in feldspar and quartz, there are, however, many examples of authigenic quartz and authigenic feldspar that posess only a very weak CL.

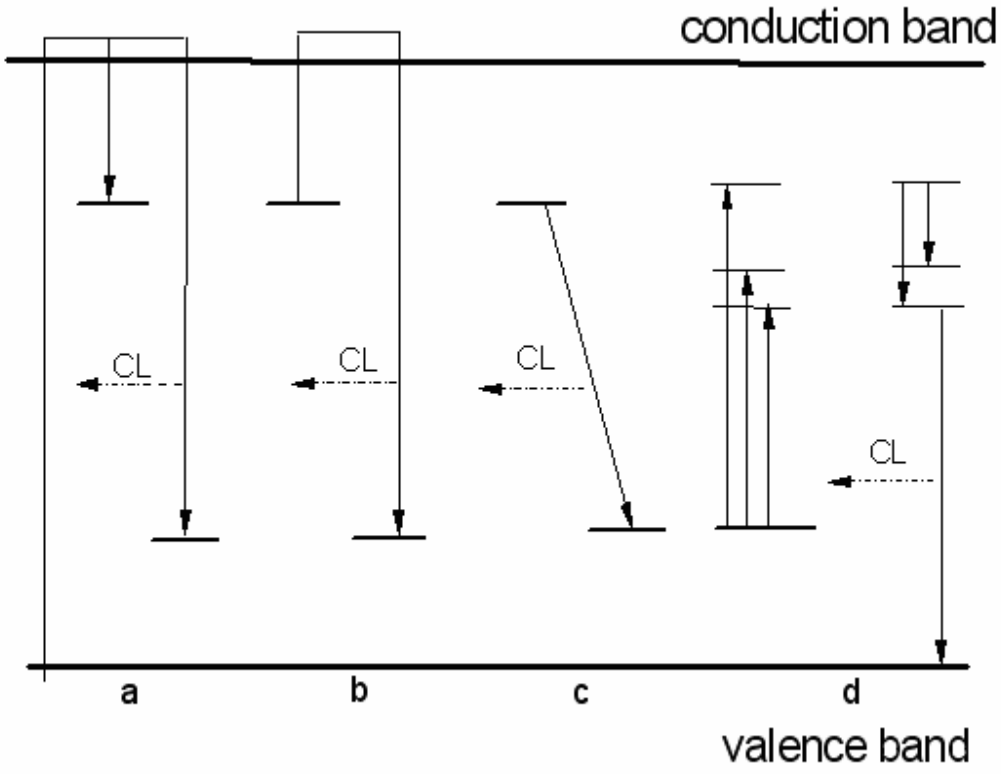

Figure 2.2: Process of charge transfer and luminescence production in crystals after Krbetschek et al. (1997).

These authigenic minerals are formed under conditions of low temperature and slow crystallization, which favor the production of a more perfect lattice with low impurity levels. One conclusion drawn from these cases is that an ideal, pure crystal is not luminescent.

However where there is a crystal imperfection, due to any cause, the disturbed lattice has energy levels different from the pure unperturbed crystal. The presence of the additional energy levels will therefore give rise to luminescence.

The intrinsic luminescence is enhanced by non-stoichiometry and structural imperfections (radiation damage, shock damage) that distort the crystal lattice.

2.1.2 Extrinsic luminescence

The extrinsic luminescence is produced by the presence of impurities, which are responsible for the additional energy levels in the crystal structure. These types of impurities are called activators.

There is also the possibility, especially in geological samples that more than one activator impurities are present.

Also, some materials show luminescence only when two different impurities are present. In this case the terms “co-activators” or “sensitizes” are used (e.g. Pb and Mn in minerals like calcite; Robbins 1983). In this particular case of luminescence the sensitizer needs the presence of an activator to create a luminescence center. In the presence of the sensitizer, the activator is excited to a higher state of energy and a so-called sensitized luminescence is created.

The intensity of the CL spectrum increases with the concentration of the activators up to a maximum level and then decreases. The decrease in intensity with increasing concentrations of activators is called quenching (self-quenching). Some of the most important quenchers in minerals are Fe^{2+}, Fe^{3+}, Co^{2+} and Ni^{3+}.

The quenchers play a complete opposite role to that of activators. These elements modify the energy level arrangement so that the luminescence process does not operate or is very inefficient. But in order to be effective, the quencher must be incorporated in the solid as a substitutional or interstitial impurity and not in a coexisting mineral phase.

The quenching by ions with intense charge transfer bands influences the visible and near ultraviolet (UV) spectral ranges, while luminescence emission in the infrared (IR) region is less affected. The small influence of quenchers on the IR emission is attributed to the creation of new closely spaced energy levels so that the electron can easily relax to the ground state with the emission of a low energy photon (IR) or by heat transfer (Marshall 1988).

Quenching due to lattice defects is also possible. Lattice defects that occur as a result of irradiation, mechanical stress or growth defects can create new energy levels between the conduction band and the valence band resulting in non-luminescent energy transfer or low frequency emission.

Another factor that can induce quenching is temperature. Leverentz (1968) noted that the effect of increasing temperature could be in either direction, being able to increase or decrease the intensity of CL emission, depending on the mineral

composition. In most cases temperature behaves as a quencher and the process is called thermo-quenching. The process of thermo-quenching occurs due to the release of electrons as a result of heating

Moreover, changes in the crystal field properties like local symmetry, coordination number or field strength influence the positions of the energetic levels of the activator elements and also the splitting in closely spaced energy levels of the sensitizer. Therefore a CL spectrum is not a characteristic of the activator but a characteristic of the mineral that crystallized under specific conditions and underwent specific geological histories.

2.2 Cathodoluminescence of quartz

Quartz is one of the most abundant minerals in the Earth's crust occurring in large amounts in almost all crystalline rock types and in various ore deposits.

The great interest concerning luminescence studies of quartz is based on the fact that this mineral has a wide range of technological and industrial applications and that information not available by other analytical methods can be obtained.

The close relationship between physico-chemical properties and luminescence characteristics is the basis for revealing different growth generations, internal structures or distribution of trace elements within quartz. The defects causing the different CL emissions in quartz often reflect the specific physico-chemical conditions of crystal growth and therefore, can be used as a signature of genetic conditions of mineral formation.

The search for the causes of CL in silicates started as early as the beginning of last century and is still under way.

The difficulty in determining the causes of CL in silicates is that it may result from any combination of many factors, including: a large set of possible activator elements, variable chemistry, polymorphyism, and non-identical structural sites for an element, substitution of silica by hydrogen and defect structures such as broken Si-O bonds, oxygen vacancies and radiation-induced defects. Most of these parameters are difficult to quantify on a micron scale at parts-per-million (ppm) or lower concentrations.

The observations of cathodoluminescence phenomena in quartz have had a long history, providing valuable information for the study of cathodoluminescence origin.

Smith and Stenstrom (1965) observed both red- and blue-luminescing quartz. They noted that the CL of authigenic quartz is much duller than that of blue-luminescing detrital grains and thought the latter may have originated in igneous rocks formed at elevated temperatures.

The same authors also noted an example of a quartz grain that luminesced blue except for a central region with red CL. The red-luminescing region contained zircon and they inferred that the CL change was due to radiation damage from thorium associated with the zircon inclusion.

Three years later, Sippel (1968), in a comprehensive article on sandstone petrology, reported that red and blue dull colours were most common in quartz from

sandstones. He observed the dull or nonluminescent properties of authigenic quartz and reported that the blue-luminescing quartz has never been seen as overgrowths.

Secondary (authigenic) quartz that grows in optical continuity with detrital grains has been identified historically by the presence of such features as bubbles or dust, collected along the rims or detrital cores. These features are sometimes difficult to see and equivocal in interpretation. The CL contrast, when present, is much clearer and a routine CL examination to distinguish the two types of quartz is valuable. However Sippel cautioned that the absence of luminescence contrast does not prove the absence of secondary quartz. Sometimes both the overgrowth and the detrital core have the same dull CL colour. He also reported that in immature sandstones phenomena related to fracturing and healing by secondary quartz could be seen. CL can also observe the various degrees of crystallization and annealing.

Studying naturally deformed quartzite, Sprunt et al. (1979) found that metamorphism appears to homogenize the luminescence and the colour is related to the metamorphic grade: low temperatures result in a red luminescence whereas high temperatures cause a blue CL. They also stated that strain is a factor in the CL of quartz.

These same authors reported observations on quartz from granites and pegmatites. Their results concluded that quartz in 85% of the granite samples exhibited blue CL. In the reminder, the dominant CL colour is red.

An example of radiation-damage of quartz in uranium-containing sandstone was provided by Morton (1978). Distinct haloes, invisible in transmitted light or polarized light, show up as red luminescing rings on the quartz grains under CL. These haloes surround blue-luminescing cores. The widths of the radiation haloes were reported to be ~20 μm and the interpretation was that they are due to radiation damage by alpha particles, emitted by uranium containing minerals in the pore space.

The penetration range of alpha particles in solids is about 20 μm (Gentry 1973) and they apparently produce a radiation-damaged region with changed CL properties. The haloes are unstable under heating conditions and Morton suggested that these could be useful indicators of uranium presence in leached sandstones. The damage information would be retained after the leaching process, proving that the rock has not been subjected to temperatures high enough to be annealed.

Zinkernagel (1978) established one of the first classification schemes of quartz CL colours in sandstones. He divided the CL phenomena into three groups:

1) violet or blue luminescing quartz (major peaks at 450 nm and 620 nm) derived from igneous and high-grade metamorphic rocks that have undergone relatively fast cooling
2) brown-luminescing quartz (major peak around 620 nm and a minor peak near 450 nm) from low grade metamorphic rocks or slowly cooled high-grade metamorphic rocks
3) non-luminescing quartz of authigenic (diagenetic) or hydrothermal origin.

However numerous investigations showed that this general classification could not be widely applied because quartz grains with similar CL colours and emission spectra may have grown under different genetic conditions.

Nevertheless another general classification made by Ramsey et al. (1988) is often used. This interpretation divides the CL colours in quartz into five groups:

1) blue to violet colours belonging to plutonic quartz as well as phenocrysts in volcanic rocks and high-grade metamorphic quartz;
2) red colour belonging to matrix quartz and quartz phenocrysts in volcanic rocks;
3) brown colour belonging to quartz from regional methamorphic rocks;
4) non-luminescent or weakly luminescent authigenic quartz;
5) short-lived blue-green colour belonging to hydrothermal and pegmatitic quartz.

Ramseyer et al. (1988) suggested that the most likely cause of the brown CL colour is damage to the quartz lattice induced by particle bombardment, because artificially produced lattice dislocations or formations of unpaired, non-bonding electrons are known to induce such luminescence colour. Ramseyer et al. (1988) also proposed that the short-lived blue and bottle-green luminescence colours are probably related to interstitial cations in the c-axis channels of the quartz lattice, whereas the yellow luminescence colour in authigenic quartz was thought to be related to trace elements incorporated during crystallization from oxidizing fluids. Jones & Embree (1976) proposed that a strong luminescence signal in the ultraviolet range at 260 nm is most likely related to a trapped hole in quartz.

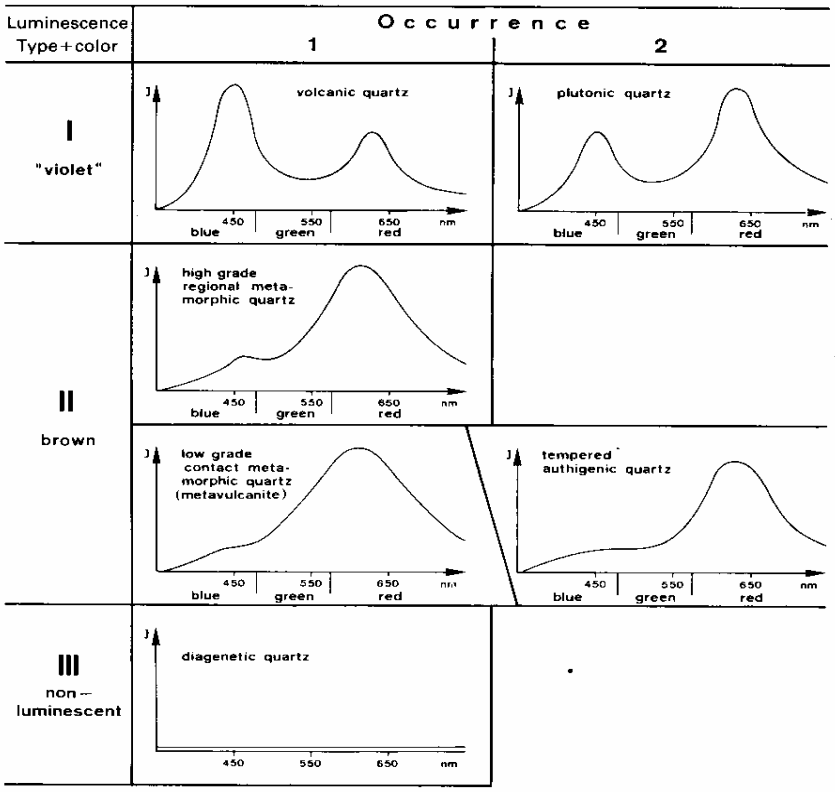

Figure 2.3: CL spectra of various types of quartz according to the classification proposed by Zinkernagel (1978).

Investigation of natural and synthetic quartz specimens showed various emission bands that were ascribed to different intrinsic and extrinsic defects. Goetze et al. (2001) provided a detailed review on CL spectra and possible origins of CL, including the radiation-damage-induced CL (Table 2.1).

Table 2.1 summarizes the current state of knowledge about CL colours in quartz and the principal ideas about the origin of the different CL spectral lines.

2.3 Cathodoluminescence equipment

The early observations of cathodoluminescence were accomplished with an electron probe as the source of excitation (Stenstrom & Smith 1964). Not long after, when cathodoluminescence became a routine technique for petrografic examination, the need for a simpler excitation source lead to the development of the cold cathode electron gun.

A number of cathodoluminescence arrangements have been designed, and the scanning-electron-microscope-CL (SEM-CL) will be described here.

The SEM-CL is one of the most important imaging instruments in geology. The scanning electron microscope utilizes a scanned electron beam with a small spot size of around 2 μm in diameter.

The advantages of the SEM-CL over the conventional (cold cathode electron gun) CL microscopy are the enhanced spatial resolution and the possibility of performing simultaneously back-scattered electron (BSE) imaging and microanalysis.

Emission line (nm)	Proposed Origin
175 nm 7.1 eV	Intrinsic emission of pure SiO_2
290 nm 4.3 eV	Oxygen deficit center (ODC)
340 nm 3.65 eV	Oxygen vacancy $[AlO_4/Li^+]$ center $[TiO_4/Li^+]$ center
380-390 nm 3.1-3.3 eV	$[AlO_4/M^+]$ center $M^+=Li^+, Na^+, H^+$ $[H_3O_4]^0$ hole center
420 nm 2.95 eV	Intrinsic emission
450 nm 2.8 eV	Intrinsic defect Self-trapped exciton (STE)
500 nm 2.5 eV	$[AlO_4]^0$ center $[GeO_4/M^+]$ center $[AlO_4/M^+]$
580 nm 2.1 eV	Oxygen vacancy Self trapped exciton (STE) E1' center
620 – 650 nm 1.96 – 1.91 eV	NBOHC Oxygen vacancy
705 nm 1.75 eV	Substitutional Fe^{3+}

Table 2.1: Characteristic emission band in the luminescence spectra of quarz (modified after Gotze et al. 2001).

The SEM has also a large depth of field, which allows a large amount of the sample to be in focus at one time. These advantages are extremely useful especially for samples with a low CL intensity, like quartz.

In other words, a solid material can be analyzed at a scale of a few microns or less, which allows the detection of a small compositional variations within an individual crystal, variation that can not be detected by bulk chemical analysis.

Two fundamental components comprise the SEM-CL system, the electron-optical system and the various detection systems (Fig. 2.4).

Electron-optical system (EOS)

The electron-optical system consists of an electron gun and a series of magnetic lenses and apertures, which focuses the beam electron on to a sample. Typically a hairpin tungsten wire is used in the electron gun to generate electrons by thermoionic emission. The electron beam is directed trough a vacuum chamber by the condenser lens and then focused on the sample. An analytical volume as small as 2-3 cubic microns is possible.

Cathodoluminescence detectors

Cathodoluminescence from specimens under electron bombardment can be detected with a photomultiplier (PM). Scanning CL images can be produced by modulating the display cathode-ray tube (CRT) with the PM output.

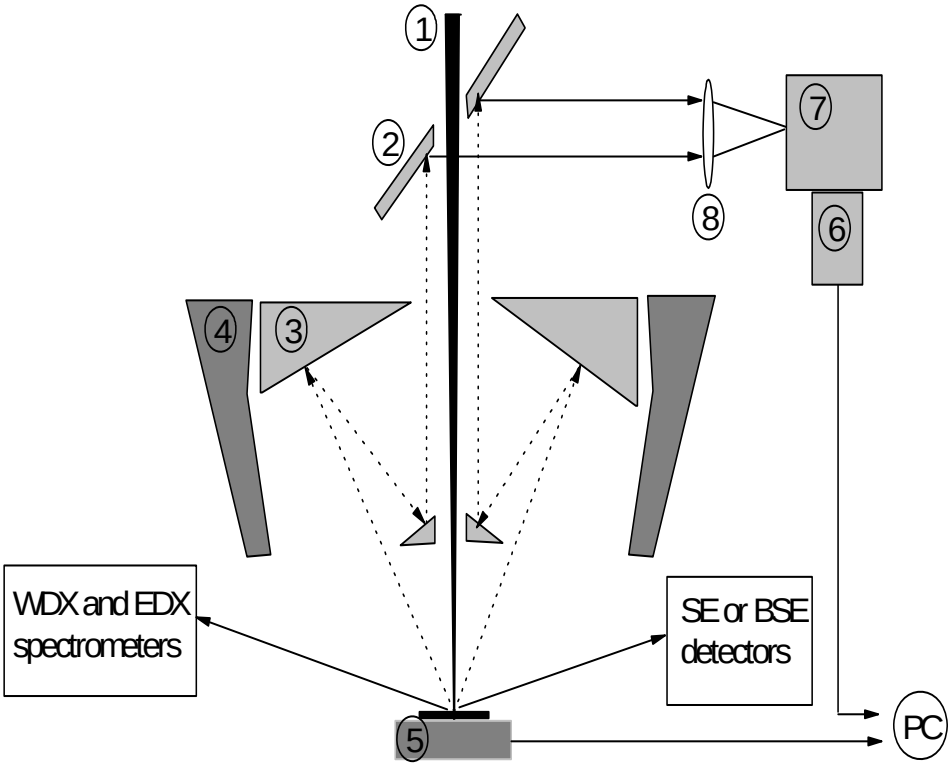

Figure 2.4: Diagram of SEM-CL spectroscopy system where 1 represents the electron beam, 2 mirror, 3 optical reflective objective, 4 electron objective, 5 scanning stage, 6 cooled charge-coupled device *ccd* detector, 7 spectrograph, 8 lens.

The light may be focused onto the entrance window of the photomultiplier with a lens mounted in the specimen chamber.

In SEM-CL, beside the cathodoluminescence detectors, several other types of detectors are used giving the option of obtaining both qualitative and quantitative analysis of the sample together with imaging.

A small fraction of the electrons striking the sample material results in inner sphere ionization. In other word electrons from inner orbitals are ejected.

When electrons from inner orbitals are ejected, photons with discrete energy will be emitted. Therefore characteristic X-rays are produced by electron transitions.

When a characteristic X-ray spectrum of a sample is produced we need a spectrometer to measure it. There are two types of X-ray spectrometers used in electron microprobes, the wavelength-dispersive X-ray spectrometer (WDS) and the energy-dispersive X-ray spectrometer (EDS).

The energy dispersive (EDS) and wavelength dispersive (WDS) systems both have benefits and disadvantages. The main differences between the systems are in detector efficiency and resolution.

Energy dispersive X-ray spectrometer (EDS)

The energy dispersive X-ray spectrometer is used for qualitative analysis. It consists of a solid-state detector that produces pulses proportional in size to the X-ray photon energy.

In EDS spectrometers the detection medium is a semiconductor with an electronic structure in which the valence band is normally fully occupied by electrons.

If one of these electrons is excited into the conduction band it becomes mobile the same as the positive hole left in the valence band. At room temperature very few electrons have enough energy to jump from the valence band into the conduction band and therefore the conductivity is very low.

When an X-ray photon is absorbed it generates Auger and photo-electrons which dissipate their energy partly in raising valence electrons into the conduction band. Therefore the arrival of each photon creates a pulse of current caused by electrons and holes moving in opposite directions.

The semiconductor detector is usually a *p-i-n* (p-type, intrinsic, n-type), lithium-drifted silicon (Si(Li)) crystal, although intrinsic, high-purity germanium (HPGe) is also used.

Wavelength dispersive X-ray spectrometer (WDS)

The wavelength dispersive X-ray spectrometer is used for highly quantitative analysis. Even though WDS spectrometer gives high spectral resolution, it provides signal with a lower intensity if compared to the EDS-type.

WDS spectrometer consists of a monochrometer and a detector.

The monochtometer is a crystal, or a synthetic multilayer material that disperses X-rays by Bragg reflection. Most electron microprobes are equipped with

several crystals offering different d- spacing to allow analysis of wider range of X-ray wavelengths.

The most common crystals are lithium fluoride (LIF), pentaerythritol (PET) and thallium acid phthalate (TAP). These crystals cover all X-ray wavelengths generated by elements with Z=11 (Na) to Z=92 (U). For lighter elements, a wider d-spacing is needed and in this case soap film or evaporate multilayer are used. The detectors convert X-rays photons through ionization into voltage pulses, which can be counted.

The type of X-ray detector used in WDX is called a proportional counter. It is a gas-filled tube with a coaxial wire held at a positive potential and a thin window to permit X-rays. There are two types of proportional counters, gas-flow and sealed. As the names suggest, the gas flow counter maintains a continuous flow of gas while the sealed counter is filled with gas and sealed permanently. The gas is ionized with free electrons attracted to the wire (anode) and positive ions to the body of the counter (cathode). As a result of the positive potential in the counter the free electron are accelerated and they cause further ionization. This cascade results in an electric charge on the wire proportional to the energy of the X-ray protons that initially ionized the gas. The gas flow counter is more sensitive to longer wavelengths X-rays (i.e. lighter elements) while the sealed counter provides superior counts at shorter wavelengths (i.e. heavier elements).

Therefore modern electron microprobes usually have both types of counters installed.

Beside EDS and WDS spectrometers the SEM-CL arrangement is also equipped with secondary electron (SE) and backscattered electron (BSE) detectors.

Electron detectors

The basic form of SEM is derived from secondary electrons ejected from the sample by the electrons in the incident beam.

Usually a scintillator makes the detection of the secondary electrons. The scintillator consists of either plastic or crystalline material that produces light when bombarded with electrons. The light is further converted to an electrical signal by a photomultiplier.

However secondary electrons are emitted with energies of only a few electron-volts (eV) and must be accelerated to a several kiloelectronvolts to produce a reasonable output for the scintillator. A positive potential (e.g. 10 kV) is therefore applied to a thin metal coating on the scintillator.

If only BSE detection is required a large scintillator located close to the specimen is used. A scintillator of the type illustrated in Figure 2.5 subtends a large solid angle enabling very good BSE images to be obtained using a low beam current.

Backscattered electrons can also be detected by solid-state devices. A large solid angle can be obtained by locating the detector directly above the specimen with the beam passing through a hole (Pagel et. al 2001).

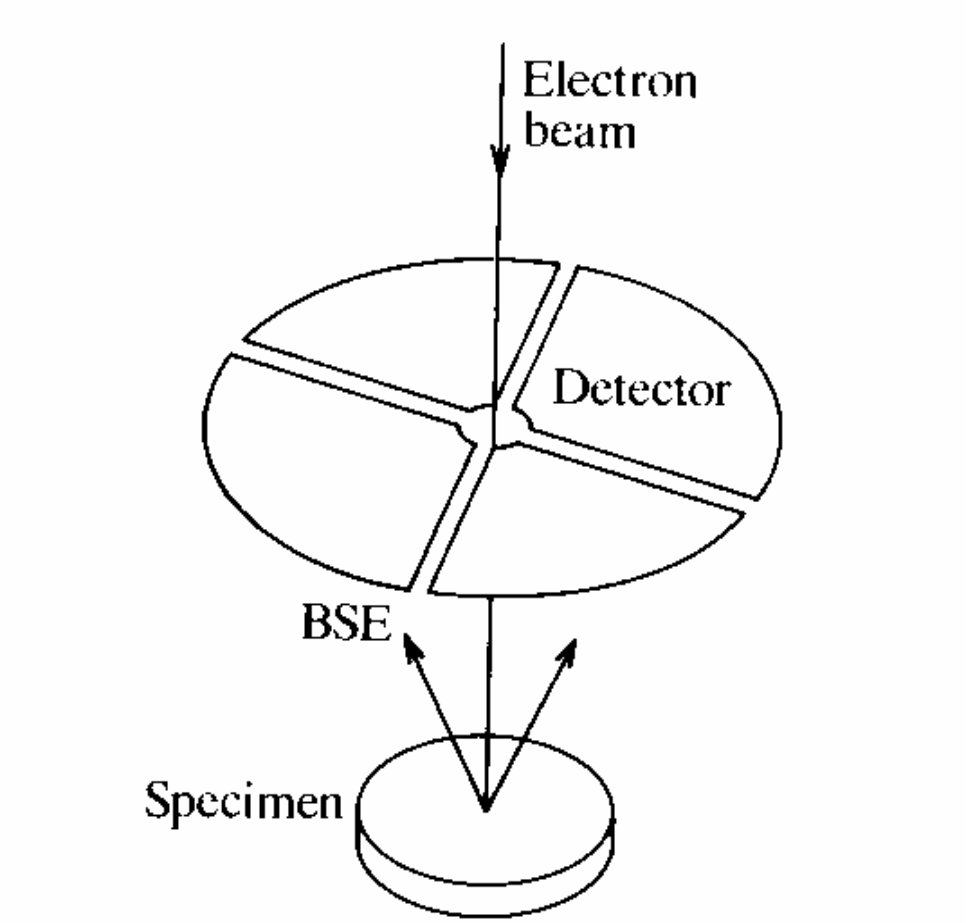

Figure 2.5: Diagram of a solid-state backscattered electron detector (after Pagel et. al 2001).

Chapter 3

EPR spectroscopy

Electron paramagnetic resonance (EPR) spectroscopy is a physical method of observing resonance absorption of microwave power in a magnetic field. Widely used as an analytical tool in chemistry, biochemistry, solid-state physics and medicine, EPR started to become popular in the field of geological sciences, not only as a dating technique but also as a method of structural analysis.

The unique feature of EPR spectroscopy its capacity for detecting paramagnetic species or species that can become paramagnetic after the change of charge state due to irradiation. Thus in principle, all atoms and molecules are amenable to study by EPR.

Typical systems that have been studied by EPR include:

a) free radicals in a solid, liquid or aqueous phase;
b) transition metal ions;
c) various point defects in solids;
d) systems with more than one unpaired electron (biradicals or triplet-state systems);

e) systems with conducting electrons (metals and semiconductors) (Weil et al. 1994).

3.1. Fundamental principles of EPR

Each atom and molecule has discrete spectrum of energy levels. Spectroscopy is the measurement and interpretation of the energy differences between these levels and allows the researcher to have an insight into the identity, structure and dynamics of the sample under study.

The energy differences studied by EPR spectroscopy are predominantly due to the interaction of the unpaired electrons with an external magnetic field. This effect is called the Zeeman Effect.

Because an electron has a magnetic moment due to its spin (S=1/2), it will be oriented in an external magnetic field, either in the direction of the field or in an opposite direction. Therefore in an external magnetic field, an electron will have two possible energy states. These two states are labeled by the projection of the electron spin number m_s; the energy states parallel to the external field is designated as m_s=-1/2 and the antiparallel state as m_s=+1/2.

The energy separation between these two states is known as the Zeeman energy:

$$E = g\mu_0 B_0 M_S = \frac{1}{2} g\beta B_0 \qquad 3.1$$

and

$$\Delta E = h\nu = g\beta B_0 \qquad 3.2$$

where g is the spectroscopic splitting factor, β is the Bohr magneton and B_0 is the external magnetic field.

For paramagnetic species in solids, their orbital momentum is quenched due to the crystal field, which respects the symmetry of the environment. Therefore the ground state should be a pure spin state and the EPR spectrum should be observed at a g factor equal to that of a free electron g_e=2.0023.

However, the g factors differ slightly from the g factors of the free electron due to the contribution of orbital angular momentum via the spin-orbit interaction. In a low symmetry environment the spin-orbit interaction will give rise to anisotropy in the g factor so that a g matrix will describe the Zeeman energy.

The symmetry of this matrix will further reflect the local symmetry of the site occupied by the paramagnetic species.

If the paramagnetic species has a nuclear magnetic dipole (I≠0) an interaction between the unpaired electron and the nuclear momentum will give rise to a further reorganization of the electronic spin levels. This interaction is called the hyperfine interaction and leads to a splitting of absorption line into (2I+1) components, which is very helpful in identification of the paramagnetic species.

The structure of the EPR absorption spectrum can be interpreted using the effective spin Hamiltonian:

$$H = \beta \vec{S}^T \cdot \hat{g} \cdot \vec{B} + \vec{S}^T \cdot \hat{A} \cdot \vec{I} \qquad 3.3$$

where $\vec{S}$ represents the effective spin of the spin center, $\hat{g}$ is a matrix , $\vec{I}$ is the nuclear spin angular momentum and $\hat{A}$ is the hyperfine interaction matrix including both isotropic and anisotropic contributions.

The first term in equation 3.3 arises from the electronic Zeeman interaction and the second term expresses the hyperfine interaction.

For S >1/2 the spin Hamiltonian also includes quadratic or higher order terms which are not relevant to this study and will not be discussed here.

The Zeeman term of the spin Hamilotonian and the g tensor

The first term in Equation 3.3 involves the g tensor. To understand the effect of the g tensor we consider a spin S=1/2 in a single crystal.

Let us choose laboratory coordinate frame x, y, z, not necessarily coincident with the crystallographic axes. The direction of the static magnetic field B is given by the direction cosines $\cos\theta_x$, $\cos\theta_y$, $\cos\theta_z$ with respect to axis x, y, z.

The Zeeman term of the Hamiltonian than becomes:

$$H_{zeeman} = \beta\left|S_x S_y S_z\right| \cdot \hat{g} \cdot \begin{vmatrix} \cos\theta_x \\ \cos\theta_y \\ \cos\theta_z \end{vmatrix} \qquad 3.4$$

where

$$\hat{g} = \begin{vmatrix} g_{xx} & g_{xy} & g_{xz} \\ g_{yx} & g_{yy} & g_{yz} \\ g_{zx} & g_{zy} & g_{zz} \end{vmatrix} \qquad 3.5$$

And therefore the spin can be considered as being subjected to an effective magnetic field vector

$$\vec{B}_{eff} = \cdot\hat{g} \cdot \begin{vmatrix} \cos\theta_x \\ \cos\theta_y \\ \cos\theta_z \end{vmatrix} \cdot B \qquad 3.6$$

which depends on the particular orientation of B.

Therefore the Hamiltonian becomes:

$$H_{zeeman} = \beta \cdot \vec{S} \cdot \vec{B}_{eff} \qquad 3.7$$

and its eigenvalues can be written as:

$$E_{zeeman} = \beta \cdot B_{eff} \cdot m_S \qquad 3.8$$

The splitting of the energy levels depends, through B_{eff}, on the orientation of B with respect to the x, y, z axes as stated by equation 3.6. This implies that the resonance magnetic field position in a single crystal is also a function of the direction of the external field.

Since B_{eff} depends also on g, the experimental determination of the resonance fields of a paramagnetic centre for various orientations of the applied static magnetic field B with respect to the crystal axes is a way to determine the g matrix components.

Once these components are found it is possible to diagonalize the g matrix and establish the principal axes of the paramagnetic defect, gaining information on the geometry of the center and on its orientation in the single crystal (Poole 1967).

The powder line shape

When the paramagnetic substance is in a powder sample the orientation of the crystal axes is completely random. So even if for each paramagnetic species we can define a g tensor, with respect to the crystal axes, we must consider the distribution of these axes orientations with respect to an external reference frame. A distribution of the resonance fields appears for any arbitrary orientation of the static magnetic field.

In addition it is possible, depending on the symmetry of the g tensor, that different spin center orientations give the same resonance field. This degeneration causes that for certain resonance fields a larger number of spins absorb energy than for other resonance fields.

The result of this distribution will be an asymmetric absorption line shape, characteristic for powders and amorphous materials.

In this particular case, the g matrix will have the following form:

$$\hat{g} = \begin{vmatrix} g_{xx} & 0 & 0 \\ 0 & g_{yy} & 0 \\ 0 & 0 & g_{zz} \end{vmatrix} \qquad 3.9$$

where g_1, g_2, g_3 are the principal values of the tensor.

Therefore the spin Hamiltonian becomes:

$$H_{zeeman} = \beta\left(S_1 g_1 \cos\theta_1 + S_2 g_2 \cos\theta_2 + S_3 g_3 \cos\theta_3\right)B \qquad 3.10$$

with the eigenvalues:

$$\left(E_{zeeman}\right) = m_S \beta B \sqrt{\left(g_1 \cos\theta_1\right)^2 + \left(g_2 \cos\theta_2\right)^2 + \left(g_3 \cos\theta_3\right)^2} \qquad 3.11$$

The energy splitting between two adjacent energy levels is given by:

$$\Delta E = \beta B \sqrt{(g_1 \cos\theta_1)^2 + (g_2 \cos\theta_2)^2 + (g_3 \cos\theta_3)^2} \qquad 3.12$$

The amplitude of the absorption depends on the number of spin centers whose g tensor principal values coincide with the reference frame chosen and, therefore, with the probability of finding a spin in such an orientation.

So scanning the distribution of the magnetic field we scan the distribution of the orientation of the spin centers in a powder or glass matrix.

The absorption line shape in amorphous or powder matrices has been calculated theoretically (Weeks & Nelson 1960, Sands 1955). On the basis of these theoretical results, one can infer the principal values g_1, g_2, g_3 from the field position (see Fig. 3.1).

A typical powder-like EPR spectrum for S=1/2 center is illustrated in Figure 3.1, both for derivative and absorption spectra. The position of the principal g values can be determined from the derivative spectrum as seen in Fig. 3.1a. Moreover one can deduce the symmetry properties of this center. As an example if two of the principal axes coincide, one can deduce that the center has an axial symmetry.

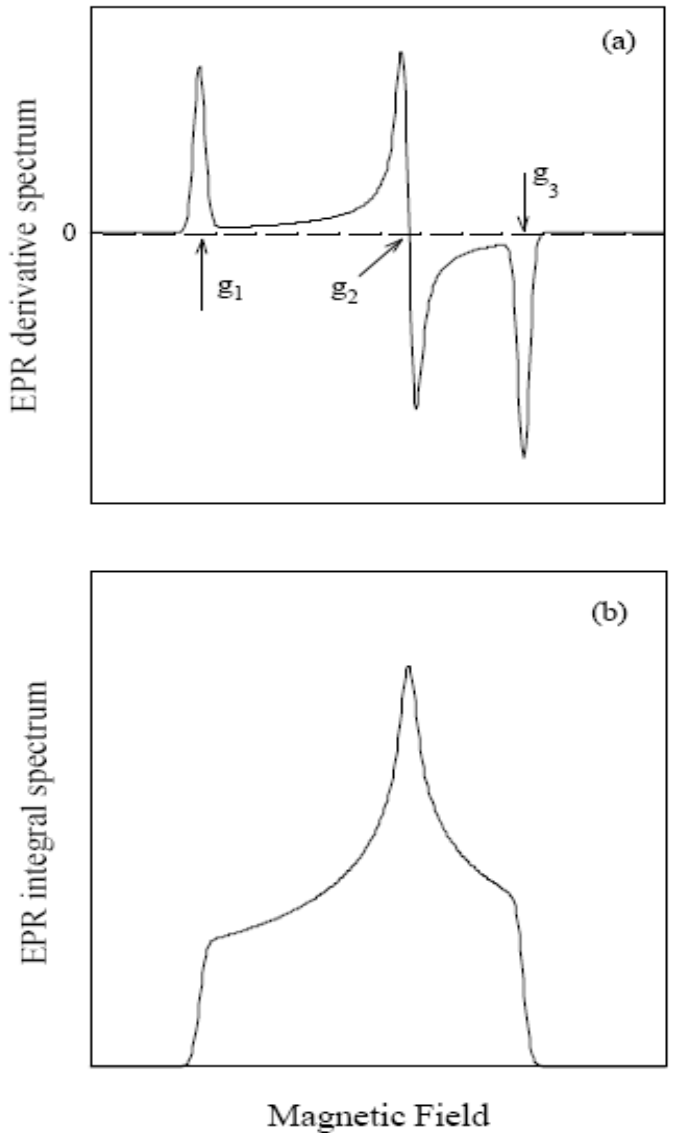

Figure 3.1: Typical EPR signal for amorphous or powder: a) first derivative, b) absorption line.

3.2 Paramagnetic centers in quartz

Quartz structure

Each Si atom in quartz is bonded to four oxygen atoms and each oxygen atom is bonded to two Si atoms. This arrangement creates a network of linked SiO_4 units with a crystalline structure belonging to the trigonal trapezohedral class of the rombohedral subsystem and a hexagonal lattice. The space groups that describe left and right quartz (in a right-handed hexagonal system) are $P3_121$ and $P3_221$ and the Laue class is D_{3d}. There is neither a symmetry plane nor a center of symmetry.

Within the hexagonal unit cell, four axes are used to determine the reference system. Two of these axes a_1 and a_2 coincide with two C_2 symmetry axes and are at an angle of 120° from each other. A third a_3 axis that is 120º from the a_2 axis is not a C_2 type of axis. The crystallographic c-axis is the fourth axis in the reference system and is considered to be coincident with the cartesian z-axis and normal to the plane formed by a_1 and a_2.The conventional unit cell in quartz contains Si_3O_6.

The smallest formal structural unit in quartz is a pseudo-tetrahedron formed by the central Si atom surrounded by four O atoms. The deviation from a true tetrahedron is due to the asymmetry from different Si-O bond lengths. Two of the bonds, the so-called “long bonds”, measure about 16.145 nm (94 K) and the other two bonds, “short bonds”, measure about 16.101 nm (94 K) (LePage et al. 1980). This destroys the local C_3 axes, the local S_4 axes, and all local planes of symmetry. The local symmetry elements that remain are a C_2 and a C_1 axis. The SiO_4 pseudo-tetrahedra occur in three

different special orientations within the quartz structure. These orientations are related by rotation around the c-axis.

The crystal structure of quartz presents two types of parallel channels different in diameter. The crystallographic c-axis is defined along the small channels and the large channels are parallel to the c-axes (Fig. 3.2). These large c-axis channels provide a good location for the interstitial cations, which can diffuse along the channels.

Structural defects in quartz

Quartz defects can be classified in three categories according to their structure and size:

a) point defects (most important for luminescence studies);

b) dislocations;

c) inclusions and clusters.

During crystallization the impurities and lattice defects are generally incorporated as charge compensated diamagnetic defects.

Natural radioactivity as well as the electron irradiation during experiments, causes the transformation of diamagnetic precursors into paramagnetic centers.

EPR studies have identified around 100 different paramagnetic defect centers in quartz which can be divided into two main categories: 1) vacancy centers and 2) impurity centers.

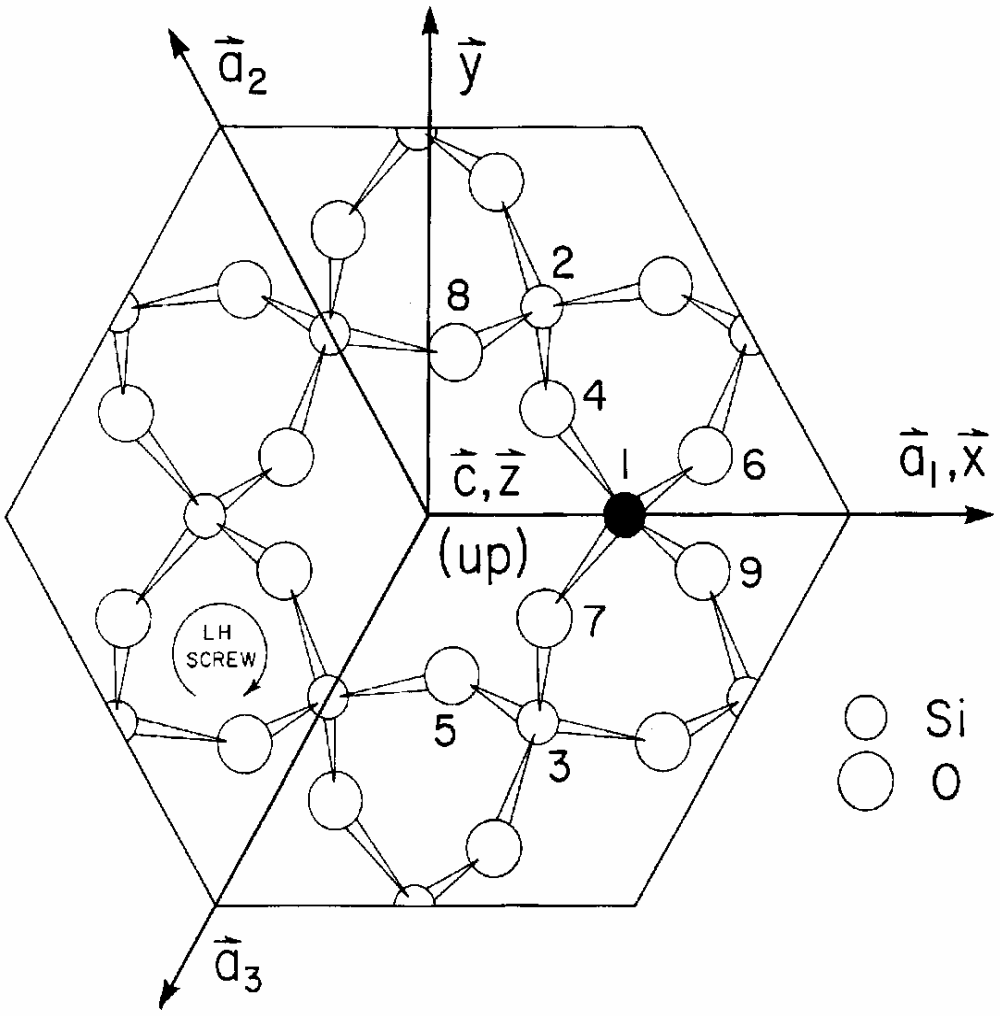

Figure 3.2: Crystal structure of quartz, projection on the plane perpendicular to c-axis showing the large central c-axis channel surrounded by 6 smaller channels. The three axes a_1, a_2 and a_3 are identical, and a typical site if Si on a_1 is showed by a filled circle.

Paramagnetic vacancy centers

The vacancy centers can be further divided in electron centers (oxygen vacancies) and hole centers (silicon vacancies). The best-known vacancy centers in quartz are the E′ centers, the peroxy centers and the non-bridging oxygen hole centers like O_2^- and O_2^{3-} centers (Fig. 3.3).

The E_1' center

Structural model: The E_1' center is one of the best-known radiation-induced paramagnetic defects observed in both fused and crystalline quartz. This defect consists of an electron in an oxygen vacancy, where the electron occupies a dangling sp^3 hybrid orbital of silicon bonded to three oxygen atoms (Feigl and Anderson 1970). The E_1'center can be produced and observed at room temperature by gamma-irradiation of amorphous SiO_2 and crystalline quartz (Silsbee 1961).

Thermal properties: The E_1' center is known to increase in intensity with increasing temperature at below 200 °C but is annealed out between 360-380°C (Ikeya 1993). The regeneration efficiency of the E_1' center is strongly reduced by annealing at 500 °C. From annealing experiments and saturation properties, two types of the E_1' center have been proposed to exist: one annealed at around 200 °C (observed only in artificially irradiated samples), and another stable up to 360-380 °C (Griffiths et al. 1982). In amorphous SiO_2, the E_1' center is annealed at about 100 °C (Stapelbroek et al. 1979).

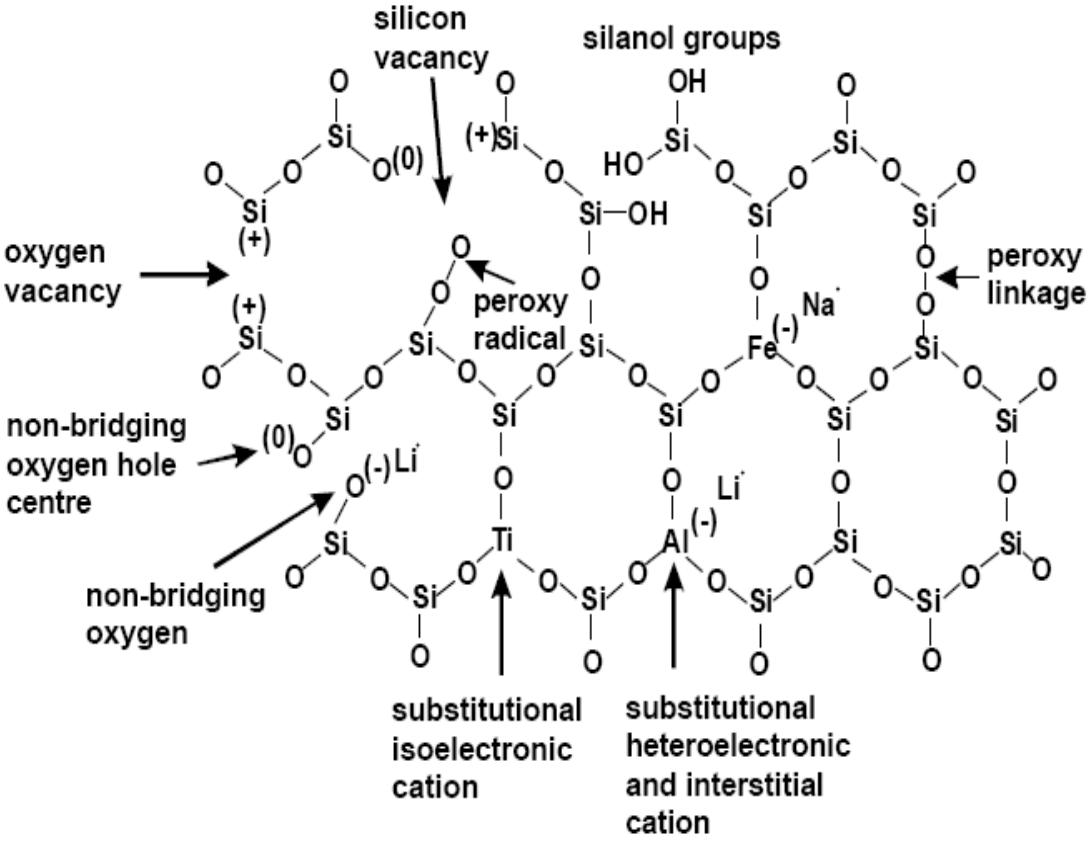

Figure 3.3: Schematic quartz structure showing the most common intrinsic and extrinsic lattice defects (Gotze et al. 2001).

Microwave power dependence: The E_1' center is known to saturate at a microwave power of 10^2 mW (Ikeya 1993).

Silicon vacancy hole centers

A number of silicon vacancy hole centers have been proposed to occur in amorphous and crystalline SiO_2. These hole centers commonly involve a silicon vacancy, which leads to hole trapping by two oxygen atoms, forming O_2^{3-} centers ($O^- + O^{2-} \rightarrow O_2^{3-}$; Mashkovtsev et al. 1978). These centers can only form on two of the four O – O edges of the SiO_4 tetrahedron, at those perpendiculars to the C_2 axis (Fig. 3.2). Mashkovtsev et al. (1978) reviewed three silicon vacancy hole centers in quartz and provided the following g factors:

- O_2^{3-}/H^+ (I): g=2.0021, 2.0074, 2.0295
- O_2^{3-}/H^+ (II): g=2.0007, 2.0042, 2.0052
- O_2^{3-}/M^+ (where M can be Na, Li, etc.) g=2.0024, 2.0076, 2.0494

Thermal properties: Mashkovtsev et al. (1978) noted that these O_2^{3-} centers increase in EPR intensity with increasing temperature and are best resolved at 200 to 250 ˚C. Mashkovtsev et al. (1978) also noted that the O_2^{3-} centers are stable up to 300 to 350 ˚C.

Peroxy centers (PR1 and PR2)

Structural model: The peroxy type radicals are paramagnetic molecular species consisting of an O_2^{2-} molecular ion bonded to another molecular complex generally

denoted R (Griscom & Friebele, 1981). The existence of peroxy radicals as radiation-induced defects in glasses was first suggested by Cohen et al. (1959) on the basis of the experimentally determined g matrices. The structural model was confirmed by the hyperfine structure of artificially ^{17}O-enriched samples (Griscom 1989).

Thermal properties: Griscom and co-workers reported that the peroxy centers increase in EPR intensity with annealing temperature below 400 ˚C and remain stable at 700 ˚C.

Impurity defect centers

Impurity ions enter either interstitial or substitutional positions in the quartz lattice depending on ion radius and charge. The numbers of ions, which can substitute for the silicon atom in the quartz lattice, is limited because of the small ionic radius of Si^{4+} compared to its 4+ valence. Typically these substitution impurities are Al^{3+}, Ti^{4+}, Ge^{4+}, Fe^{3+}, P^{5+}, and Ga^{3+} (Maschmeyer & Lehmann 1983, Weil 1984).

The impurity ions form a variety of defect centers depending on the kind of ion-charge compensator in the structural channels (H^+, Li^+, Na^+) as well as on the position of the ion-charge compensator. Large open channels thread through the quartz structure parallel to the c-axis and offer locations for interstitial cations such as H^{1+}, Na^+, K^+, Li^+, Fe^{2+}, Cu^+, Co^{2+} or Ag^+. They act as charge compensators for substitutional ions like X^{3+} and X^{5+}.

There are also geometrically nonequivalent positions; some positions of the same center related to one another through the lattice symmetry elements.

The paramagnetic impurity centers that are built by tetravalent ions (mostly $Ti^{4+}$and Ge^{4+}) cause the formation of the diamagnetic $[XO_4]^0$ centers. These centers act as the precursors for paramagnetic $[XO_4]^-$ centers, which develop during ionization irradiation. At room temperature these centers bind diffusing M^+ cations such as H^+, Li^+, Na^+ forming a paramagnetic $[XO_4/M^+]^0$ center (Rinneberg & Weil 1972; Weil 1993).

3.3 EPR spectrometer

The energies of magnetic dipoles in a typical static magnetic field are such that frequencies in the microwave region are required to induce resonance transitions. A schematic experimental arrangement is shown in Figure 3.4.

The basic setup for a continuous wave (CW) EPR spectrometer consists of a microwave source, a magnet with variable field, a resonant cavity, magnetic field modulation coils, a microwave diode as a detector, and a computer for data acquisition, storage and processing (Weil et al.1994).

The cavity substitutes for the RLC resonant circuit at microwave frequencies, where conventional coils and capacitors would have impractical dimensions. The cavity dimensions are on the order of the wavelength of the microwave irradiation (~cm to ~mm range).

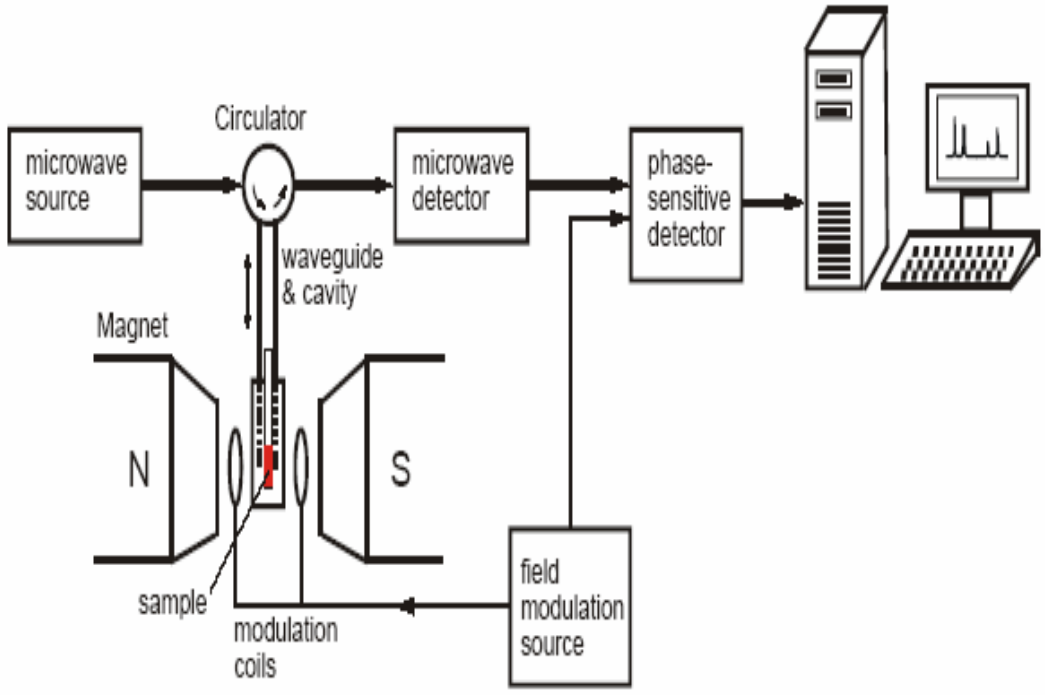

Figure 3.4: Schematic of an EPR spectrometer.

The experiments are done at fixed microwave frequency and the magnetic field is swept. At the field where the spin system is off resonance, the cavity is tuned to the microwave frequency and the impedance of the cavity is matched to the impedance of the waveguide.

Under these conditions, no microwave is reflected by the cavity. The resistance of the resonance circuit absorbs all power that is transmitted from the source to the cavity. Therefore no microwave leaves the cavity towards the circulator and no power is transmitted from the circulator to the microwave detector.

When the system reaches the resonance state, it starts to absorb microwave. Thus the impedance and Q values of the cavity change. This causes reflection of a small part of the microwave power. The circulator guides this reflected microwave power towards the detector and a signal arises.

The described setup would not be very sensitive using a common microwave detector, because of the very broad band and the high noise level. To overcome this problem, the magnetic field is modulated at a low frequency (typically 100 kHz). This causes a modulation of the reflected microwave and thus of the detector output current with the same low frequency.

The phase sensitive detector basically measures the amplitude of this signal modulation. Since most of the microwave noise does not oscillate with the same phase as the field modulation, at this low frequency, it can be suppressed.

As a consequence of this kind of detection, changes in the signal that are caused by the field modulation are measured. The signal acquired during the field sweep therefore corresponds to the derivative of the absorption line.

Chapter 4

Sample preparation and chemical characterization of sandstones from the Athabasca Basin

4.1 Sample preparation

This thesis is a part of a broad study on radiation-damage-induced CL in quartz grains associated with uranium deposits in the Athabasca Basin. Approximately one thousand samples from the eastern part of the Athabasca Basin have been investigated in this study. Most of these samples were collected as part of previous studies of clay minerals in this basin (Zhang et al. 2001, Wasyliuk 2002). Emphasis was placed on approximately three hundred samples from five diamond drill holes from Cigar Lake (WDG1), Key Lake (DDH2217) and McArthur River Deposit (MAC223) and BJ zone (MAC121 and MAC135A) to document the distribution of radiation-damage-induced CL in quartz with respect to mineralization and stratigraphy.

Polish thin sections of these samples were first prepared for petrographic examination and the documentation of CL in quartz grains.

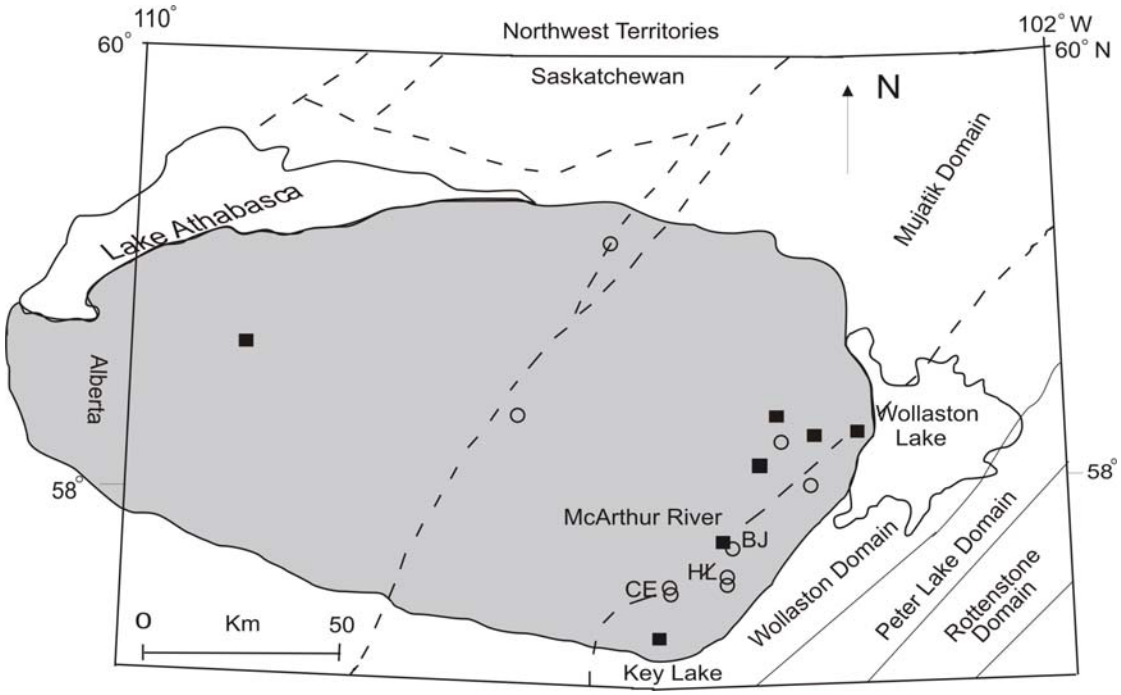

Figure 4.1: Location map of the Athabasca basin.

McArthur River Deposit		
Hole	Depth (m)	Description
MAC-223	125	sandstone
MAC-223	225	sandstone
MAC-223	355	sandstone
MAC-223	475	sandstone
MAC-223	635	basement quartzite
MAC-223	655	basement quartzite
BJ zone		
MAC-121	25	sandstone
MAC-121	125	sandstone
MAC-121	265	sandstone
MAC-121	305	sandstone
MAC-121	385	sandstone
MAC-121	465	basement rocks
MAC-121	476	basement rocks
MAC-135A	106	sandstone
MAC-135A	146	sandstone
MAC-135A	186	sandstone
MAC-135A	216	sandstone
MAC-135A	236	sandstone
MAC-135A	286	sandstone
MAC-135A	356	sandstone
MAC-135A	376	sandstone
MAC-135A	368	sandstone
MAC-135A	386	sandstone
MAC-135A	406	mineralized sandstone
MAC-135A	416	sandstone
Key Lake Deposit		
DDH-2217	19	sandstone
DDH-2217	26	sandstone
DDH-2217	53	sandstone
DDH-2217	71	mineralized sandstone
DDH-2217	77	sandstone
Cigar Lake Deposit		
WDG1	432	sandstone

Table 4.1: List of samples analyzed by both CL and EPR techniques.

From these three hundred samples, a total of 31 samples (Table 4.1) have been investigated for documenting the origin, development and distribution of radiation-damage-induced CL in quartz grains from this basin and the local distribution of the paramagnetic defects in sample's volume. These samples were subjected to mineral separation and annealing experiments.

One sandstone sample from the McArthur River deposit (H737-58), which has one of the most pervasively developed CL, was selected for detailed investigations.

All the samples were soaked in distilled water for several days, then crushed gently into small pieces and washed in an ultrasonic bath. The disintegrated grains from the ultrasonic treatment were then sieved (> 25 mesh or 0.7mm in diameter), washed and dried for several hours in air at room temperature. Pure quartz grains without any visible mineral inclusions were then selected by handpicking under a binocular microscope.

Small fragments and pure quartz separates of selected sample H737-58 have been annealed under atmospheric pressure at various temperatures in a Thermolyne muffle furnace. These annealing experiments were made at the following temperatures: 100, 200, 300, 400, 450, 500, 550, 600, 700, 800, 900 and 1000 ˚C. The annealed samples were investigated by a detailed X-band EPR study, and selected grains were also mounted and polished for CL examination.

Quartz separates (~100 mg) from two background samples (103 and 376) and three CL active samples (DDH2217-254, MAC223-635 and H737-58) were subjected to dissolution treatment by immersion in concentrated HF in teflon capsules. These

quartz separates, after a total of 8 hours of HF treatment, were washed in water in an ultrasonic bath, air-dried and then were weighed to determine mass reduction. The HF treatment resulted in a loss of ~ 20 mg for each sample.

4.2 ICP-MS analysis of sample H737-58

Sample H737-58 was selected for detailed CL and EPR analysis and therefore a compositional ICP-MS analysis of this sample was made.

ICP-MS analysis revealed that the quartz separates from H737-58 contain Ti (41 ± 0.98 ppm), Mn (0.97 ± 0.18ppm), Cu (03.8 ± 0.05ppm), Zn (49 ± 1.89ppm), Ge (0.95 ± 0.06 ppm), Sr (9 ± 0.2 ppm), Zr (12 ± 0.05 ppm), Al (590 ± 1.2 ppm), Ce (4.4 ± 0.02 ppm), Pb (13 ± 0.03 ppm), Th (0.69 ± 0.01 ppm) and U (167 ± 0.01 ppm). The most salient feature of the trace element data in this sample is the significant Al content, which is a common constituent in natural quartz (Weil 1984; Demars et al. 1996). Lithium was sought for but is below the detection limit of 2.3 ppm. Titanium in H737-58 may be present in the quartz structure (Weil 1984; Plötze & Wolf 1996), although rutile has been observed as a common mineral inclusion in quartz grains of this sample and may not be completely eliminated during mineral separation. The presence of significant amounts of U, Pb, Zr and Zn is also likely attributable to contamination from mineral inclusions.

Chapter 5

Cathodoluminescence characterization of Athabasca quartz

Cathodoluminescence (CL) imaging was performed on a JEOL 8600 Superprobe electron microprobe analyzer (EMPA), equipped with a CL detector, at the Department of Geological Sciences, University of Saskatchewan. Both backscattered electron (BSE) and CL images were acquired using a Gellar Micro Analytical's dPict digital image acquisition system. BSE images were acquired at an accelerating voltage of 15 kV and a beam current of 10 nA beam. All CL images were obtained at 15 kV and 75 nA beam.

Quantitative CL spectra of sample H737-58 were collected on a JEOL JSM-6360 scanning electron microscope equipped with a Gatan MonoCL3 spectrometer, at the University of Regina. This instrument was operated at an acceleration voltage of 5 kV. CL spectra were collected in the range of 300-700 nm, with a spectral resolution of 2 nm.

5.1 CL microscopy study of quartz in the Athabasca Basin

Athabasca sandstones are composed mainly of detrital quartz grains with variable amounts of clay and other minerals (kaolinite, dickite, illite, hematite, chlorite, magnesiofoitite, crandallite-goyazite, rutile, zircon, monazite, xenotime, and uraninite;

Kotzer & Kyser 1995; Fayek & Kyser 1997; Zhang et al. 2001; Wasyliuk 2002). One characteristic feature of Athabasca quartz grains, especially those in alteration haloes associated with uranium mineralization, is the common development of secondary overgrowths (Fig. 5.1).

Kotzer & Kyser (1995), on the basis of petrographic evidence, fluid inclusion measurements and isotope geochemical analysis, distinguished two generations of quartz overgrowths (Q1 and Q2) in the Athabasca Basin.

Q1 occurs with early hematite, illite, kaolinite and dickite (Zhang et al. 2001, Wasyliuk 2002) as part of a basin-wide alteration assemblage. The Q1 overgrowths are commonly irregular in shape (i.e. variably corroded during subsequent fluid events) and are characterized by the presence of randomly distributed fluid and mineral inclusions.

The Q2 overgrowths are usually euhedral in shape and are characterized by well-developed growth patterns defined by oscillatory/sector distributions of fluid and mineral inclusions (Kotzer & Kyser 1995). Euhedral quartz grains (up to several millimeters in size) are also common as in-fillings in reactivated faults, late fractures and voids.

Cathodoluminescence imaging distinguishes detrital quartz grains from their secondary overgrowths (Figs. 5.1a, b), the latter being less luminescent than the former.

The two generations of quartz secondary overgrowths are also distinguishable on the basis of their overall CL pattern. Q1 overgrowths are either CL inactive or exhibit weak CL with irregular patterns (Figs. 5.1c, d). Q2 overgrowths, on the other

hand, commonly possess weak CL revealing oscillatory/sector growths patterns (Figs. 5.1e, f). Similarly, euhedral quartz grains in reactivated faults, late fractures and voids are commonly CL inactive, although weak CL revealing growth zoning is observed locally in those euhedral grains (Fig. 5.1i). It should be emphasized that the overall CL patterns described above are those developed throughout individual detrital quartz grains and secondary overgrowths and are distinct from the radiation-damage-induced CL (see below).

5.1.1 Radiation-damage-induced CL

Petrographic examinations revealed that quartz grains from the Athabasca sandstones exhibit three distinct types of bright CL that superimposes on the overall CL: 1) concentric haloes around U- and Th-bearing mineral inclusions (Figs. 5.2a, b); 2) patches in association with U-bearing minerals in matrices or pores (Figs. 5.2c, d) or without any association with U-bearing minerals and 3) continuous rims with or without any association of U-bearing minerals (Figs. 5.2g, h, e, f).

Bright CL haloes around U- and Th-bearing mineral inclusions in quartz have been observed in both sandstones and basement rocks. Although CL haloes occur in both detrital quartz grains and their secondary overgrowths in sandstones and have been observed occasionally in euhedral quartz grains in faults, fractures and voids, the associated U- and Th-bearing mineral inclusions in detrital quartz grains are different from those in overgrowths.

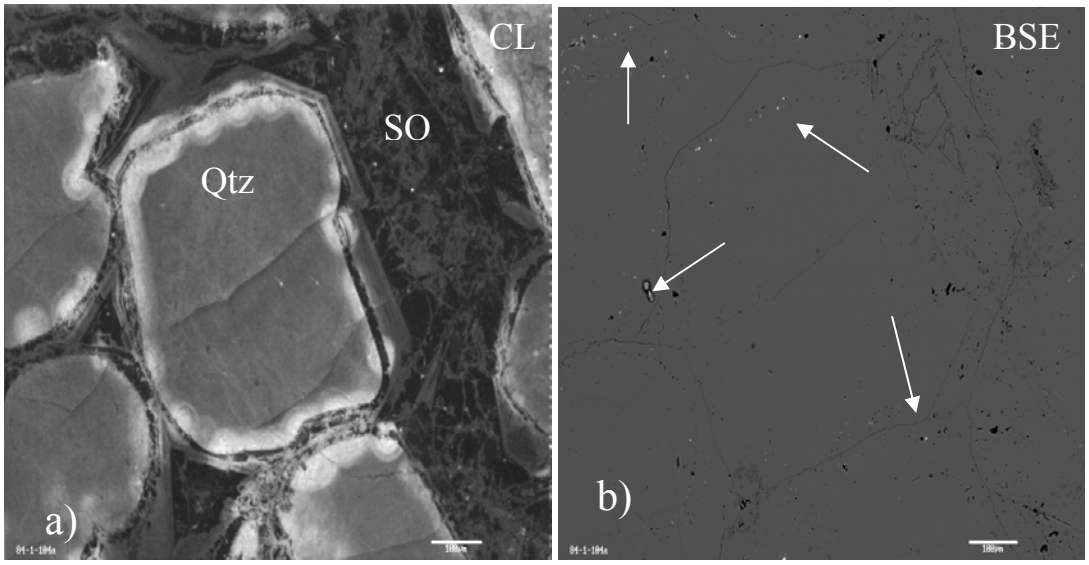
CL
SO
Qtz
a)
BSE
b)

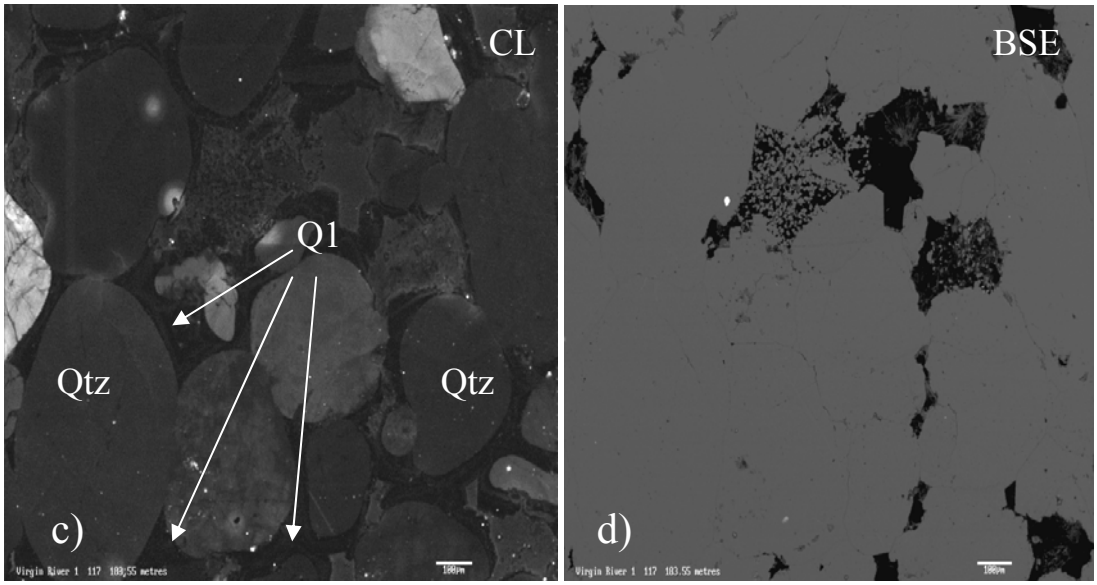
CL
Q1
Qtz
Qtz
c)
BSE
d)

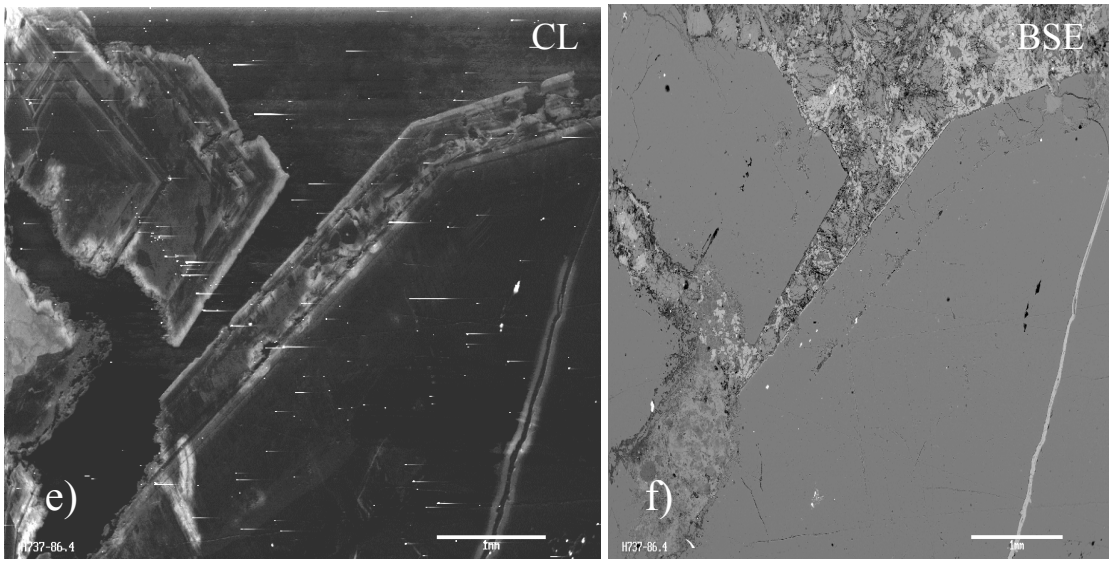
CL
BSE
e)
f)
H737-86.4
1mm

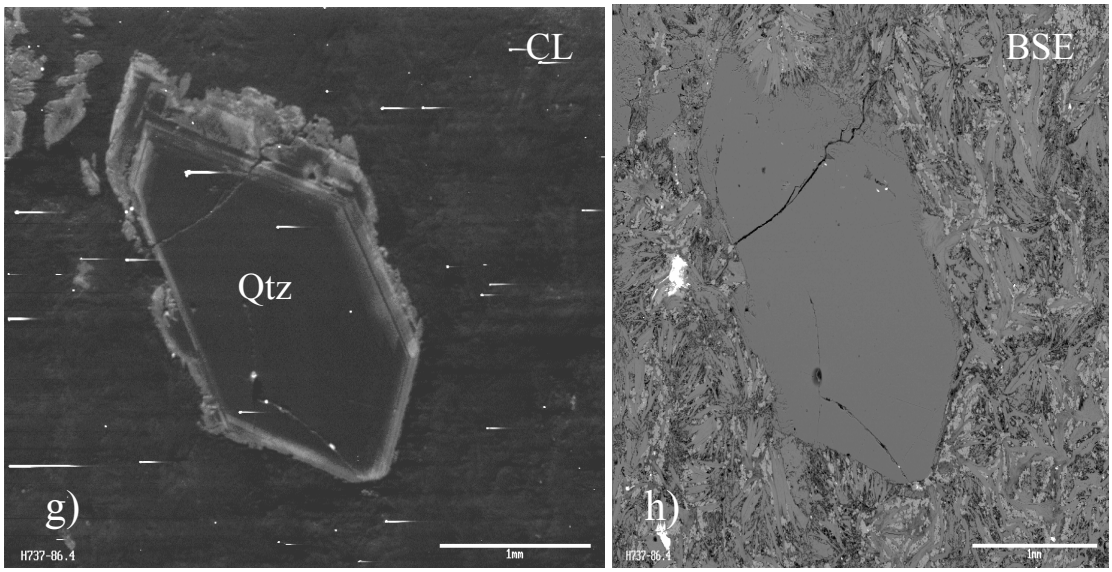
CL
BSE
Qtz
g)
h)
H737-86.4
1mm

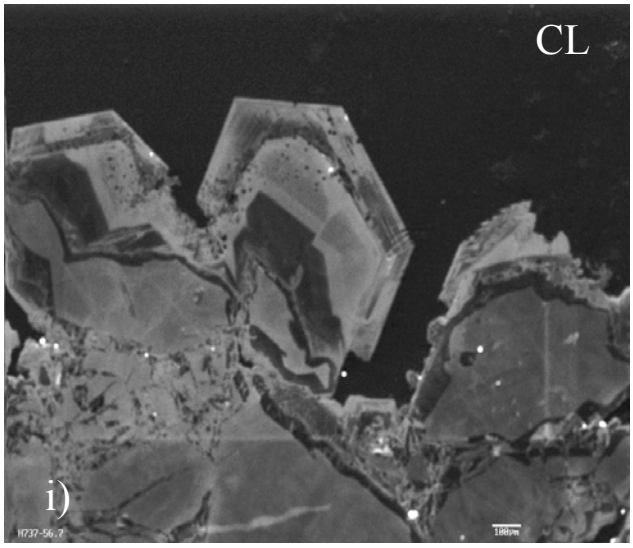

Figure 5.1: Cathodoluminescence (CL, a, c, e, g, i) and backscattered electron (BSE, b, d, f, h) images illustrating detrital quartz grains and well developed overgrowths in Athabasca sandstones: a) & b) sample H737-58 showing detrital quartz distinct from secondary overgrowths (SO). Note that radiation-damaged-induced CL associated with U-rich minerals (highlighted by arrows in b) along the boundaries between detrital quartz and secondary overgrowth. c) & d) Sample 117-183 from Virgin River showing CL active detrital grains and CL inactive Q1 overgrowth on CL active detrital quartz grains. e) & f) Sample H737-86 illustrating euhedral quartz grains with oscillatory/sector zoning as revealed by weak CL. g) & h) Euhedral quartz grain exhibiting oscillatory growth zoning as revealed by weak CL in a clay-rich void. i) Euhedral grain with well developed oscillatory/sector zoning as revealed by CL from a late hydrothermal vein.

Zircon is by far the most common U-bearing mineral inclusion in detrital quartz grains, in which monazite, fluorapatite and rutile have also been found but are much less common. Crandallite-goyazite and uraninite are the most common U-bearing mineral inclusions in quartz overgrowths. Other U-bearing minerals in overgrowths include xenotime, fluorapatite, monazite, and rutile.

U-bearing mineral inclusions in euhedral quartz grains in faults, fractures and voids, albeit less common, are similar to those observed in the secondary overgrowths.

The CL intensity of haloes around zircon varies significantly in different detrital quartz grains, even within the same sandstone sample. Also, CL haloes associated with uraninite in overgrowths are significantly brighter than those associated with other minerals (e.g., crandallite-goyazite and rutile). These observations suggest correlations between CL intensity and radiation dose. However, attempts to correlate the CL intensity of haloes with the U (and Th) contents in their associated mineral inclusions were not successful owing to presumably large differences in age of U- and Th-bearing mineral inclusions (see also Owen 1988).

CL patches in contact with U-bearing minerals in matrices or pores have been observed to occur at the margins of 1) detrital quartz grains, 2) secondary overgrowths (both Q1 and Q2), and 3) euhedral quartz grains in faults, fractures and voids. The suite of U-bearing minerals in matrices and pores includes crandallite-goyazite, uraninite, fluorapatite, xenotime, monazite and rutile, similar to that observed in quartz overgrowths.

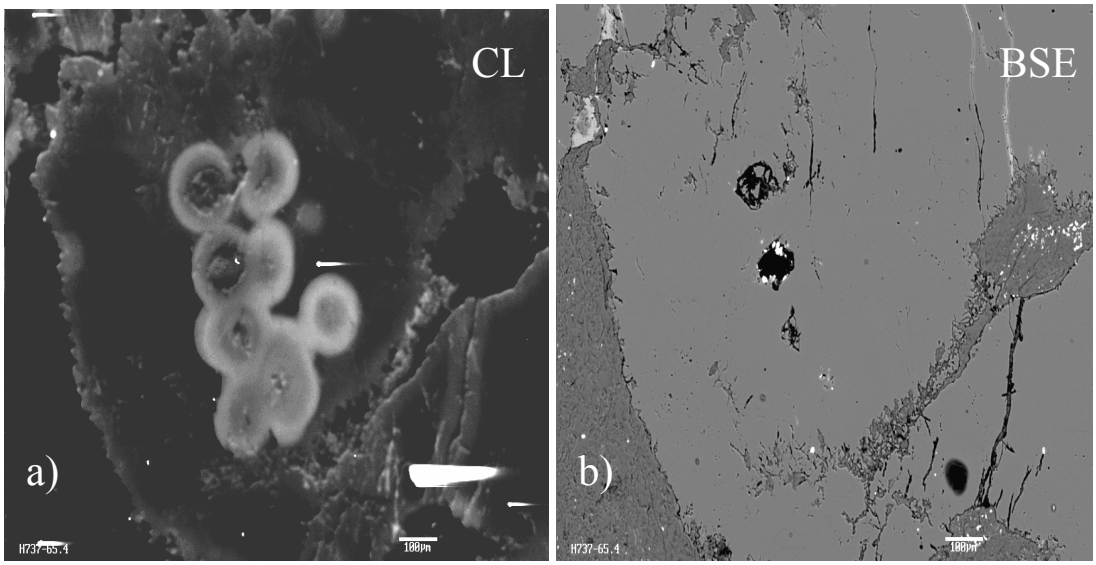
CL
BSE
a)
b)

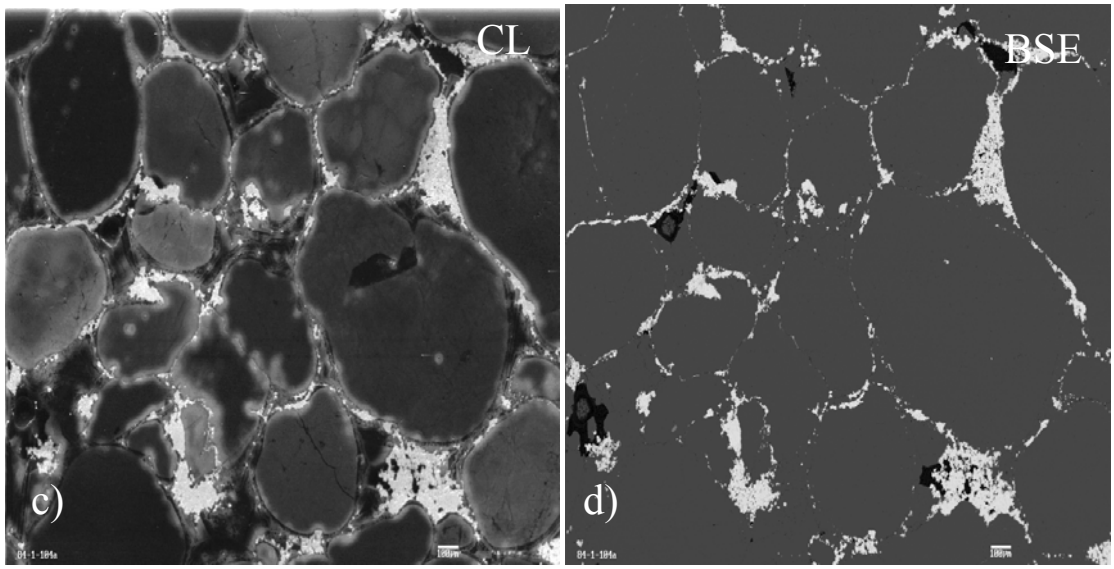
CL
BSE
c)
d)

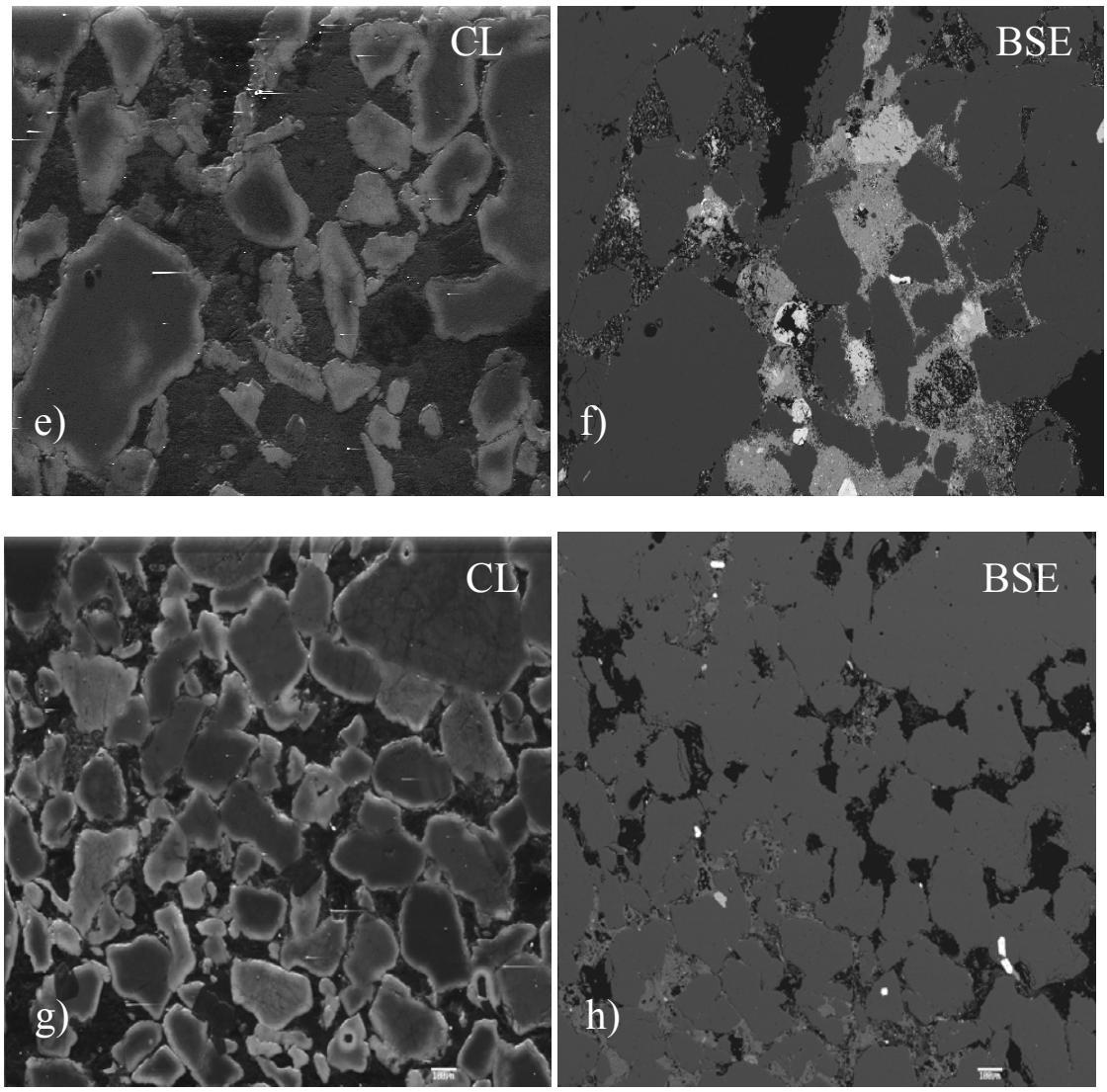

Figure 5.2: Cathodoluminescence (CL) and backscattered electron (BSE) images illustrating various types of radiation-induced-damages: a) & b) radiation-induced halos around zircon inclusions in quartz from sample H737-65, c) & d) radiation-damage-induced patches associated with U-bearing minerals on the margins of detrital quartz grains in sample H737-58, e) & f) continuous rims in association with U-bearing minerals in sample MAC135A-406, g) & h) continuous rims on the detrital quartz grains near a lithological boundary from sample MAC121-185.

Similarities between those CL patches and CL haloes are best illustrated by the common occurrence of abundant U-bearing minerals (e.g., crandallite-goyazite and uraninite) along boundaries between detrital quartz grains and Q1 overgrowths in mineralized sandstones. Here, the U-bearing minerals result in bright CL patches on both the detrital quartz grains and Q1 overgrowths, which join together to form concentric haloes (Fig.5.3).

Continuous CL rims have been observed to occur only at the margins of detrital quartz grains (Figs. 5.2g, h). They are commonly continuous along the margins of detrital quartz grains and are generally uniform in intensity around individual grains except where they are superimposed by CL patches.

Although continuous CL rims are best developed in mineralized samples, they have been observed in samples without any visible U-bearing minerals. Even in mineralized samples, there are no direct relationships between continuous CL rims and U-bearing minerals. Instead, the presence of abundant U-bearing minerals in matrices and pores usually results in numerous CL patches on the margins of secondary overgrowths or CL patches superimposed on CL rims of detrital quartz grains. The latter occur either where secondary overgrowths are not developed or U-bearing minerals are present in direct contact with detrital quartz grains (i.e., uraninite and crandallite-goyazite along boundaries between detrital quartz grains and Q1 overgrowths).

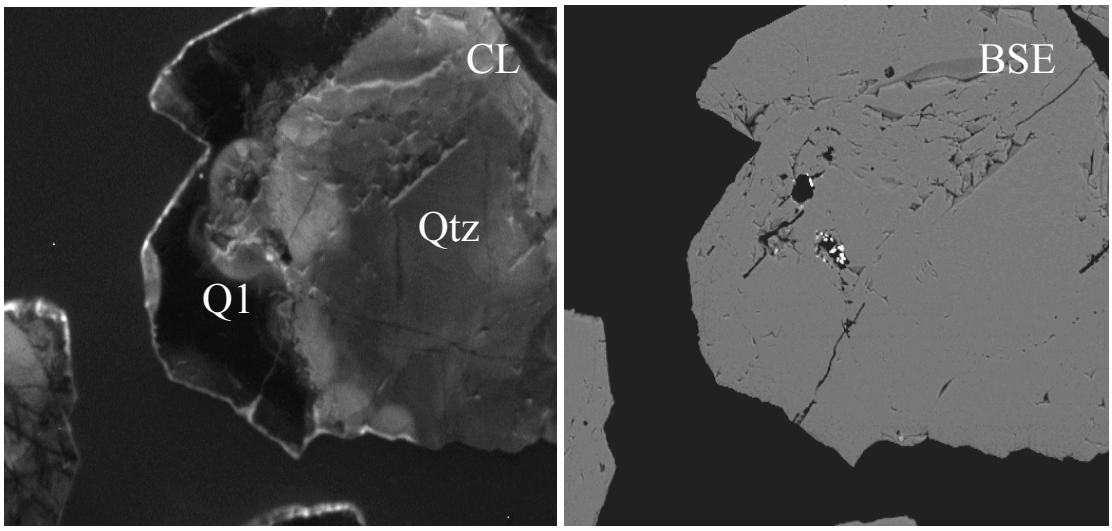

Figure 5.3: Cathodoluminescence (CL) and backscattered electron (BSE) image of sample H737-58 illustrating CL patches associated with U-rich minerals in both detrital quartz grain and secondary overgrowth Q1. Note that the patches form complete haloes around those U-rich minerals.

5.1.2 Distribution of radiation-damage-induced CL at three uranium deposits

Figures 5.4 and 5.5 illustrate the distribution of radiation-damage-induced CL in quartz from two diamond drill holes at the McArthur River deposit: MAC135A and MAC121. Bright CL haloes are present occasionally in quartz grains from all the samples that have been investigated, except the basement quartzites in which U-bearing mineral inclusions are generally absent. Similarly, CL patches are wide spread throughout the stratigraphic columns but are particularly abundant in samples containing well-developed alteration assemblages: including those from 1) the ore body, 2) the alteration haloes, 3) lithological boundaries and 4) faults, fractures and voids. Continuous CL rims, on the other hand, are more restricted in occurrence and have been observed only in samples close to mineralization at the unconformity, lithological boundaries and fractures.

For example, continuous CL rims are restricted to mineralized samples and those from the associated alteration haloes in MAC135A. The only exception is the occurrence of continuous CL rims in sample MAC135A-226, which is located close to a lithological boundary but does not contain any visible U-bearing minerals. The CL rims increase in intensity from moderate in sample MAC135A-356 (Figs. 5.4a, b) to very good in sample MAC135A-368.8 (Figs. 5.4c, d). Sandstone samples directly below this level exhibit only poor patchy to no CL. Good continuous CL rims occur again in sample MAC135A-406 (i.e. associated with uranium mineralization) and increase in intensity toward the unconformity (Figs. 5.4e, f). Therefore a well-

developed radiation-damage-induced CL is present along lithological boundaries, unconformity and near the top of the alteration haloes.

In MAC121, continuous CL rims occur on the margin of quartz grains along annealed fractures at 125 m depth (Figs 5.5 a, b). This occurrence, however, is probably better attributed to the local abundance crandallite-goyazite in fractures, which leads to continuous development of CL patches (Fig. 5.5).

Good continuous rims of sample MAC121 occur in corroded sandstone with dickite-filled pores at 185 m depth (Figs 5.2g, h) and highly corroded sandstone with abundant uraninite and other U-bearing minerals at 275 m depth (Figs 5.5c, d). The former occurrence at 185 m, where no mineralization directly contributing to this damage is observed lies directly above an aquitard where quartz overgrowths have completely occluded porosity. In addition to the detrital quartz grains with well-developed continuous CL rims in sample MAC121-275 (Figs 5.5c, d), three stages of secondary quartz are observed: 1) Q1 overgrowth with abundant U-bearing mineral inclusions, 2) Q2 overgrowth with weak oscillatory CL and 3) CL inactive euhedral quartz in cross-cutting veins. Poor to moderate continuous CL rims have also been observed directly above the unconformity in MAC121, in highly corroded sandstones with abundant magnesiofoitite.

Similar to those at the McArthur River deposit, CL haloes around U-bearing mineral inclusions have been observed in quartz grains from all parts of the Cigar Lake and the Key Lake deposits.

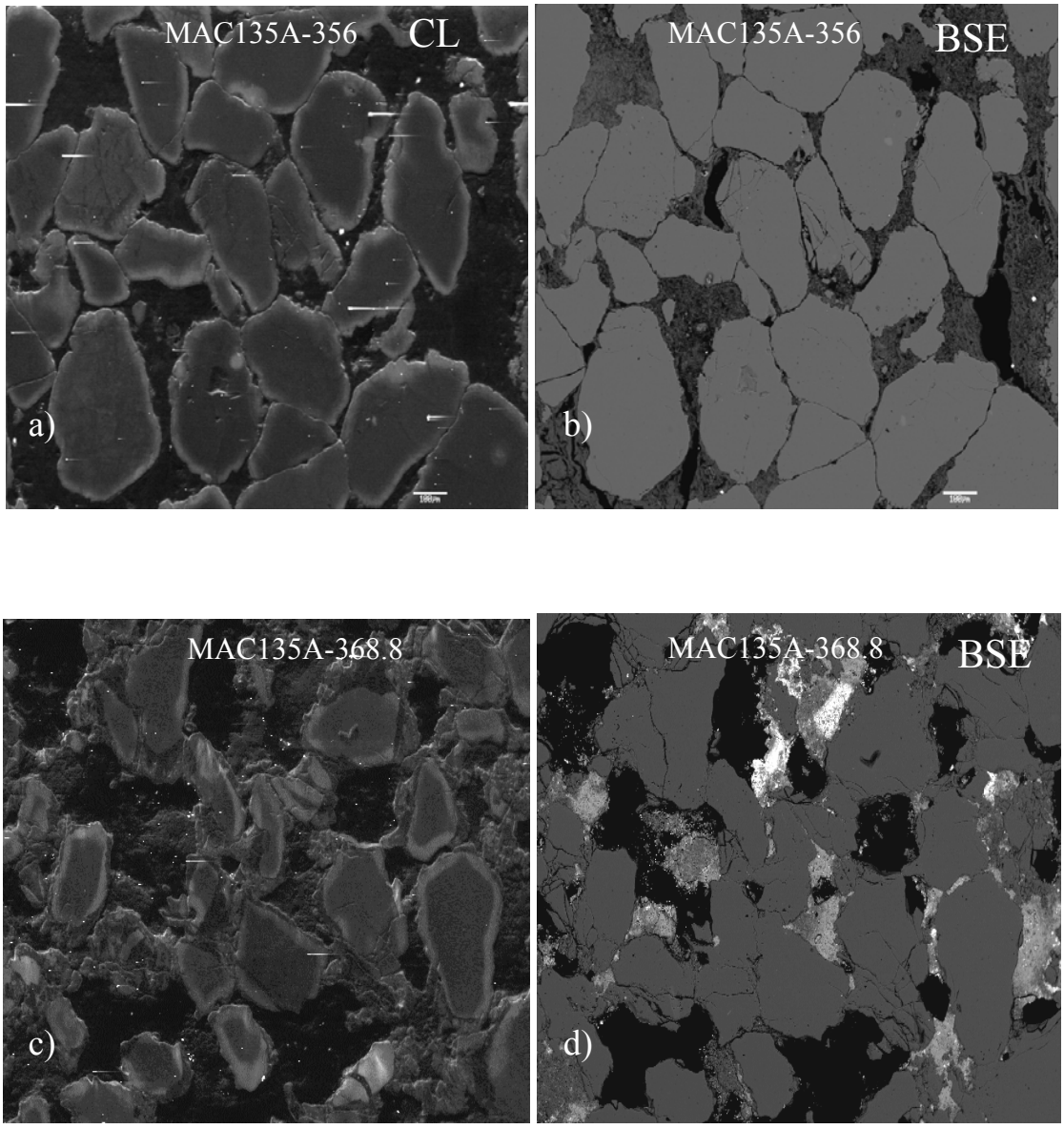
MAC135A-356
CL
a)
MAC135A-356
BSE
b)
MAC135A-368.8
c)
MAC135A-368.8
BSE
d)

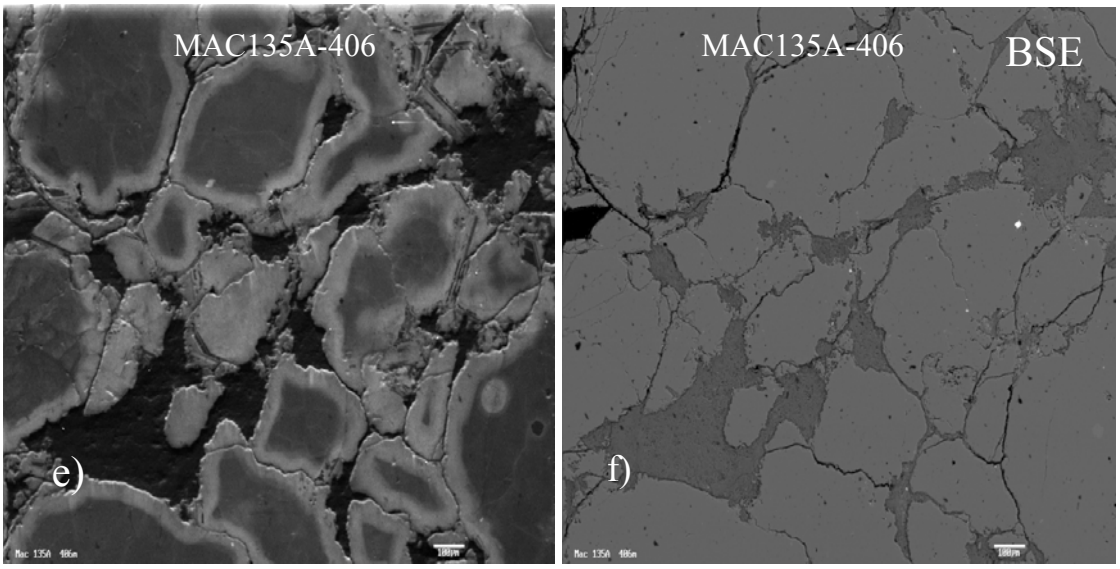

Figure 5.4: Cathodoluminescence (CL, a, c, e) and backscattered electron (BSE, b, d, f) images illustrating: a, b, c & d) the development of CL rims in samples from the siliceous cap, e & f) continuous CL rims on detrital quartz grains in a mineralized sandstone near the unconformity.

Also, CL patches associated with U-bearing minerals in matrices and pores in the Cigar Lake and Key Lake deposits are best developed in mineralised samples, alteration haloes, faults, fractures and voids. At the Cigar Lake deposit, moderate to good continuous CL rims on detrital quartz has been observed in highly altered sandstone associated with U-mineralization and alteration haloes close to unconformity.

Also poor to moderate CL rims are present along annealed fractures in overlying sandstones. However, continuous CL rims generally absent on detrital quartz grains from the Key Lake deposit, exception being the mineralised sandstone samples which exhibit weak to moderately developed rims of continuous CL.

5.1.3 CL microscopy of sample H737-58

Sample H737-58 presenting one of the most pervasively developed CL was selected for a detailed investigation of CL stability as a function of temperature.

CL images of sample H737-58 after annealing reveal that the radiation-damaged haloes and rims remain CL active up to at least 800 ºC (Fig. 5.6e) but become inactive at 900 ºC (Fig. 5.6f). Similarly, Baker and Owen (1983) noted that CL haloes in quartz do not fade noticeably at temperatures below 800 ºC.

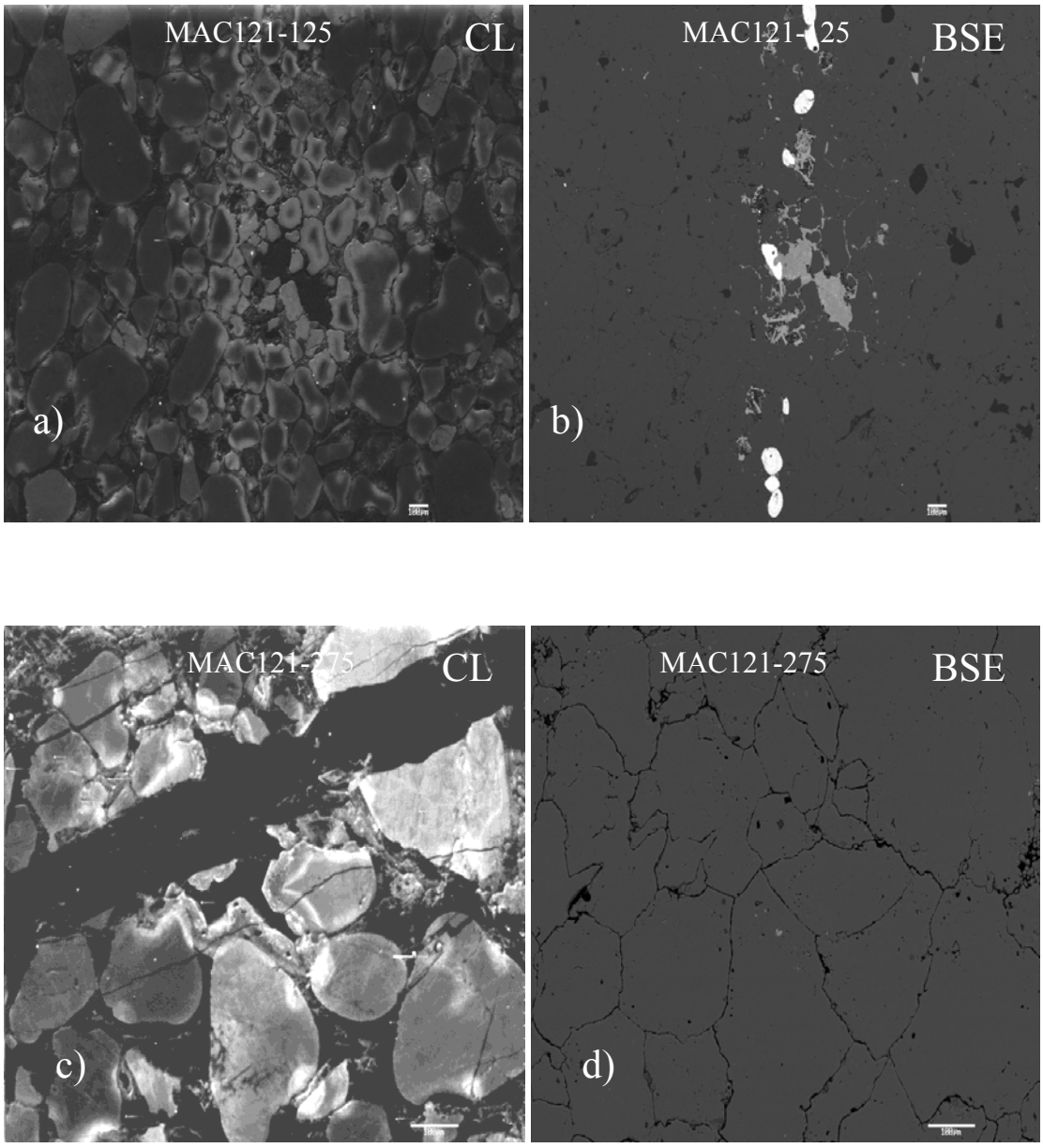

Figure 5.5: Cathodoluminescence (CL) and backscattered electron (BSE) images illustrating: a & b) CL rims associated with U-rich minerals along a fracture, c & d) Q1and Q2 secondary overgrowth on detrital grains and CL inactive quartz vein.

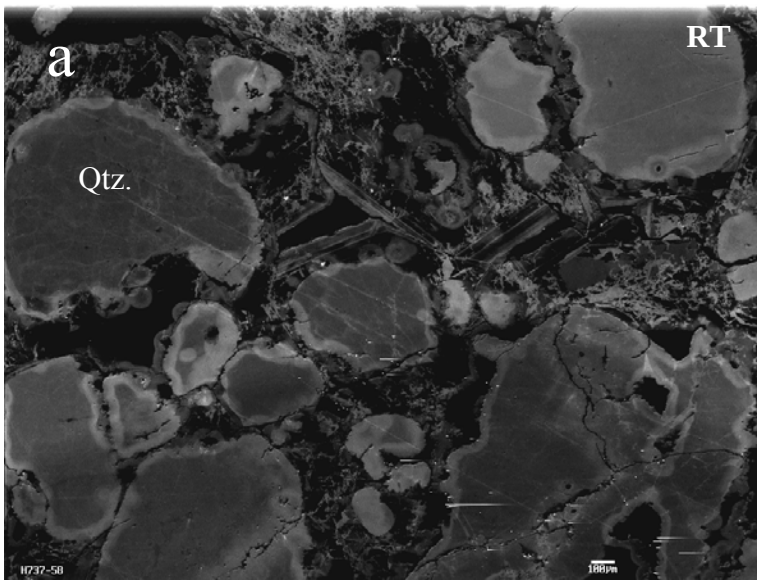
a
RT
Qtz.

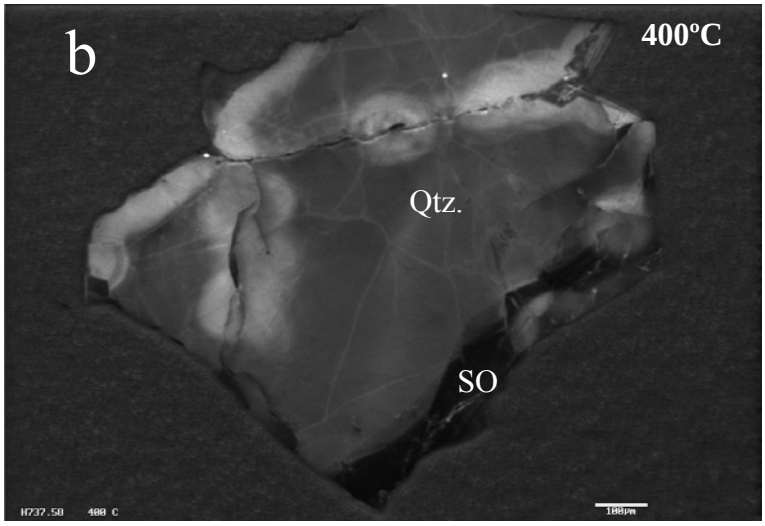
b
400°C
Qtz.
SO

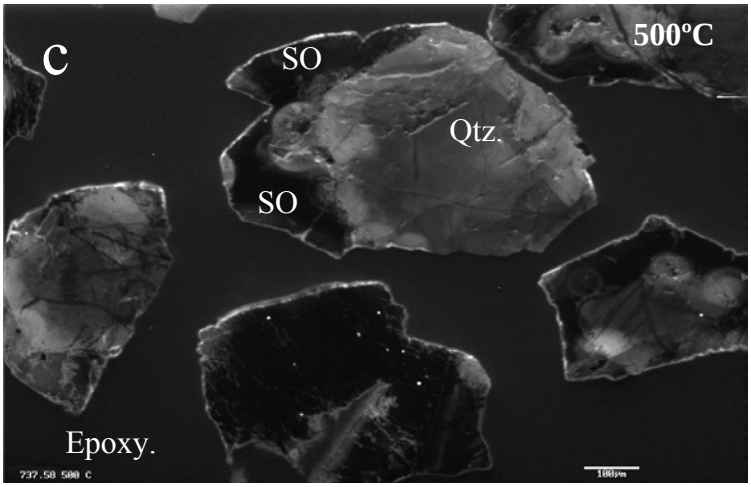
c
500ºC
SO
Qtz.
SO
Epoxy.

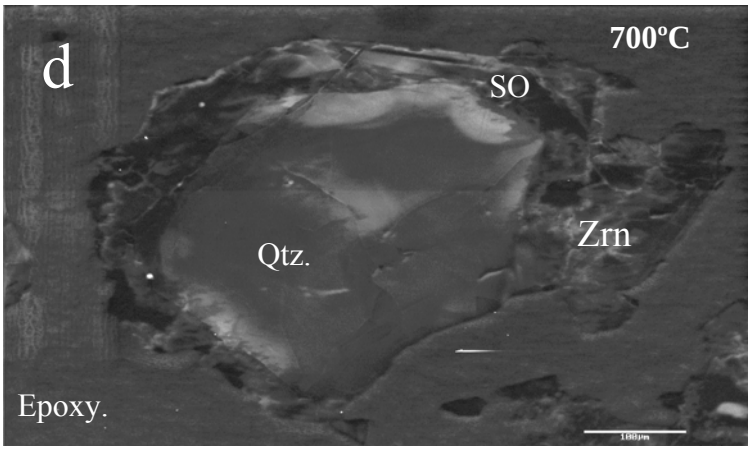
d
700ºC
SO
Zrn
Qtz.
Epoxy.

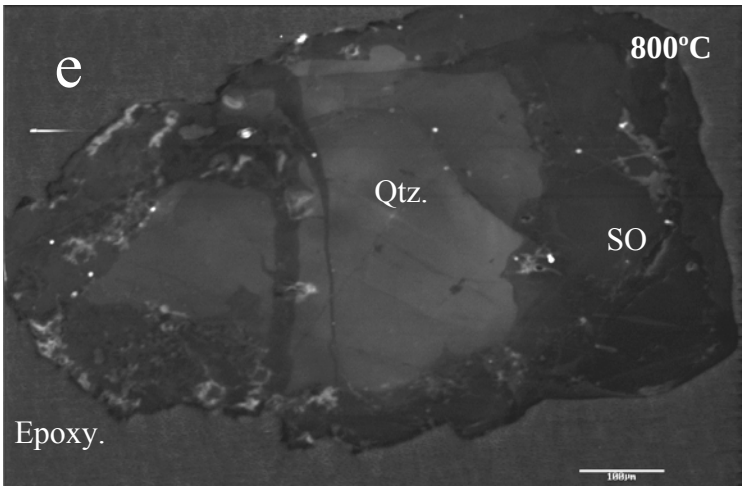
e
800ºC
Qtz.
SO
Epoxy.

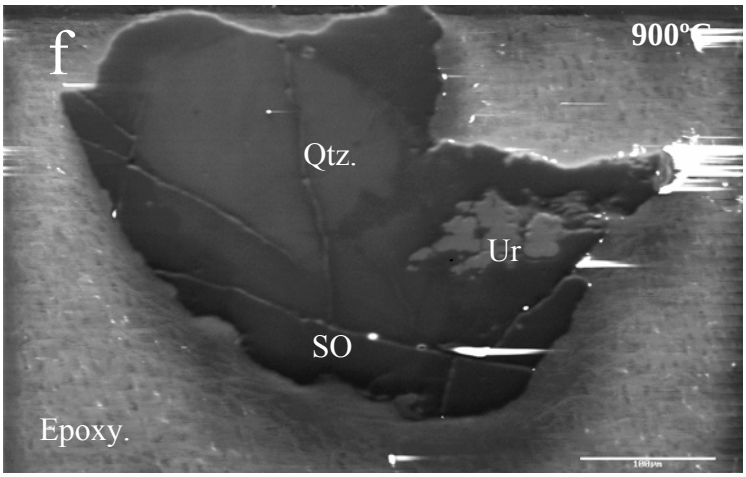

Figure 5.6: Cathodoluminescence (CL) images of sample H737-58 illustrating: a) bright CL patches and continuous rims on the boundaries and fractures of detrial quartz grains (Qtz). Note that the well-developed secondary overgrowth (SO) is relatively CL inactive and that clay minerals (mainly kaolinite, K) are also present; b) bright CL rims along the boundaries and fractures of detrital quartz grains after isochronal annealing at 400 ºC; c) well-preserved CL patches, rims and haloes in detrital quartz grains mantled by CL inactive secondary overgrowth (SO) after annealing at 600 ºC; d) well-preserved CL haloes surrounding a zircon (Zrn) inclusion in a detrital quartz and CL patches along the grain boundaries of detrital quartz after annealing at 700 ºC; e) weak but visible CL rims and haloes in detrital quartz after annealing at 800 ºC; and f) no visible CL rims on detrital quartz grains after annealing at 900 ºC. Note that no CL haloes occur around the uraninite (Ur) inclusion in the secondary overgrowth.

5.2 CL spectra of sample H737-58

The CL spectra of detrital quartz grains in sample H737-58 are characterized by two broad bands in the blue (~420 nm) and red (~620-650 nm) regions (Fig. 5.7a), whereas the CL spectra of the secondary overgrowth are as expected to have low signal-to-noise ratios (Fig. 5.7b). The CL spectra of the radiation-damaged haloes and rims are dominated by the presence of a very intensive but broad band in the ultraviolet region (~350 nm), in addition to the blue and red bands (Fig. 5.7c). Also, a comparison of the CL spectra between the radiation-damaged haloes/rims and their host grains reveals that the red-to-blue ratios of the former are invariably higher than those of the latter. This result is consistent with the observation of Götze et al. (2001), who reported a red CL for radiation-damaged haloes in quartz grains from the Witwatersrand Basin, South Africa (see also Morton 1978). However, the characteristic ultraviolet CL of the McArthur River sample was not detected in Götze et al. (2001). This discrepancy may be attributable to the different experimental conditions in the collection of CL spectra (i.e., 14 kV and 10 μA in Götze et al. 2001).

There is no systematic change in the CL spectra of the detrital quartz grains after annealing up to 600 ºC (Figs. 5.7a, d). Also, the CL spectra of the radiation-damaged haloes are similar from room temperature to 500 ºC (Figs. 5.7c, e). However, the CL spectra of the radiation-damaged haloes at 600 ºC are distinct by the disappearance of the characteristic ultraviolet band (Fig.5.7f). Also, the red-to-blue ratio in the 600 ºC spectrum of a radiation-damaged halo (Fig. 5.7f) is significantly higher than that of its undamaged detrital host (Fig. 5.7d); again pointing to a red CL characteristic of the radiation-damaged haloes (Götze et al. 2001).

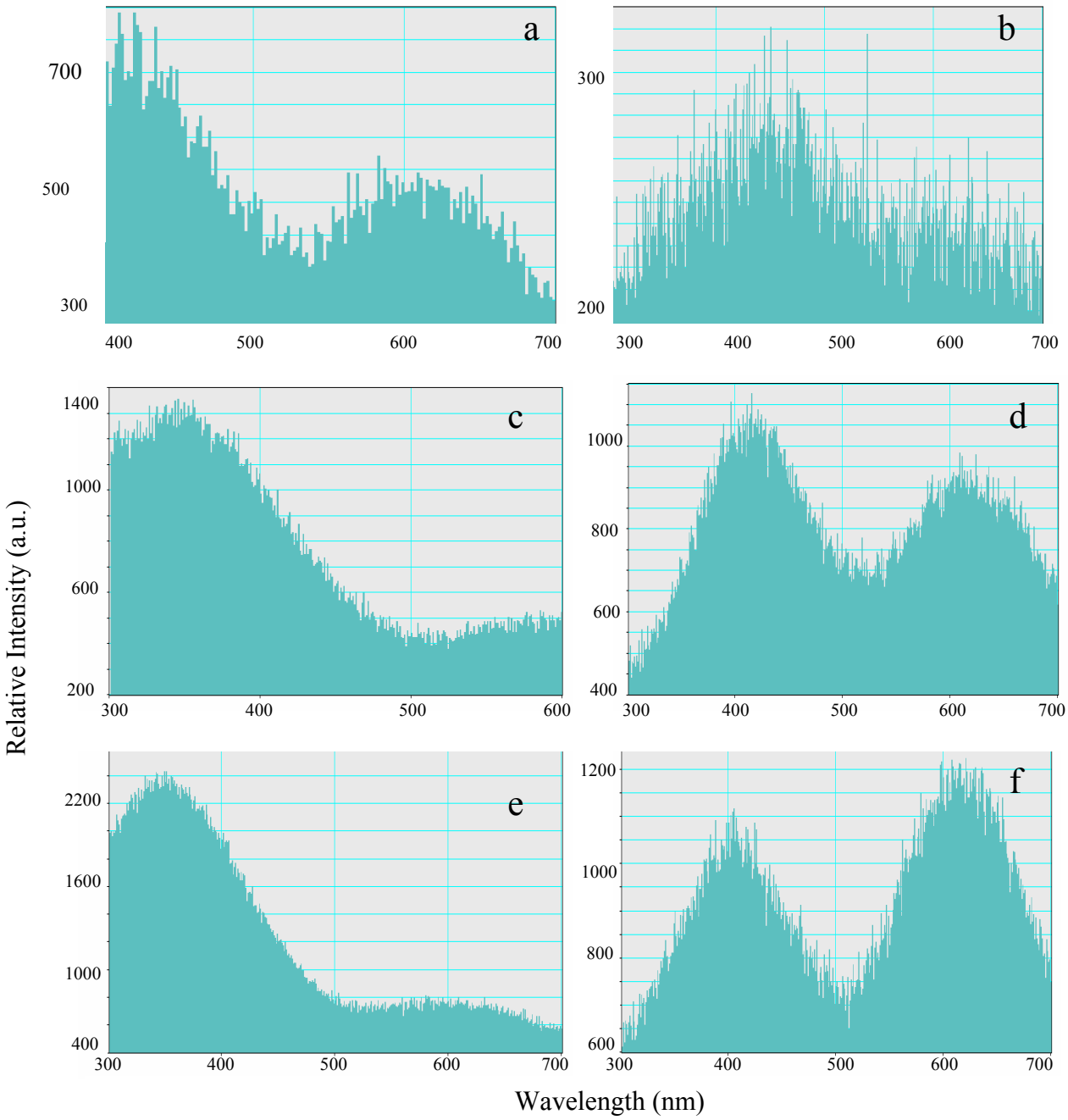

Figure 5.7: CL spectra of sample H737-58: a) undamaged area in a detrital quartz after annealing to 200 ºC; b) secondary overgrowth after annealing to 200 ºC; c) haloes surrounding uraninite after annealing to 200 ºC; d) undamaged area in a detrital quartz after annealing to 600 ºC; e) haloes surrounding uraninite after annealing to 500 ºC; f) haloes surrounding uraninite after annealing to 600 ºC.

5.3 Origin of radiation-damage-induced CL in quartz

Bright CL haloes around U- and Th-bearing mineral inclusions in quartz (and other minerals) have been demonstrated, both theoretically (Owen 1988) and experimentally (Komuro et al. 2002), to be caused by bombardments of alpha particles emitted from the ^{238}U, ^{235}U and ^{232}Th decay series.

Owen (1988) noted that the CL haloes in quartz and biotite are most likely related to bombardment of alpha particles. He reasoned that different radionuclides emit alpha particles of different kinetic energies and therefore should give rise to CL haloes of different radii. Owen (1988) used the Bragg-Kleeman rule to account for the effects of mineral density on the penetration distance of alpha particles and calculated the halo widths in quartz for alpha particles from different radionuclide (Table 5.1).

Komuro et al. (2002) performed a high-energy He^+ (4 MeV) implantation experiment on crystals of synthetic α-quartz, using a 3M-tandem ion accelerator in the Takasaki Research Centre, Japan Atomic Energy Research Institute. This experiment demonstrated that the alpha-particle-irradiated quartz crystals developed CL rims of a constant width and that the width of the CL rims is consistent with that predicted by Owen (1988). Moreover, Komuro et al. (2002) noted that the intensity of CL in the artificially irradiated quartz increases systematically with the radiation doses.

The CL haloes and rims in the Athabasca quartz grains of this study (Fig.5.2a) are similar to those reported in the literature, being characterized by a uniform width of ~35-45 μm and, therefore, attributable to alpha-particle-induced radiation damages.

Radionuclide	Energy (MeV)	Range in air (cm)	Radii, Quartz(μm)
238U decay series			
214Po	7.68	6.91	35.8 *
218Po	6.00	4.66	24.1 *
222Rn	5.48	4.05	21.0
210Po	5.30	3.84	19.9
226Ra	4.78	3.28	17.0
234U	4.77	3.21	16.6
230Th	4.68	3.11	16.1
238U	4.20	2.65	13.7
232Th decay series			
212Po	8.79	8.57	44.4 *
216Po	6.77	5.64	29.2 *
220Rn	6.28	5.00	25.9
212Bi	6.09	4.73	24.5

Table 5.1: Estimated range in air and in solids (quartz) for alpha particles emitted by various radionuclides from U and Th decay series.

CL patches (Fig. 5.2c) may be interpreted as partial development of CL haloes owing to the location of U-rich minerals outside of quartz grains. This interpretation is supported by the occurrences of U-rich minerals along boundaries between detrital quartz grains and Q1 overgrowths, where CL patches on the outer margins of detrital quartz grains and the inner margin of Q1 overgrowths join together to form complete CL haloes (Fig. 5.3).

Continuous CL rims are also characterized by a uniform width of ~35-45 μm and, therefore, are caused by alpha particle irradiation. Locally, abundant U-rich minerals, especially in high-grade ore samples, result in CL patches that superimpose on continuous CL rims (Fig. 5.1a). Moreover, continuous CL rims on detrital quartz grains also occur in samples without any visible U-rich minerals (Fig. 5.2g).

Similar continuous CL rims on quartz grains have been reported in uranium-bearing sandstones elsewhere (e.g., Colorado, Meunier et al. 1990; Witwatersrand, South Africa; Goetze et al. 2001). For example, Meunier et al. (1990) also reported that CL rims occur on quartz grains where no uranium minerals are present and interpreted them to record radiation damages after removal of uranium.

In the Athabasca Basin, continuous CL rims are present exclusively on detrital quartz grains and have been observed in sandstones with and without uranium mineralization. The occurrences of continuous CL rims in the Athabasca Basin (Key Lake, McArthur River, BJ zone and Cigar Lake) are closely associated with the unconformity, alteration haloes (siliceous cap at the McArthur River Prospect), lithological boundaries and faults/fractures. These structures are characterized by well-developed clay mineral alteration assemblages and have been interpreted to represent

pathways of uranium-bearing mineralization fluids. Therefore, one possible explanation for the restricted occurrences of continuous CL rims in association with the unconformity, alteration haloes, lithological boundaries, faults and fractures is that they record bombardments of alpha particles emitted from uranium-bearing mineralization fluids. This interpretation is supported by the commonly uniform intensity of CL rims (Fig. 5.2e, f), which is expected from U-bearing fluids. U-bearing minerals, on the other hand, result in CL patches of variable intensities (Fig. 5.2c).

Chapter 6
EPR study of naturally irradiated quartz samples

Quartz separates from 31 Athabasca samples have been investigated by powder EPR spectra (Table 4.1), which were recorded with a Bruker ESP 300E spectrometer, at the Department of Chemistry, University of Saskatchewan and a Bruker EMX spectrometer, at the Structural Science Center, University of Saskatchewan, both operating at X-band frequencies (9.5-9.7 GHz). Except that the microwave power was varied for different experiments [from 30 dB (200 μW) to 5 dB (63.3 mW)] all other experimental parameters on each spectrometer were kept constant during all measurements in order to facilitate direct comparison between the EPR spectra. In particular, all EPR spectra were collected with similar amounts of powder materials in the same quartz tube. Comparisons were made only between EPR spectra recorded with the same EPR spectrometer (i.e. Figs. 6.6 & 6.7; Figs. 6.8 & 6.9), owing to different sensitivities of the two EPR spectrometers (i.e., the Bruker EMX instrument is approximately 100 times more sensitive than the Bruker ESP 300E machine).

Sample H737-58 with one of the most pervasively developed CL was selected for detailed EPR experiments before and after annealing experiments and HF

treatments. EPR measurements of quartz separates of sample H737-58 after isochronal annealing experiments were made at room temperature and microwave powers of 10, 15, 20 and 30 dB. The EPR spectra of the quartz separate after the isochronal annealing experiments are hereafter designated by their respective annealing temperatures (e.g., the 100 °C EPR spectra) in order to distinguish them from those without isochronal annealing experiments (i.e., the room-temperature or RT spectra). It should be emphasized that all EPR spectra of quartz separates after isochronal annealing experiments were recorded at room temperature. EPR spectra of the HF-treated quartz separates were collected at room temperature for the following microwave powers: 10, 20 and 30 dB.

6.1 Powder X-band EPR spectra of sample H737-58

6.1.1 RT EPR spectra

The RT EPR spectrum of H737-58 at 30 dB (Fig. 6.1) is characterized by the presence of the well-known oxygen vacancy centre E_1' (Weeks 1956; Feigl & Anderson 1970; Jani et al. 1983; Weil 1984). This centre is easily recognizable by its almost uniaxial g values (2.00178, 2.0005 and 2.00033) and by its saturation behaviour. The structural model of E_1' involves a vacancy left by a missing bridging O^{2-} ion between two Si atoms and the unpaired electron in a dangling tetrahedral sp^3 orbital of a single Si atom bonded to three O atoms (Yip & Fowler 1975).

The RT EPR spectra of sample H737-58 at higher microwave powers revealed the presence of additional paramagnetic centres, which are indicated by a multitude of lines in the g region from ~2.005 to ~2.049 (Fig. 6.1).

However, these EPR lines on the RT spectra are difficult to interpret owing to their similarities in saturation behavior. In particular, several EPR lines with effective g values around 2.002-2.007 have very similar dependence on microwave power.

Due to the great difficulty in distinguishing between the various paramagnetic defects present, a different approach was necessary and therefore isochronal annealing experiments were performed in order to selectively anneal the paramagnetic centers and simplify the analysis.

6.1.2 EPR spectra after isochronal annealing experiments

Annealing of defects commonly occurs through the recombination of electron centres and hole centres and depends on the properties of the defects and temperature. The recombination of electron and hole centres is commonly divided into two types: 1) a correlated recombination leading to first-order kinetics and 2) an uncorrelated recombination leading to second-order kinetics. The correlated recombination is commonly investigated by isochronal annealing experiments. Isochronal annealing experiments, also known as pulse annealing, treat samples at a fixed duration at different temperatures.

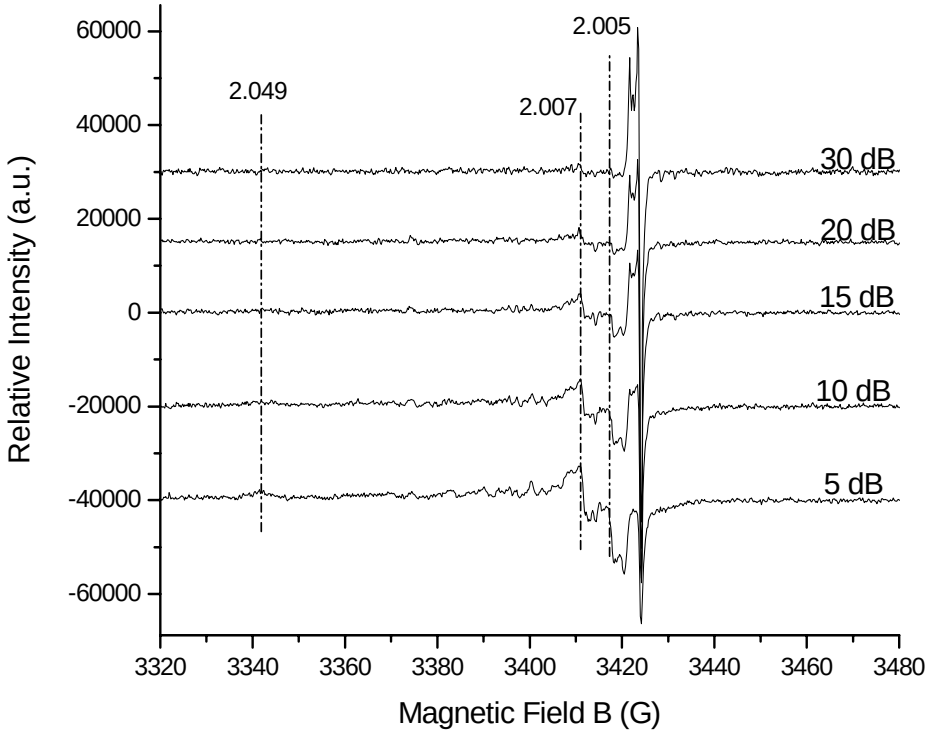

Figure 6.1: Comparison of powder X-band EPR spectra of sample H737-58 without isochronal annealing collected at room temperature and various microwave powers (30 to 5 dB). Also the effective g values of selected peaks are labeled.

In this study, isochronal annealing experiments have been made for sample H737-58 in order to better distinguish the different paramagnetic centers in this sample. The 100 and 200 ºC EPR spectra of sample H737-58 are similar in the number of peaks to those of their RT counterpart at the same microwave powers (Fig. 6.2). However, the overall intensities of the 100 and 200 ºC spectra increase significantly relative to those of the RT spectra (Fig. 6.2).

Also, the overall intensity of the 200 ºC spectra is notably higher than that of the respective 100 ºC counterparts. The 300, 400 and 450 ºC spectra are also similar in the number of peaks to those of the RT, 100 and 200 ºC spectra at the same microwave powers (Fig. 6.2). However, the overall intensities decrease gradually and systematically from the 200 ºC to the 300, 400 and 450 ºC spectra (Fig. 6.2).

A comparison of these EPR spectra at different temperatures permits a possible correlation of the various peaks to specific paramagnetic centers. For example, the broad peak at g = ~2.05 varies systematically with two other broad peaks at g = 2.008 and 2.0045 (Fig. 6.2). These g values are closely comparable to those of a silicon vacancy hole center O_2^{3-}/M^+ (M=Li and Na; Mashkovtsev et al. 1978).

The broad EPR peak at g = ~2.008 not only increases in intensity from RT to 200 ˚C but also becomes a well-resolved doublet at 200 ˚C (Fig. 6.2). Similarly, the broad peak at g = ~2.005 increases in intensity from RT to 200 ˚C and becomes a doublet at 100 and 200 ˚C. However, these peaks have different behaviors at 300 ˚C. For example, the line at g = ~2.005 almost disappear at 300 ˚C, whereas the lines at g = ~2.008 have

decreased intensities but remain well resolved (Fig. 6.2). This result suggests that these peaks at g = ~2.005 and ~2.008 most likely belong to different paramagnetic centers. In particular, the doublet with g = 2.00535 and 2.00405 is similar to those of the silicon vacancy hole center O_2^{3-}/H^+(II) (g_1 = 2.0007, g_2 = 2.0042 and g_3 = 2.0052; Mashkovtsev et al. 1978). The g_1=2.0007 peak of this center is expected to overlap with the E_1' center. Another similar silicon vacancy hole center O_2^{3-}/H^+(I) (g_1 = 2.0021, g_2 = 2.0074 and g_3 = 2.0295; Mashkovtsev et al. 1978) is indicated by the g=~2.03 peak (Fig. 6.2). In addition, the characteristic doublet of the E_1' center in the 100 ºC spectra is distorted (Fig. 6.2) and is probably attributable to interference from an unknown center with a g = ~2.0005.

The 500 and 550 ºC spectra show further decreases in overall intensities relative to their low-T counterparts of the same microwave powers and are characterized by the disappearance of the E_1' center (Fig. 6.2). The O_2^{3-}/M^+, O_2^{3-}/H^+(I) and O_2^{3-}/H^+(II) centers remain well resolved on the 500 and 550 ºC spectra, especially those obtained at high microwave powers.

The 600 ºC spectra are characterized by one broad peak of very low intensity at g = ~2.001, whereas all other paramagnetic centers observed at lower temperatures disappear (Fig. 6.2). The line shape suggests that an isotropic paramagnetic center can't be responsible for the broad peak at g=~2.001. This g factor is similar to the g_1 values of two O_2^- peroxy centers in artificially irradiated amorphous SiO_2 and α-quartz (PR_1: g_1 = 2.0018, g_2 = 2.0078 and g_3 = 2.067; PR_2: g_1 = 2.0020, g_2 = 2.0085 and g_3 = 2.027; Griscom 1989).

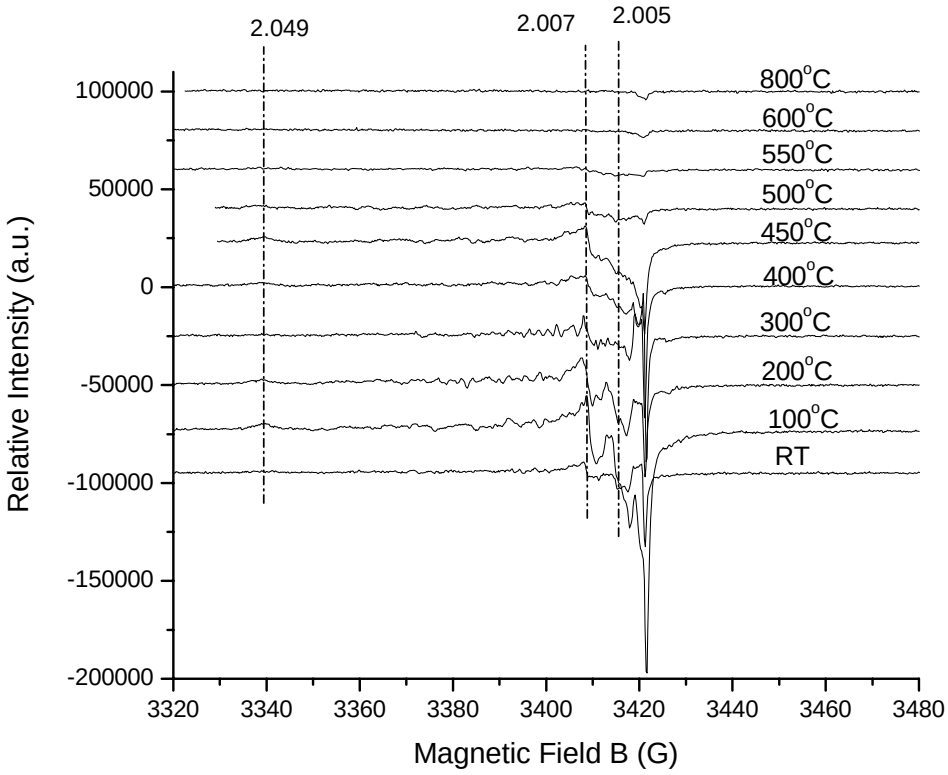

Figure 6.2: Comparison of powder X-band EPR spectra of sample H737-58 before (RT) and after isochronal annealing at 100, 200, 300, 400, 450, 500, 550, 600 and 800 ºC, collected at room temperature and microwave power of 10 dB.

Therefore, the aforementioned doublet at g = ~2.008 may be attributable to the peroxy centers. Moreover, the presence of the characteristic $g_3 = 2.027$ peak on the low-T spectra and the high-microwave-power 550 ºC spectra (Fig. 6.2) suggests that peroxy center PR_2 is present in sample H737-58.

The peroxy radicals were first observed in neutron- and γ-irradiated fused silica (Friebele et al. 1979; Griscom & Friebele 1981; Griscom 1989). Friebele et al. (1979) and Griscom & Friebele (1981) noted that post-irradiation heat treatments to 500 ºC destroy virtually all paramagnetic centers but the peroxy radicals in fused silica. These results are consistent with the preservation of the peroxy radicals on the 600 and 700 ºC spectra (Fig. 6.2). Friebele et al. (1979) proposed that the peroxy radicals in fused silica involved the preexistence of bridging peroxy linkages (≡Si–O–O–Si≡), which share an electron to form peroxy radicals by irradiation and/or thermal treatment (Griscom 1989).

In order to obtain additional information on the existent paramagnetic defects from sample H737-58, microwave power dependence experiments were performed on the sample annealed at 200 ºC. Increasing the microwave power a distinction between the paramagnetic defects can be made as a result of differences in their saturation behavior. Therefore a microwave power dependence EPR experiments will provide further information on the radiation-induced defects and complete the spectral analysis.

6.1.3 Dependence of paramagnetic centers on microwave power at 200ºC

Figure 6.3 presents the 200 ºC EPR spectra, which have the highest overall intensities (see above), to illustrate the dependence of individual paramagnetic centers on microwave power (i.e., saturation behavior). Center E_1' decreases in intensity with increasing microwave power and is saturated at 5 dB. All other centers, however, increase in intensity with increasing microwave power up to about 5 dB and then decrease in intensity with further increasing microwave power. For example, the two peroxy centers appear as a broad peak at g=~2.008 at 20 dB but are well resolved at 15 dB and higher microwave powers (Fig. 6.3). The O_2^{3-}/M^+, O_2^{3-}/H^+(I) and O_2^{3-}/H^+(II) centers also become well resolved at 10 dB and higher microwave powers.

6.1.4 Spectral simulation and confirmation of paramagnetic centers in sample H737-58

Spectral simulations of the EPR spectra of sample H737-58 were done using EPR-NMR software of Mombouquette et al. (1996) and the results are shown in Fig. 6.4. The spectral simulations included the following six known paramagnetic defects: E_1', O_2^{3-}/H^+(I), O_2^{3-}/H^+(II), O_2^{3-}/M^+, PR_1 and PR_2.

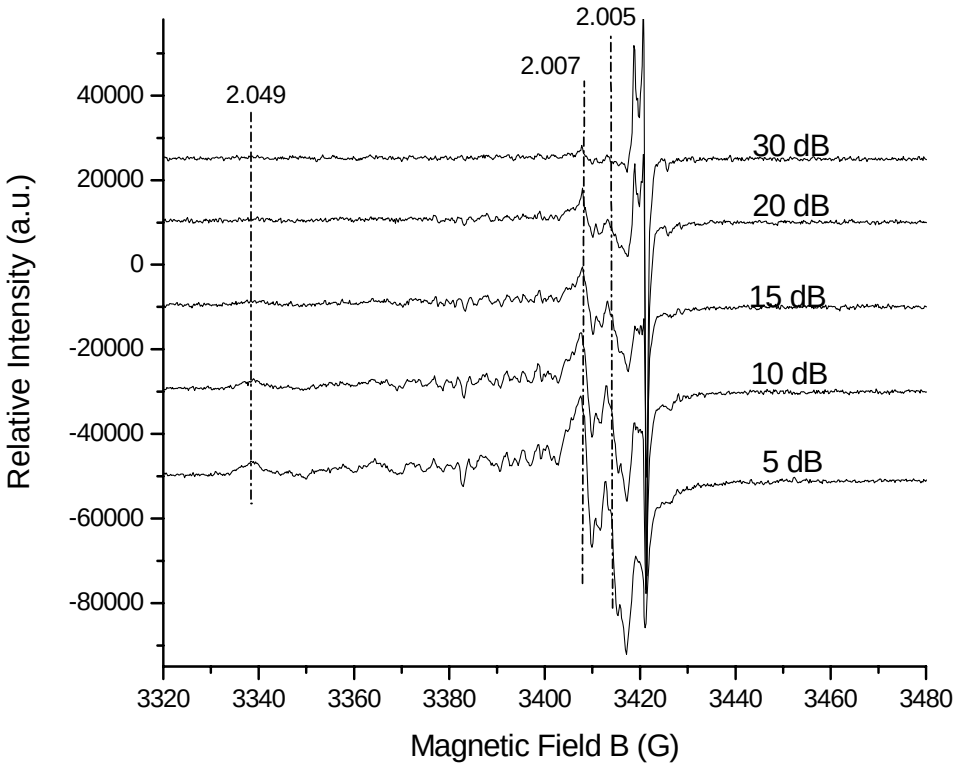

Figure 6.3: Comparison of powder X-band EPR spectra of sample H737-58 after isochronal annealing at 200 ºC, collected at room temperature and various microwave powers (30 to 5 dB).

Spectral simulations have been made after each annealing experiment using the six paramagnetic centers in different ratios. After heating the sample at 500 ºC and 700 ºC, the only two paramagnetic centers needed for spectral simulations were the two peroxy centers. Figure 6.4 shows that the simulated and observed spectra at various temperatures and microwave powers are all in reasonable agreements.

Table 6.1 summarizes the thermal properties and saturation behavior of the defect centers present in sample H737-58, and makes a comparison with the previously reported data in the literature.

The absolute concentrations of paramagnetic centers in sample H737-58 could not be determined due to the absence of a concentration standard. The possibility of using E_1' center as a concentration standard was considered but the great overlapping of the defect centers made difficult any quantitative analysis.

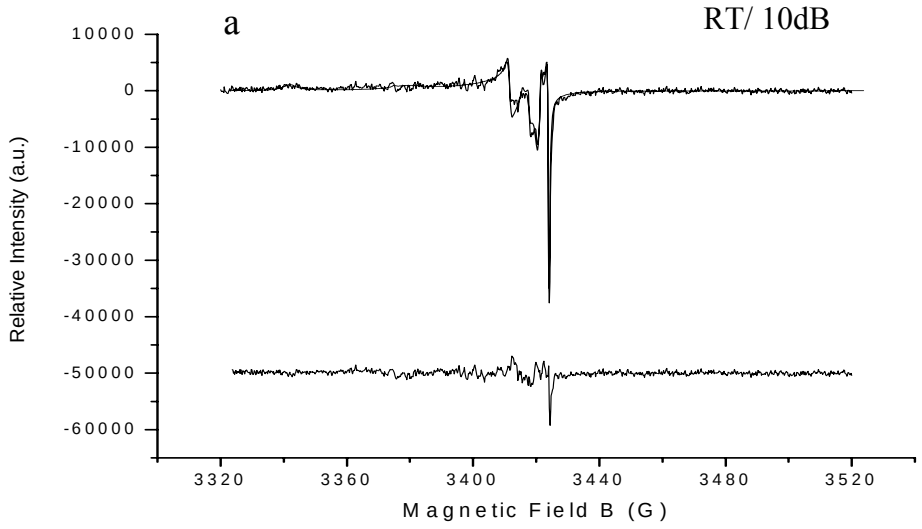

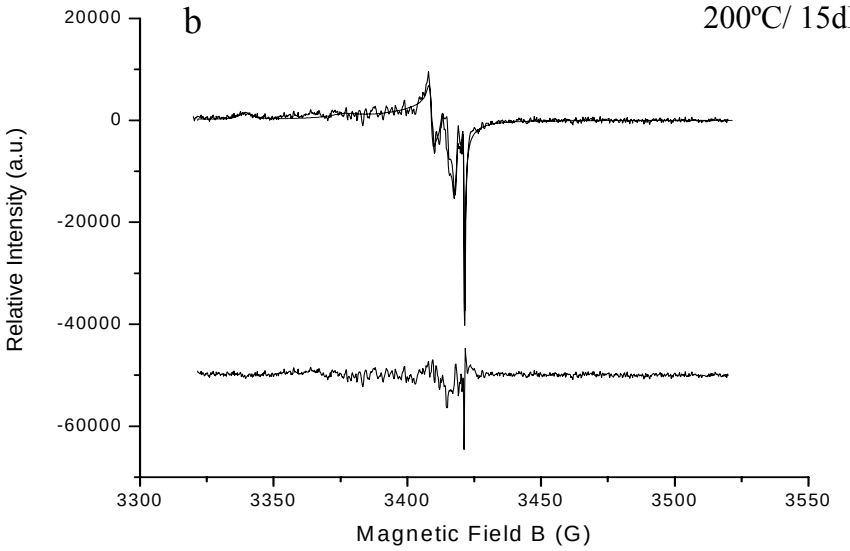
b
200ºC/ 15dB
20000
0
-20000
-40000
-60000
Relative Intensity (a.u.)
3300
3350
3400
3450
3500
3550
Magnetic Field B (G)

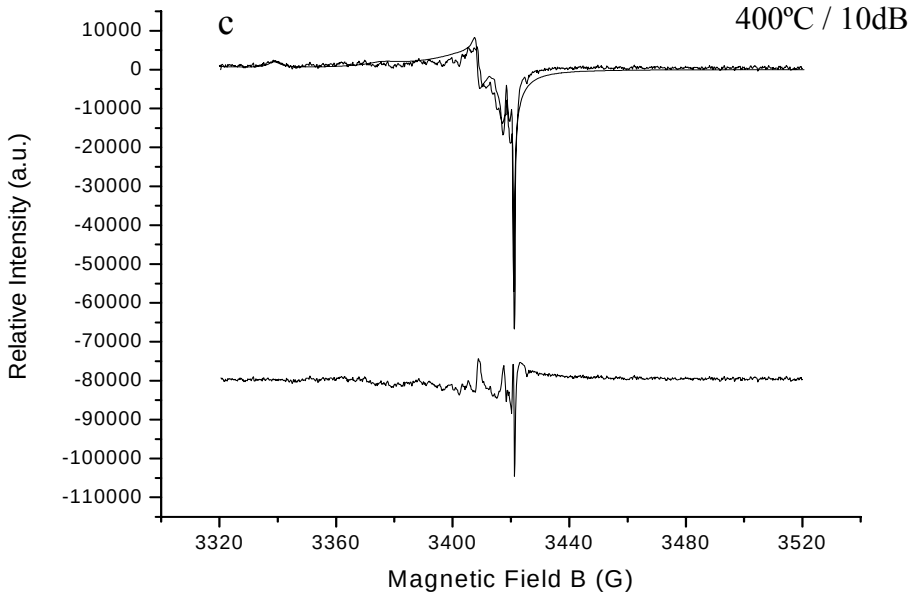
c
400ºC / 10dB
10000
0
-10000
-20000
-30000
-40000
-50000
-60000
-70000
-80000
-90000
-100000
-110000
Relative Intensity (a.u.)
3320
3360
3400
3440
3480
3520
Magnetic Field B (G)

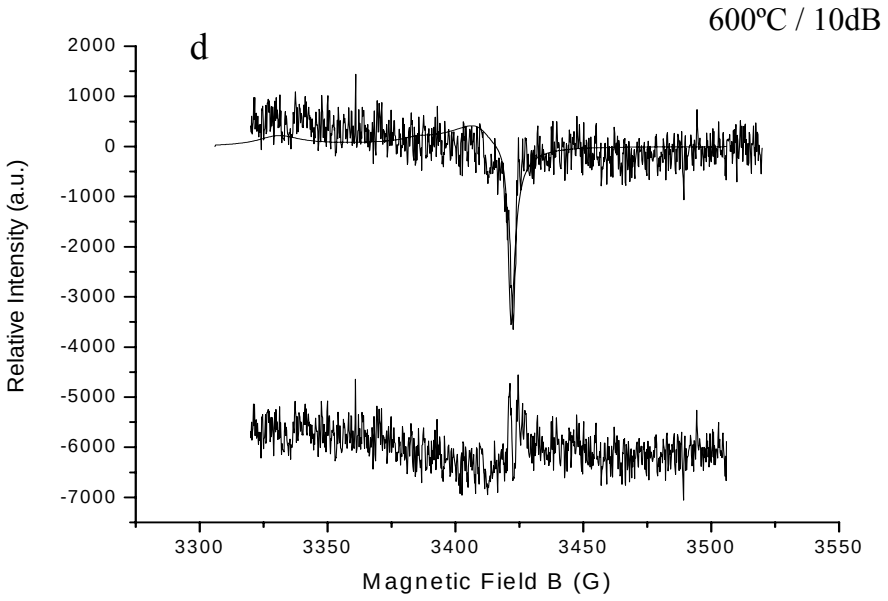

Magnetic Field B (G)

Figure 6.4: Comparison of simulated and observed powder X-band EPR spectra of H737-58 at various temperatures and microwave powers: a) room temperature and 10 dB; b) 200 ºC and 15 dB; c) 200 ºC and 5 dB; and d) 600 ºC and 5 dB. Spectral simulations for a), b) and c) included the following six centers:1) oxygen vacancy center E_1', 2-3) peroxy centers (PR_1, Griscom & Friebele 1981;PR_2 Griscom 1989), 4-6) silicon vacancy hole centers [O_2^{3-}/H^+ (I), O_2^{3-}/H^+ (II) and O_2^{3-}/M^+, Mashkovtsev et al. 1978]. Note that only two peroxy centers are needed to simulate the spectra at and above 600 ºC. Also shown are the difference spectra. A notable signal with an effective g = 2.001 is visible on all difference spectra and is probably attributable to an isotropic center of this g value reported by Serebrennikov et al. (1982).

Defect	g factors		Structural Model	Saturation Behavior		Thermal Properties		Ref
	Previous Studies	This study		Previous Studies	This study	Previous Studies	This Study	
E_1'	2.00178 2.0005 2.00033	2.00178 2.0005 2.00033	an unpaired electron in an O vacancy, where the electron occupies a dangling sp^3 hybrid orbital of Si bonded to three O atoms	saturated at 100 mW	saturated at 100 mW	annealed at ~400ºC	present up to 500ºC	1, 2 3, 4
Peroxy 1	2.067 2.0078 2.0018	2.067 2.0076 2.001	-a hole trapped by an O_2 molecule at an O^{2-} site in the form of Si-O-O	no data	active at 159 mW	present at 700ºC	present at 800ºC	3, 5 7, 8
Peroxy 2	2.027 2.0085 2.0020	2.027 2.0085 2.0018	a hole trapped by a O_2 molecule at an O^{2-} site in the form of Si-O-O	no data	active at 159 mW	present at 700ºC	present at 800ºC	6
O_2^{3-}/M^+	2.049 2.0076 2.0024	2.0495 2.0076 2.0024	involving a Si vacancy that leads to a hole trapped by two O atoms forming O_2^{3-} with M^+ (Li^+ or Na^+) as charge compensators	no data	active at 159 mW	no data	present up to 500ºC annealed at 600ºC	9
O_2^{3-}/H^+(I)	2.0295 2.0074 2.0021	2.0285 2.0074 2.0021	involving a Si vacancy that leads to a hole trapped by two O atoms forming O_2^{3-} with H^+ as a charge compensator	no data	active at 159 mW	no data	present up to 500ºC annealed at 600ºC	9
O_2^{3-}/H^+(II)	2.0052 2.0042 2.0007	2.00528 2.004 2.0007	involving a Si vacancy that leads to a hole trapped by two O atoms forming O_2^{3-} with H^+ as a charge compensator	no data	active at 159 mW	no data	present up to 500ºC annealed at 600ºC	9

Table 6.1: Summary of paramagnetic defects in sample H737-58. Reference is 1, Feigle & Anderson 1970; 2, Silsbee 1961; 3, Ikeya 1993; 4, Griffits et al 1982; 5, Griscom et al. 1981; 6, Griscom 1989; 7, Friebele et al 1979; 8, Weeks 1956; 9, Mashkovtsev et al. 1978.

6.1.5 EPR spectra of HF-treated sample H737-58

After subsequent steps of HF treatment, sample H737-58 shows a significantly decrease in intensity for all paramagnetic centres (Fig. 6.5). However, centre E_1' shows a smaller increase in intensity and becomes better resolved relative to other centers (Fig. 6.5). The small increase in the relative intensity of centre E_1' is readily attributable to the greater decrease in intensity of all the other paramagnetic centres. Therefore, centre E_1' is probably distributed evenly throughout the quartz grains. The other paramagnetic centres are most likely concentrated in the radiation-damaged rims and fractures that were preferentially dissolved away during the HF treatments and therefore their intensity is dramatically reduced after the dissolution experiment.

6.1.6 Interpretation of powder X-band EPR spectra

The X-band EPR spectra of the CL active H737-58 sample are very similar to those of shock-metamorphosed quartz reported by Serebrennikov et al. (1982). They interpreted their EPR spectra to arise from a combination of the well-known E_1' centre and five other oxygen hole centres with similar g factors. However, their identification of the five oxygen hole centres was based solely on the g values taken from the spectra. These authors noted that two of the five proposed oxygen hole centres have g values close to the silicon vacancy hole centres O_2^{3-}/M^+ and O_2^{3-}/H^+(I) reported by Mashkovtsev et al. (1978).

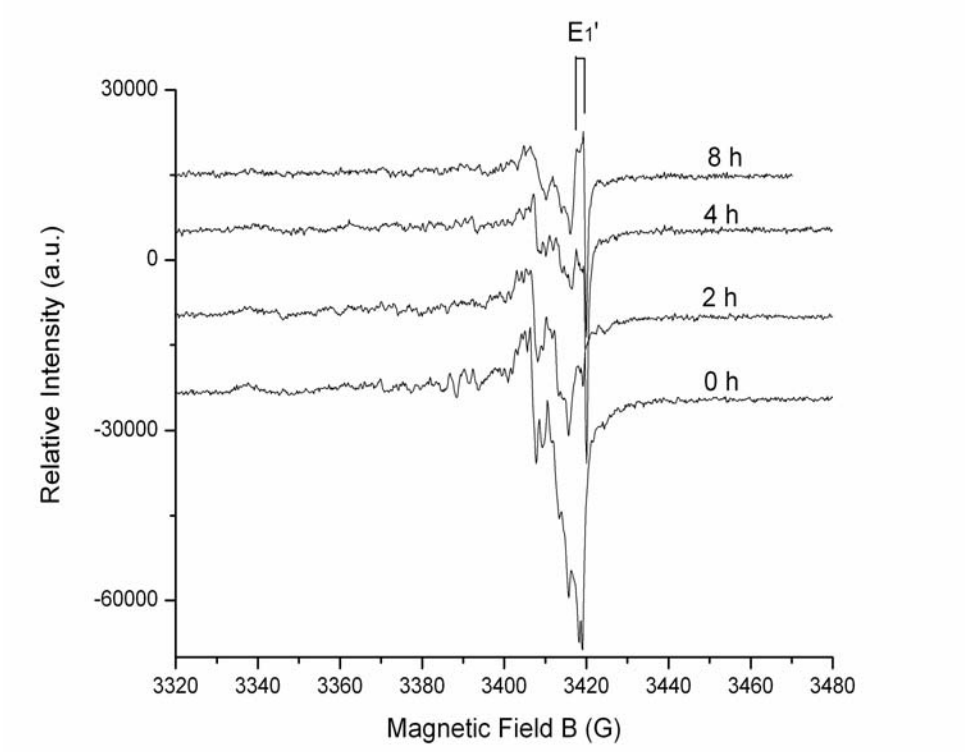

Figure 6.5: Comparison of X-band EPR spectra of H737-58 before and after sequential HF treatments. Note that all spectra were collected at a microwave power of 10 dB. Also labeled is center E_1'.

Serebrennikov et al. (1982) attributed the proposed oxygen hole centres to vacancies associated with dislocations induced by shock metamorphism. Our X-band EPR measurements show that a sandstone sample of mixed quartz, coesite and stishovite from the Meteor Crater, Arizona, is EPR silent. Serebrennikov et al. (1982) observed the paramagnetic centres in the shock-metamorphosed quartz only after X-ray irradiation. Therefore, their proposed oxygen hole centres whether related to shock metamorphism or not, are activated by X-ray irradiation.

Götze et al. (1999) reported another similar X-band EPR spectrum for a red agate, from Lauterbach, Germany and obtained the g factors for two paramagnetic centres which, following Bershov et al. (1978) and Serebrennikov et al. (1982), were assigned to the O^{-} and O_2^{3-} centres. A comparison of their simulated and observed spectra shows significant discrepancies (Plötze 2004, Person. Commun.), pointing to the presence of additional paramagnetic centres. Moreover, the g factors of their O^{-} center are similar to those of the O_2^{3-}/M^{+} center (Mashkovtsev et al. 1978), the Ge trapped-hole center in quartz (Hayes & Jenkin 1986) and the self-trapped hole (STH_1) in amorphous SiO_2 (Griscom 1989), whereas the g factors of their O_2^{3-} centre are indistinguishable from those of the peroxy radical PR_2 (Griscom 1989).

The six paramagnetic defects (E_1', O_2^{3-}/H^{+}(I), O_2^{3-}/H^{+}(II), O_2^{3-}/M^{+}, PR_1 and PR_2; Table 6.1) have been previously reported in the literature but mostly from artificially irradiated materials (Weeks 1956; Friebele et al. 1979; Griscom & Friebele 1981, Griscom 1989). Therefore, the presence of these paramagnetic centers in H737-58 represents the first example in naturally irradiated quartz. It is noteworthy that McMorris

(1970) reported similar EPR spectra of quartz from sandstones and attributed them to fossil alpha damage. However, the EPR spectra reported by McMorris (1970) only allowed the identification of the E_1' center. Our EPR spectra of the HF-treated samples also confirmed that all paramagnetic centers, except for E_1', are concentrated largely in the alpha-particle-damaged patches/rims.

Table 6.1 shows that the naturally occurring paramagnetic centers in sample H737-58 have similarities and significant differences in thermal properties and saturation behaviors to their respective counterparts in artificially irradiated materials. For example, Friebele et al. (1979) reported that the peroxy centers remain stable after annealing to 700 ˚C (see also Griscom & Friebele 1981; Griscom 1989), similar to the preservation of these centers to 700 ˚C in H737-58 (Table 6.1). Also, the saturation behavior of the E_1' center is similar to that reported in literature, but the presence of this center on the 450 ˚C spectra is unusual in comparison with its commonly reported annealing temperature of 360-380 ˚C (Ikeya 1993). Similarly, Mashkovtsev et al. (1978) reported that the silicon vacancy hole centers are stable only up to 300-400 ˚C, whereas the O_2^{3-}/H^+(I), O_2^{3-}/H^+(II) and O_2^{3-}/M^+ centers are all detected on the high-microwave-power 550 ˚C spectra of H737-58. It remains uncertain whether the high annealing temperatures of these radiation-damage-induced paramagnetic centers in H737-58 are attributable to high dosage of natural irradiation in this sample.

6.2 EPR spectra of other Athabasca quartz samples

The EPR spectra of all CL active samples from the Athabasca basin show the same paramagnetic defects as those observed in sample H737-58 (Figs. 6.5, 6.6). It is noteworthy that the EPR spectra of several CL inactive samples (e.g., MAC135A-105, MAC135A-146, see Fig. 6.5), although low in signal-to-noise ratios, also reveal defect centres identical to those observed in sample H737-58. This result confirms that EPR is more sensitive in detecting dilute defect centres than CL (e.g., Weil et al. 1994; Pan et al. 2003).

6.2.1 Distribution of radiation-damage-induced defects in the McArthur River deposit

The relative intensity of EPR spectra of quartz separates in diamond drill hole MAC135A (Figs. 6.6 & 6.7) correlates with the results obtained from CL microscopy. For example, the intensities of the EPR spectra of CL inactive samples near the surface are relatively low (e.g., MAC135A-106 and 146; Fig. 6.6). The EPR spectra of CL active sample MAC135A-285, which is from the siliceous cap near the top of the alteration halo at this deposit, reveal pronounced radiation-damage-induced defects. Also, the EPR spectra of CL inactive sample MAC135A-376 and CL poor sample MAC135A-386 (Fig. 6.7) are low in intensity. The EPR spectra of uranium-mineralized samples MAC135A-406 and 416, which are close to the unconformity, again show well-resolved radiation-damage-induced defects. This result confirm CL observations (see Chapter 5) that the distribution of radiation

damages in the Athabasca Basin is not a simple function of depth but rather is associated preferentially with alteration haloes and the unconformity.

In diamond drill hole MAC121 a similar distribution of radiation defects is observed. The EPR intensity again correlates with the observed radiation-damages-induced CL (Figs. 6.8, 6.9). Only poor to moderate continuous CL rims have been observed above the unconformity in MAC121. The intensities of EPR spectra of samples from this hole (Fig. 6.8) are notably lower than those of samples from MAC135A (Figs. 6.6). Below the unconformity at 420 m, the EPR spectra of quartz from two basement rocks also disclose radiation defects, but their signal-to-noise ratios are noticeably lower than that of MAC121-385 and are probably attributable to radiation damages from associated U- and Th-bearing mineral inclusions.

In diamond drill hole MAC223 (Fig. 6.10), the EPR spectra of the sample at 225 m, which is close to a lithological boundary and contains well-developed radiation-damage-induced CL (see Chapter 5), have well resolved radiation defects. Sample MAC223-635 is a mineralized sample in the basement and the relative high EPR intensity is correlated to uranium mineralization. However, the EPR intensity of sample MAC223-655, an altered quartzite in the basement, decreases dramatically.

Therefore, EPR measurements of quartz samples from diamond drill holes MAC121, MAC223 and MAC135A demonstrate that the concentration of paramagnetic centres does not depend on the depth but rather is associated with specific geological settings such as lithological boundaries, alteration haloes and the unconformity (Fig.6.6, Fig. 6.7, Fig. 6.8, Fig. 6.9 and 6.10).

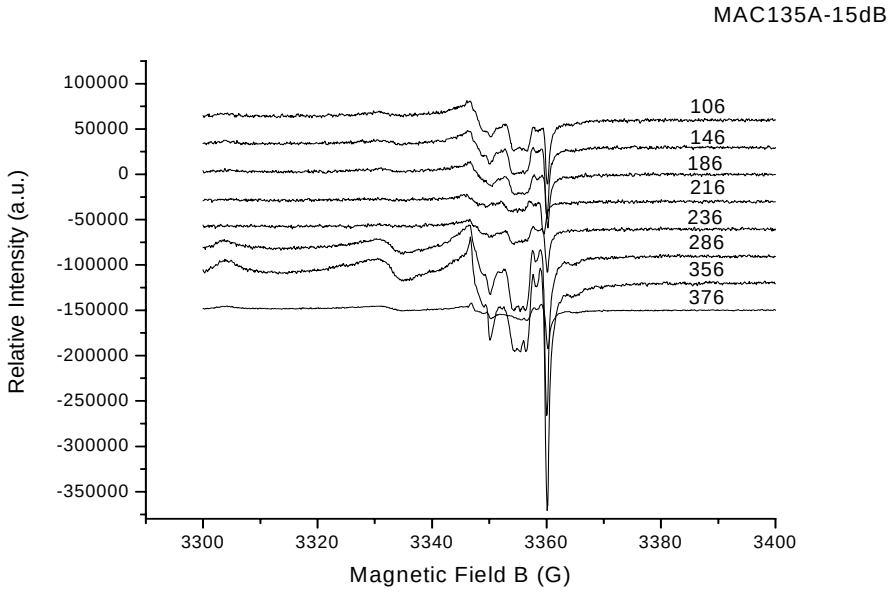

Figure 6.6: EPR spectra of quartz samples from diamond drill hole MAC135A at different depths from 106 to 376 m.

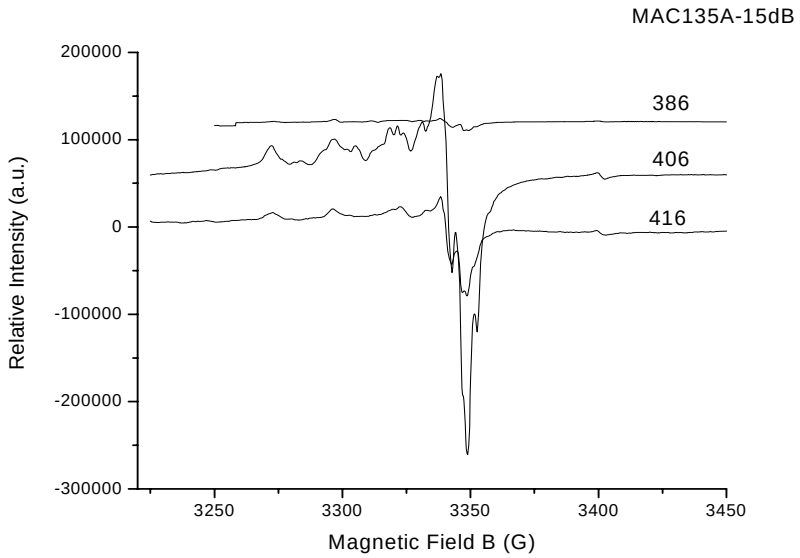

Figure 6.7: EPR spectra of quartz samples from diamond drill hole MAC135A at three different depths 386m, 406m and 416m.

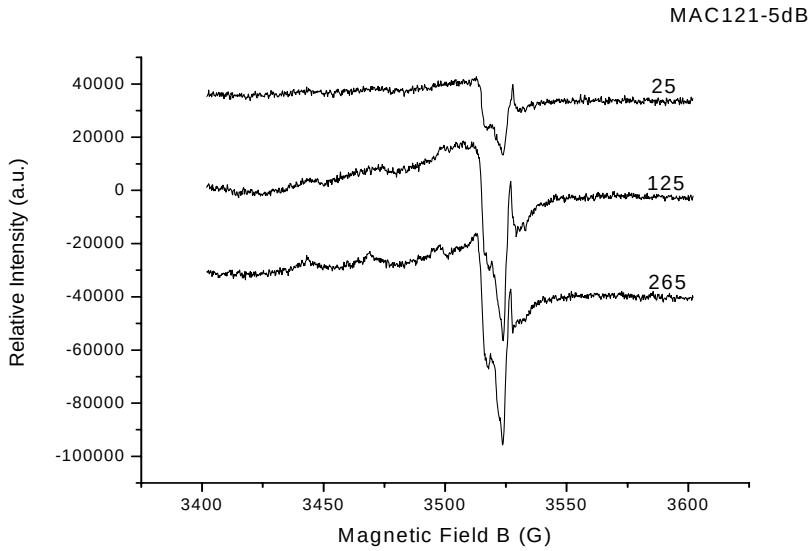

Figure 6.8: EPR spectra of quartz samples from diamond drill hole MAC121 at three different depths 25m, 125m and 265m.

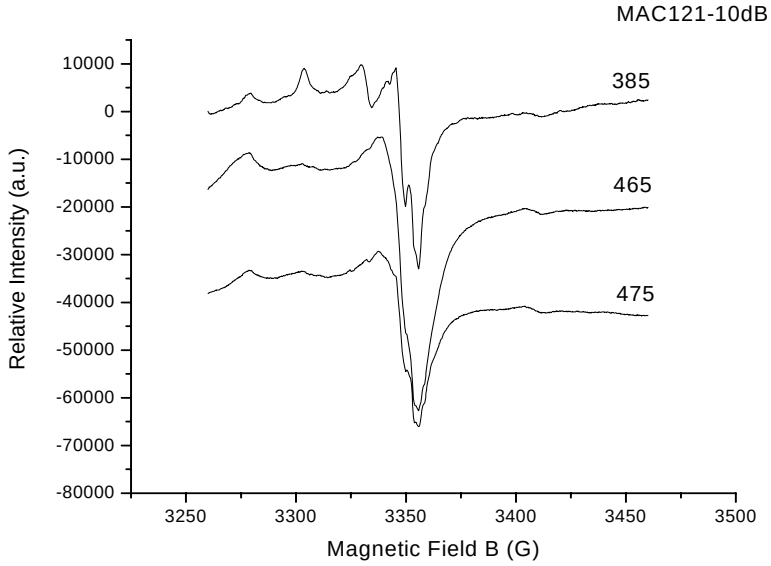

Figure 6.9: EPR spectra of quartz samples from diamond drill hole MAC121 at three different depths 385m, 465m and 475m.

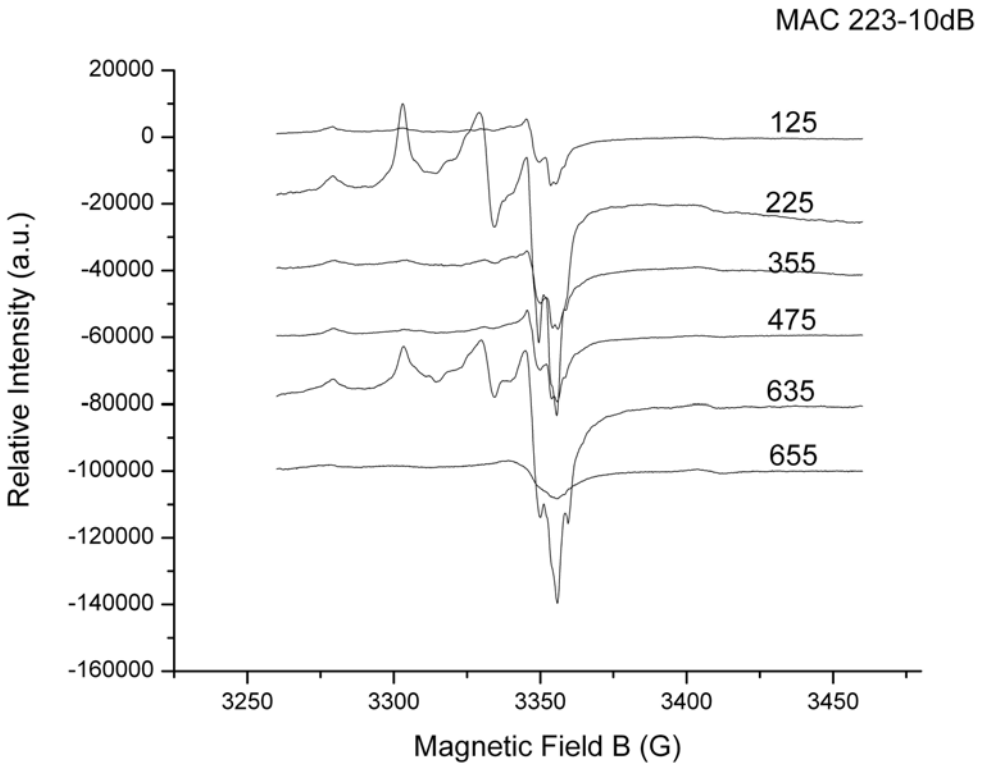

Figure 6.10: EPR spectra of quartz samples from diamond drill hole MAC223 at different depths.

6.2.2 Distribution of radiation-damage-induced defects in the Key Lake deposit

Similar to the McArtur River deposit, the EPR spectra of quartz separates from samples of the Key Lake deposit show the same radiation defects as those observed in H737-58. In addition, the EPR spectra of the CL inactive samples from the Key Lake deposit show the presence of those radiation defects. Moreover, the distribution of radiation-damage-induced defects in sandstone samples from the Key Lake deposit is associated with specific geological settings. For example, the EPR spectrum with the highest intensity is observed for a mineralized sample DDH2217-71 close to the unconformity (Fig. 6.11).

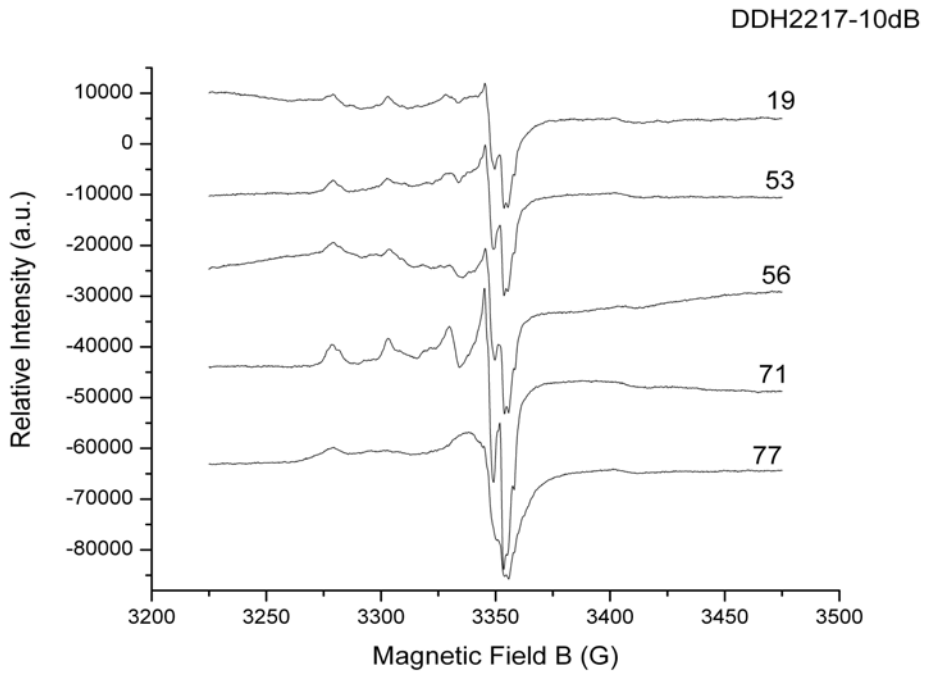

Figure 6.11: EPR spectra of quartz samples from diamond drill hole DDH2217 at different depths.

6.3 EPR of HF-treated samples

In addition to sample H737-58, HF dissolution experiments have also been performed for 4 other samples in order to determine the distribution of radiation-damage-induced defect centers in Athabasca quartz. Two of the measured samples (DDH2217-254 and MAC223-635) are CL active, whereas the other two (MAC135A-106 and 376) are CL inactive but exhibit well-resolved radiation-damage-induced defects on their EPR spectra.

Figure 6.12 compares the observed and calculated intensities of six EPR peaks (i.e., g = 2.0005, 2.007, 2.005, 2.029, 2.049, 2.016, representing the six paramagnetic centers as identified in sample H737-58, Table 6.1) in the four samples before and after HF treatments.

The EPR intensities of the silicon vacancy hole centers and the peroxy centers in the CL active samples after HF treatments are significantly lower than their counterparts before treatments (Fig. 6.12). As discussed in Section 6.1.5, the apparent increase in EPR intensity of the E_1' center after HF treatment is attributable to removal of peak interferences from the other centers. This observation is supported by a comparison of the observed and calculated intensities of those centers after HF treatments. Here, the EPR intensities after HF treatments are calculated on the basis of mass reduction and an assumption that all paramagnetic centers are evenly distributed in the sample volume. It is noteworthy that the calculated EPR intensities of the silicon vacancy hole centers and the peroxy centers in the CL active samples are notably higher than the observed values, whereas the calculated

EPR intensities of E_1' center are lower than the observed values. These results support observations from sample H737-58 that the silicon vacancy hole centers and the peroxy centers in these CL active samples are concentrated in the rims and fractures that are preferentially dissolved during HF treatments, whereas the E_1' center is probably evenly distributed in the quartz grains.

The EPR intensities of the CL inactive samples follow closely the calculated values due to mass reduction (Fig.6.12). This result may be explained by the absence of radiation-damage induced patches and continuous rims along the margins of the CL inactive samples. In the CL inactive samples radiation damages may be associated with the occurrences of U- and Th-bearing mineral inclusions only, which are randomly distributed in quartz grains. Therefore, the HF treatment of the CL inactive samples does not preferentially remove the damaged regions, thus the EPR intensities of the radiation defects decrease proportionally to the mass reduction.

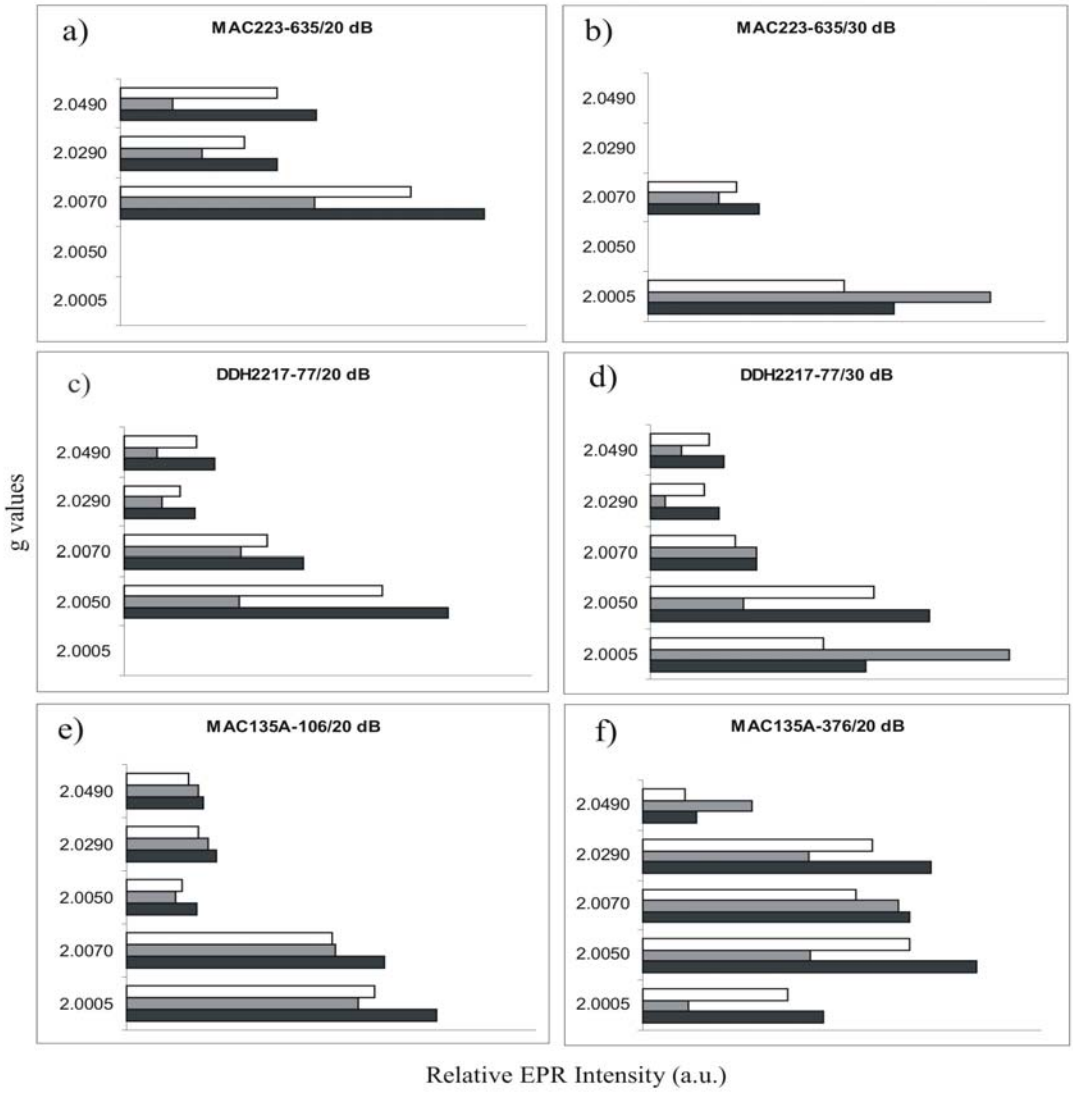

Figure 6.12: Comparison of EPR intensities of six paramagnetic centers in quartz before and after HF treatment. Also shown for comparison are calculated EPR intensities of these centers on the basis of mass reduction after HF treatments. a) and b) sample MAC223-635 at 20 and 30 dB, respectively; c) and d) sample DDH2217-77 at 20 and 30 dB, respectively; e) sample MAC135A-106 at 20 dB; and f) sample MAC135A-376 at 20 dB. Note that center E_1' (g = 2.0005) is better resolved at 30 dB, whereas the other centers are better resolved at 20 dB.

Chapter 7

Discussions and geological implications

7.1 Correlation between CL spectra and paramagnetic centres

Numerous previous studies have hypothesized that various types of luminescence in quartz are related to structural defects in this mineral (Stevens Kalceff & Phillips 1995; Götze et al. 2001 and references therein). Most of the proposed structural defects (e.g., Götze et al. 2001) are paramagnetic or become paramagnetic after artificial irradiation and, hence, can be characterized by EPR spectroscopy. However, there have been relatively few examples of integrated luminescence (including CL) and EPR studies in the past (e.g., Plötze & Wolfe 1996; Götze et al. 1999, 2001). Also, correlations between CL emission bands and paramagnetic defects identified by EPR are difficult.

The present study documented CL spectra of radiation-damaged areas in quartz before and after a series of isochronal annealing experiments. Also, the EPR measurements on the isochronally annealed samples allowed a detailed documentation of the thermal properties of the paramagnetic defects associated with natural alpha-particle-induced radiation damages in quartz. These results allow a good correlation

between the characteristic CL emission bands and specific paramagnetic defects in quartz on the basis of their thermal behaviors (Table 6.1). The characteristic ~350 nm band associated with the CL haloes/rims of H737-58 is annealed below 600 ˚C (Fig. 5.7e). Similarly, the silicon vacancy oxygen hole centers [O_2^{3-}/M^+, O_2^{3-}/H^+(I) and O_2^{3-}/H^+(II)] are associated with radiation damages and are annealed between 550 and 600 ˚C. Therefore, one (or combinations) of these oxygen holes centers may be responsible for the ultraviolet CL in the radiation-damaged haloes/rims. Center E_1', on the other hand, is not restricted to the radiation-damaged areas and is annealed at ~500 ˚C and, therefore, is unlikely to be responsible for this ultraviolet CL. Powder X-band EPR experiments of annealed samples also show that the peroxy radicals are the only paramagnetic centers stable at and above 600 ˚C. It is possible, therefore, that the peroxy centers may be responsible for the ~620-650 nm CL in the radiation-damaged haloes/rims, which remains active up to at least 800 ˚C but is annealed out at 900 ˚C.

Rink et al. (1993) reported a ~330 nm thermoluminescene (TL) band in pegmatitic quartz and attributed it to either the presence of feldspar impurities or oxygen vacancies. The present study shows that the oxygen vacancy center E_1' is unlikely to be directly responsible for the characteristic ultraviolet CL in the radiation-damaged area. Demars et al. (1996) reported a ~340 nm CL peak in sandstone samples from the Paris Basin and attributed it to the $[AlO_4/Li]^+$ center. The ICPMS analysis of H737-58 showed that Al is a significant trace element but Li was below its detection limit. The absence of the $[AlO_4/Li]^+$ center in our X-band EPR spectra is probably attributable to the fact that this center is detectable only below 35 K. However, the

$[AlO_4/Li]^+$ center is expected to be distributed throughout the volume of the quartz grains and, hence, is unlikely to be responsible for the ~350 nm CL that is restricted to the radiation-damaged haloes and rims (Fig. 5.7). The $[TiO_4/Li]^+$ center proposed by Plötze & Wolf (1996), which is readily detectable by EPR at room temperature but is not observed in H737-58, is also unlikely to be responsible for the ~350 nm CL in the radiation-damaged haloes/rims.

Götze et al. (2001) attributed the radiation-damaged-induced ~650 nm CL in the Witwatersrand quartz to nonbridging oxygen hole centers (NBOHC) with several precursors (such as hydroxyl group and peroxy linkages; cf. Stevens Kalceff & Phillips 1995). Luff and Townsend (1990) observed that the 650 nm CL in synthetic quartz grows with radiation dose and that the damage is not recoverable once the electron beam is removed. These observations led Luff & Townsend (1990) to suggest that the ~650 nm CL is related to a permanent defect such as oxygen vacancy centers. Siegel & Marrone (1981) and Redmond et al. (1992) suggested that the ~620-650 nm photoluminescence (PL) and CL are probably related to oxygen hole centers. The present study shows that the ~620-650 nm CL in the radiation-damaged haloes/rims remain active to at least 800 ºC, whereas most paramagnetic centers including oxygen vacancy and silicon vacancy hole centers are all annealed below 600 ºC. NBOHC, on the other hand, is not observed in H737-58 and is known to be unstable above 500 ºC (Stapelbroek et al. 1979). Therefore, NBOHC or oxygen vacancy centers cannot be responsible for the radiation-damage-induced CL at ~620-650 nm.

7.2 Formation of peroxy centers in the Athabasca quartz

The present discovery of the peroxy centers in the Athabasca quartz is particularly noteworthy for the following two reasons. First, this is the first report of peroxy centers in natural quartz. Second, these peroxy centers are most likely responsible for the characteristic red CL in the radiation-damaged quartz. Similar to previous reports of peroxy radicals in neutron- and γ-irradiated fused silica (Friebele et al. 1979; Griscom & Friebele 1981; Griscom 1989), the HF experiments demonstrate that these centers in the Athabasca quartz concentrate in the radiation-damaged areas. Therefore, the origin of these peroxy centers in the Athabasca quartz is most likely related to nuclear radiation processes in this uranium-mineralized basin.

Peroxide in natural minerals is rare and has been reported only recently in two uranyl minerals: studtite and metastudtite (Burns & Hughes 2003; Hughes et al. 2003). Studtite and metastudtite occur in close association with other uranium minerals (e.g. uraninite) in nature and have been reported to be important alteration products of nuclear waste (Sattonnay et al. 2001; Amme 2002; Burns & Hughes 2003). Hughes et al. (2003 and reference herein) suggested that studtite and metastudtite might grow by incorporating peroxide created from alpha radiolysis of water. By analogy, the peroxy centers in the Athabasca quartz, might have formed first from alpha radiolysis of water (i.e. U-bearing mineralization fluids) and were then incorporated into the damaged areas by diffusion (i.e. promoted by radiation damage of the quartz structure). Alternatively, the peroxy centers in the Athabasca quartz might have formed from alpha radiolysis of water already present in the damaged areas, where alpha radiolysis

is most likely related to U- and Th-bearing mineral inclusions and water might occur in fluid inclusions in quartz or incorporated into the damaged areas from grain boundaries.

7.3 Implications for uranium mineralization

This study demonstrated that detrital quartz grains of Athabasca sandstones are readily distinguishable from their secondary overgrowths on the basis of overall CL activity (i.e., the latter either CL inactive or weak in CL; Fig. 5.1). Also, the CL patterns (albeit weak in intensity) of the two generations of overgrowths are shown to be different: Q1 with irregular CL patterns and Q2 with oscillatory and/or sector CL signifying growth patterns. Moreover, quartz grains of Athabasca sandstones are characterized by common occurrences of radiation-damage-induced CL. Bright CL haloes in detrital quartz grains of Athabasca sandstones are mostly associated with zircon, whereas those in secondary overgrowths are associated with crandallite-goyazite, xenotime, uraninite, rutile, monazite and fluorapatite. Q1 overgrowths, especially those in mineralized samples close to the unconformity, commonly contain more abundant U-bearing mineral inclusions (and, hence, numerous CL haloes) than Q2. Therefore, CL imaging, including radiation-damage-induced CL, is a useful tool for establishing quartz paragenesis in Athabasca sandstones. Another notable feature of the radiation-damage-induced CL is their high annealing temperatures (i.e. stable after annealing up to 800 °C, Owen 1988; Botis et al. 2005). Therefore, radiation-damage-induced CL is applicable to metamorphosed sedimentary basins.

Chapter 6 discussed that continuous CL rims on the Athabasca quartz grains most likely record alpha particles emitted from U-bearing mineralization fluids. If this interpretation is correct, this type of radiation-damage-induced CL provides a direct visual record for the movement of U-bearing mineralization fluids in the Athabasca Basin. Indeed, the restricted distribution of continuous CL rims at the Cigar Lake and McArthur River deposits suggests a potential application of radiation-damage-induced CL in exploration for new deposits in sedimentary basins. In particular, well-developed continuous CL rims have been observed in sandstones close to the unconformity away from the McArthur River deposit. Therefore, the occurrence of radiation-damage-induced CL, particularly continuous rims, is an excellent indicator for uranium mineralization. However, the general lack of continuous CL rims on quartz grains in samples close to the unconformity at the Key Lake deposit and other parts of the Athabasca Basin is surprising and may be attributable to low levels of alpha-particle-induced radiation damages, which are below the detection limit of CL. This interpretation has been confirmed by our EPR results. We caution, therefore, that an absence of the characteristic radiation-damage-induced CL in quartz grains from sedimentary basins can not be taken as an indicator for the absence of uranium mineralization.

In contrast to the pervasive development of continuous CL rims on detrital quartz grains in sandstones at the Cigar Lake and McArthur River deposits, this type of radiation-damage-induced CL is conspicuously absent on quartz grains from Athabasca basement rocks underlying those two high-grade deposits, including highly

altered basement rocks from fault zones that are interpreted to represent the conduits for basement fluids during the formation of the uranium deposits. Similarly, continuous CL rims have not been observed on quartz grains in any basement rocks at the Key Lake deposit and other parts of the eastern Athabasca Basin. This absence of continuous CL rims on quartz grains in basement rocks indicates that basement fluids were poor in uranium; supporting previous genetic models that uranium mineralization in the Athabasca Basin resulted from interactions of U-bearing oxidizing basinal fluids and U-poor reducing basement fluids (Hoeve & Quirt 1984; Kotzer & Kyser 1995; Fayek & Kyser 1997).

Most genetic models for the formation of uranium deposits in the Athabasca Basin favoured that the main event of uranium mineralization was related to oxidizing basinal fluids after an early diagenetic fluid responsible early silicification (i.e., Q1 overgrowth; Kotzer & Kyser 1995; Fayek & Kyser 1997). The exclusive occurrence of the continuous CL rims on detrital quartz grains, which are truncated by secondary overgrowths (Fig. 5.1a), suggests that uranium mineralization in the McArthur River deposit must have commenced during this early diagenetic event. This suggestion is supported by the presence of U-bearing minerals along boundaries between detrital quartz grains and Q1 overgrowths. The common occurrence and local abundance of U-bearing minerals, including crandallite-goyazite, uraninite, xenotime, fluorapatite, and rutile, in Q1 and Q2 overgrowths suggests that uranium mineralization might have continued during the formation of those secondary overgrowths. These results suggest that uranium mineralization in the Athabasca Basin might have been a longer lasting

event(s) than previously thought. The presence of continuous CL rims on quartz grains along annealed fractures in overlying sandstones at the Cigar Lake and McArthur River deposits provides direct evidence for late remobilization of uranium (cf., Kotzer & Kyser 1995; Fayek & Kyser 1997). This late remobilization of uranium is also supported by the common occurrences of CL patches around U-bearing minerals in reactived faults, late fractures and voids.

The EPR results on the distribution of the radiation damages in the geological profile provide further evidence that the development of radiation-induced-damages is confined to specific geological settings such as lithological boundaries, alteration haloes and the unconformity. EPR data show that the radiation damages are not evenly distributed in the basin but rather follow the pathways of U-rich fluids. Moreover, EPR spectra of altered basement rocks from the McArthur River deposit confirm CL results that basement fluids did induce any significant radiation damages and therefore were unlikely a major source of uranium. In addition, the positive correlations of EPR intensities with U and Pb contents point to possible application of this technique for age determination of uranium mineralization.

Owen (1988) suggested a potential application of CL haloes in quartz for geochronological analysis. However, the intensity of CL signals is known to be influenced by many factors (e.g., CL quenching, crystallinity; Marshall 1988 and references therein). Komuro et al. (2002) demonstrated experimentally that the intensity of radiation-damage-induced CL is positively correlated with radiation dose. Therefore, another potential application of radiation-damage-induced CL is to

determine the uranium content in mineralization fluids and/or the duration of the mineralization event(s) in the Athabasca Basin. The radiation dose of the characteristic continuous CL rims is expected to be determined by both the absolute abundance of uranium in mineralization fluids and the duration of the mineralization event. If the radiation dose of continuous CL rims can be determined independently, it may be used to provide quantitative constraints on uranium mineralization processes. Two empirical approaches to quantitatively determine radiation dose on the basis of CL intensity are: 1) analyzing CL haloes and associated U-bearing minerals and 2) analyzing CL patches and associated U-bearing minerals. In both cases, the ages of the associated U-bearing minerals must be independently and precisely known. Further study is on the way to evaluate the validity of this approach and its potential application to uranium-mineralized sedimentary basins.

Chapter 8

Conclusions

Major results of this detailed CL and EPR study on the Athabasca quartz can be summarized as follow:

- CL imaging shows that the Athabasca quartz samples are characterized by three types of bright luminescence: 1) haloes around U- and Th- bearing mineral inclusions, 2) patches in contact with U-bearing minerals in matrices and pores and 3) continuous rims with or without any U-bearing minerals. These types of CL have a constant width of ~ 35-45 μm, consistent with the maximum penetration depth of alpha particles in this minerals, and therefore record alpha-particle-induced radiation damages.

- CL spectra of the radiation-damaged areas are characterized by pronounced but broad bands in the ultraviolet (~ 350 nm) and red (~620-650 nm) regions. The ultraviolet CL band persists to 500 ˚C but is annealed out at 600 ˚C, whereas the red CL persists to at least 800 ˚C.

- EPR data reveal the presence of six paramagnetic defects: one oxygen vacancy center (E_1'), three silicon vacancy hole centers [O_2^{3-}/H^+(I), O_2^{3-}/H^+(II) and O_2^{3-}/M^+] and two O_2^- peroxy centers, in the Athabasca quartz. The silicon vacancy hole centers and the peroxy centers are shown to be concentrated in the radiation-damaged rims and fractures.

- CL and EPR data from annealing experiments suggest that the silicon vacancy hole centers and the peroxy centers are most likely responsible for the characteristic ultraviolet and red CL bands, respectively, in the radiation-damaged areas.

- CL and EPR provide direct (and visual) evidence for lithological boundaries, alteration haloes, and the unconformity being the pathway for U-bearing mineralization fluids. CL and EPR data suggest that basement fluids were not a major contributor of uranium to mineralization at McArthur River and Cigar Lake. CL evidence also provides further support that uranium was mobile during early diagenesis in the Athabasca basin and that uranium was remobilized during late fluid events.

- Potential applications of CL and EPR for geochronological studies of uranium mineralization require further investigations.

REFERENCES

AMME, M. (2002): Contrary effects of the water radiolysis products H_2O_2 upon the dissolution of nuclear fuel in natural ground water and deionized water. *Radiochimica Acta* **90**, 399-406.

BAKER, E.B. & OWEN, M.R. (1983): 800ºC threshold for cathodoluminescence in zircon and radiation-damage haloes in metaquartzite. *Geol. Soc. Am. Abstr. Orog*. **18**, 532.

BERSHOV, L.V., KRYLOVA, M.D. & SPERANSKIJ, A.V. (1978): The electron hole centers O^-–Al and Ti^{3+} as indicators for temperature conditions during regional metamorphism. *Izv. Akad. Nauk. SSSR Ser. Geol.* 113-7 *(in Russian).*

BOTIS, S.M., NOKHRIN, S., PAN, YUANMING, XU, YINGKAI, BONLI, T. & SOPUCK, V. (2005): Natural radiation damages in quartz: Part I. Correlations between cathodoluminescence colours and paramagnetic defects. *Can. Mineral*.(accepted with revision).

BRAGG, W.H. & KLEEMAN, R. (1905) Alpha particles or radium, and their loss of range passing through various atoms and molecules. *Phil. Mag.* **10**, 318-334.

BURNS, P.C., HEGHES, K.A. (2003): Studtite: the first structure of a peroxide mineral. *American Mineralogist* **88**, 1165-1168.

COHEN, M.H. & KANZIG, W. (1959): Paramagnetic resonance of oxygen in alkali halides, *Phys. Rev. Lett*. **3**, 509.

DEMARS, C., PAGEL, M., DELOULE, E. & BLANC, P. (1996):

Cathodoluminescence of quartz from sandstones: Interpretation of the UV range by determination of trace element distributions and fluid-inclusion P-T-X properties in authigenic quartz. *Am. Mineral*. **81**, 891-901.

FAYEK, M. & KYSER, T.K. (1997): Characterization of multiple fluid-flow events and rare-earth element mobility associated with formation of unconformity-type uranium deposits in the Athabasca basin, Saskatchewan. *Can. Mineral*. **35**, 627-658.

FEIGL, F.J. & ANDERSON, J.H. (1970): Defects in crystalline quartz: Electron paramagnetic resonance of E' vacancy centers associated with germanium impurities. *J. Phys. Chem. Solids* **31**, 575-596.

FRIEBELE, E.J., GRISCOM, D.L., STAPELBROEK, M. & WEEKS, R.A. (1979): Fundamental defect centres in glass: The peroxy radical in irradiated, high-purity, fused silica. *Phys. Rev. Lett.* **42**, 1346-1349.

GENTRY, R.V. (1973): Radioactive haloes. *Annual Review of Nuclear Science* **23**, 347-62.

GÖTZE, J., PLÖTZE, M. & HABERMANN, D. (1999): Defect structure and luminescence behavior of agate- results of electron paramagnetic resonance (EPR) and cathodoluminescence (CL) studies. *Mineral. Mag*. **63**,149-163.

_____ (2001): Origin, spectral characteristics and practical applications of the cathodoluminescence in quartz- a review. *Mineral. Petrol*. **71**, 225-250.

GRIFFITHS, D.R., SEELEY, N.J., CHANDRA, A.C., & SYMONS M.C.R. (1982): ESR dating of heated chert. *PACT* **9**, 399-409.

GRISCOM, D.L. (1978): Defects in amorphous insulators, *J. Non-Crystal. Solids*.**31**, 241-266.

_____ (1989): Self-trapped hole centres *Phys. Rev*. **B40**, 4224-4228.

GRISCOM, D.L. & FRIEBELE, E.J. (1981): Fundamental defect centres in glass: ^{29}Si hyperfine structure of the nonbridging oxygen hole centre and the peroxy radical in α-SiO_2. *Phys. Rev*. **B24**, 4896-4898.

HALL, M.R., RIBBE P.H. (1971): An electron microprobe study of luminescence centers in cassiterite. *American Mineralogist*, **56**: 31-44.

HANUSIAK, W.M. & WHITE, E.W. (1975): SEM cathodoluminescence for characterization of damaged and undamaged α-quartz in respirable dusts. *Scan. Elec. Micro*. 125-131.

HAYES & JENKIN (1986): Charge trapping properties of germanium in crystalline quartz. *J. Phys. C: Solid State Phys.* **19,** 6211-6219.

HOEVE, J. & QUIRT, D. (1984): Mineralization and host rock alteration in relation to clay mineral diagenesis and evolution of the Middle-Proterozoic Athabasca Basin, Northern Saskatchewan. *Sask. Res. Council, Tech. Report* **157.**

HUGHES, K.A., HELEAN, K.B, NAVROTSKY, A., BURNS, P.C., (2003): Stability of Peroxide-Containing Uranyl Minerals, *Science* **302,** 1191-1193.

IKEYA, M. (1993): New Applications of Electron Paramagnetic Resonance: ESR Dating, Dosimetry, and Spectroscopy.

JANI, M.G., BOSSOLI, R.B. & HALLIBURTON, L.E. (1983): Further

characterization of the E_1' centre in crystalline SiO_2. *Phys. Rev*. **B27**, 2285-2293.

JONES, C.E. & EMBREE, D. (1976): Correlations of the 4.77-4.28-eV luminescence band in silicon dioxide with the oxygen vacancy. *J. Appl. Phys*. **47**, 5365-5371.

KALCEFF, S.M.A., PHILLIPS, M.R.1995: Cathodoluminescence microcharacterization of the irradiation sensitive defect structure of amorphous silicon dioxide. Phys.Review B,52/5, 3122-3134.

KOMURO,K., HORICAWA, Y. & TOYODA, S. (2002): Development of radiation-damage haloes in low-quartz: cathodoluminescence measurements after He^+ implantation. *Mineral. Petrol*. **76**, 261-266.

KOTZER, T.G. & KYSER, T.K. (1995): Petrogenesis of the Proterozoic Athabasca Basin, northern Saskatchewan, Canada, and its relation to diagenesis, hydrothermal uranium mineralization and paleohydrology. *Chem. Geol*. **120**, 45-89.

KRBETSCHEK, M.R., GOTZE, J., DIETRICH A., TRAUTMANN, T. (1997): Spectral information from minerals relevant for luminescence dating. Radiat. Meas. 27/5, 695-748.

LAEMMLEIN, G.G. (1945): Coloured haloes surrounding inclusions of monazite in quartz. *Nature* **155**, 724-725.

LEPAGE, Y., CALVERT, L.D, GABE, E.J. (1980): Parameter variation in low-quartz between 94 and 298K. *J. Phys. Chem. Solid*s, **41**, 721

LEVERENTZ, H.W. 1968: An introduction to luminescence of solids, New York: Dover.

LONG J, V. P & AGRELL, S.O. 1965. The cathodoluminescence of minerals in thin section. *Mineralogical magazine* **34**, 318-326

LUFF, B.J. & TOWNSEND, P.D. (1990): Cathodoluminescence of synthetic quartz. *J. Phys. Condens. Matter* **2**, 8089-8097.

MACHEL, H.G. (2000): Application of cathodoluminescence to carbonate diagenesis, *Cathodoluminescence in geoscience*, 271 Springer Verlag Berlin Heidelberg New York.

MARFUNIN, A.S. (1979): Physics of Minerals and Inorganic materials. Springer Verlag Berlin Heidelberg.

MARSHALL, D.J. 1988: Cathodoluminescence of Geological Matherials, Academic Division of Unwin Hyman Ltd.

MARTIN, B., FL"RKE, O.W., KAINKA, E., & WIRTH, R. (1996): Electron irradiation damage in quartz, SiO_2. *Phys. Chem. Mineral.* **23**, 409-417.

MASCHMEYER, D. & LEHMANN, G. (1983): A trapped-hole centre causing rose colouration in quartz. Z. Krist 163,181-196.

MASHKOVTSEV, R.I., SCHERBAKOVA M.YA & SOLNTSEV, V.P. (1978): EPR of radiation oxygen hole centres in α-quartz. *Tr. Inst. Geol. Geofiz., Akad. Nauk. SSSR, Sib. Otd*. **385**, 78-86.

MCMORRIS, D.W. (1970): ESR detection of fossil alpha damage in quartz. *Nature* **226**: 146-148.

MELDRUM A., L.A,. BOATNER, W.J., WEBER, R.C., EWING (1998): Radiation damage in zircon and monazite. *Geochim. Cosmochim. Acta* **62**, 2509-2520.

MEUNIER, J.D., SELLIER, E. & PAGEL, M. (1990): Radiation-damage rims in quartz from uranium-bearing sandstones. *J. Sed. Petrol*. **60**, 53-58.

MITCHELL, J.P. & DENURE, D.G. (1973): A study of SiO layers on Si using cathodoluminescence spectra. *Solid State Electronics* **16**, 825-839.

MOMBOURQUETTE, M.J., TENNANT, W.C. & WEIL, J.A. (1996): EPR-NMR User's Manual. Department of Chemistry, University of Saskatchewan, Saskatoon, SK.

MORTON, R.D. (1978) Cathodoluminescence applied to uranium exploration. *Nucl. Spec*. **11**,1.

NASDALA, L., WENZEL, M., ANDRUT, M., WIRTH, R. & BLAUM, P. (2001): The nature of radiohaloes in biotite: Experimental studies and modeling. *Am. Mineral.* **86**, 498-512.

ODOM, A.L. & RINK, W.J. (1989): Giant radiation-induced colour haloes in quartz: Solution to a riddle. Science 24, 107-109.

OWEN, M.R. (1988): Radiation-damage haloes in quartz. *Geology* **16**, 529-532.

PAGEL, M., BARBIN V., BLANC P., OHNENSTTER D., (2001): Cathodoluminescence in geosciences, Springer Verlag Berlin Heidelberg New York.

PAN, Y., FLEET, M. & MACRAE, N. (1993): Late alteration in titanite (CaTiSiO5): redistribution and remobilization of rare earth elements and implications for

U/Pb and Th/Pb geochronology and nuclear waste disposal. *Geochimica et Cosmochimica Acta*, **57**, 355-367.

PASCUCCI, M.R., HUTCHISON, J.L. & HOBBS, L.W. (1983): The metamict transformation in α quartz. *Rad Effects* **74**, 219-226.

PLÖTZE, M. & WOLF, D. (1996): EPR- und TL-spektren von quartz: Bestrahlungsabhängigkeit der $[TiO_4^-/Li^+]^0$-ZENTREN. EUR. J. MINERAL. **8**: 217.

POOLE, C.P. Jr. (1967): Electron spin resonance, *John Wiley & Sons, New York*

POTTS, P.J., BOWELS, F.J.W. REED, S.J.B.,& CAVE, M.R. 1995: Microprobe techniques in earth sciences, The Mineralogy Society Series, vol. 6, Chapman and Hall, London, 419

RAMAEKERS, P. (1981): Hudsonian and Helikian basins of the Athabasca region, northern Saskatchewan. *Geol. Surv. Can. Pap*. **81-10**, 219-233.

RAMSEYER, K., BAUMANN, J., MATTER, A. & MULLIS, J. (1988): Cathodoluminescence colours of α-quartz. *Mineral. Mag*. **52**, 669-677.

REDMOND, G., CESBRON, F., CHAPOULIE, R., OHNENSTETTER, D., ROQUES-CARMES, C. & SCHVOERER, M. (1992): Cathodoluminescene applied to the microcharacterization of mineral materials: a present status in experimentation and interpretation. *Scann. Micros*. **6**, 23-68.

RINK, W.J., RENDELL, H., MARSEGLIA, E.A., LUFF, B.J, TOWNSEND, P.D. (1993): Thermoluminescence spectra of igneous quartz and hydrothermal vein quartz. *Phys Chem. Minerals* **20**: 353-361

RINNEBERG H., & WEIL J.A. (1972): EPR studies of Ti^{3+}- H^{+} centers in X-irradiated quartz, *J. Chem. Phys.*, **56**: 2019-2028

ROBBINS, M. (1983): The collector's book of fluorescent minerals. New York, Van Nostrand Reinhold.

ROSSMAN, G.R. (1994): Colored varieties of the silica minerals. *Rev Mineral* **29**: 433- 467.

SANDS, R.H. 1955: Paramagnetic resonance absorption in glass. *Phys. Rev*. **99**, 1222-1226.

SATTONNEY, G., ARDOIS, C., CORBEL, C., LUCCHINI, J.F., BARTHE, M.F., GARIDO, F., GOSSET, D., (2001): Alpha-radiolysis effects on UO_2 alteration in water. *Journal of nuclear materials* **288**, 11-19.

SEREBRENNIKOV, A.J., VALTER, A.A., MASHKOVTSEV, R.I. & SCHERBAKOVA, M.YA. (1982): The investigation of defects in shock-metamorphosed quartz. *Phys. Chem. Mineral*. **8**, 155-157.

SIEGEL, G.H. & MARRONE, M.J. (1981): Photoluminescene in as-drawn and irradiated silica optical fibers: an assessment of the role of nonbridging oxygen defect centres. *J. Non-Cryst. Solids* **45**, 235-247.

SILSBEE, R.H.(1961): Electron spin resonance in neutron-irradiated quartz, *J. Appl. Phys*. **32**, 1459-1462

SIPPEL, R.F. (1965): Simple device for luminescence petrography, *Review for Scientific Instruments* **36**, 1, 556-8

SIPPEL, R.F. (1968): Sandstone petrology, evidence from luminescence petrography. *Journal of Sedimentary Petrology* **38**, 530-54.

SIPPEL, R.F. (1971): Luminescence petrography of the Appolo 12 rocks and comparative features in terrestrial rocks and meteorites. *Proceedings of the Second Lunar Conference*, Vol.1, A.A Levinson (ed.), 247-63. Cambridge: Mass. MIT.

SMITH, J.V. & STENSTROM, R.C., (1965): Electron-excited luminescence as a petrologic tool. *J.Geol.* **73**, 627-635.

SPRUNT, E.S. & NUR A. (1979): Microcracking and healing in granites: new evidence for cathodoluminescence. *Science* **205**, 495-7.

SPRUNT, E.S. (1981): Causes of quartz cathodoluminescence colours. *Scan. Elec. Micros*. 525-535.

STAPELBROEK, M., GRISCOM, D.L., FRIEBELE, E.J. & SIGEL, G.H. Jr. (1979): Oxygen-associated trapped-hole centers in high-purity fused silica. *J. Non-Crystal. Solids.* **32**, 313-326

STENSTROM, R.C. & SMITH J.V. (1964): Electron-excited luminescence as a petrologic tool (Abst.): Geological Society of America Special Paper no.76.158.

STEVENS KALCEFF, M.A. & PHILLIPS, M.R. (1995): Cathodoluminescence microcharacterization of the defect structure of quartz. *Phys. Rev*. **B52**, 3122-3134.

VANCE, E.R., CANN, C.D. & RICHARDSON, P.G. (1986): Electron irradiation-induced amorphism of some silicates.*Rad Effects.* **98**: 71-81.

WASYLIUK, H. (2002): Petrogenesis of the kaolinite-group in the eastern

Athabasca basin of northern Saskatchewan: Applications to the uranium mineralization, unpubl., MSc. thesis, Univ. Saskatchewan.

WEEKS, R.A. (1956): Paramagnetic resonance of lattice defects in irradiated quartz. *J. Appl. Phys*. **27**, 1376-1381.

WEEKS, R.A., NELSON, C.M. (1960): Paramagnetic Spectra of E_2' Centers in Crystalline Quartz. *J. Appl. Phys*. **31**, 1555.

WEIL, J.A. (1984): A review of electron spin resonance and its applications to the study of paramagnetic defects in crystalline quartz. *Phys. Chem. Mineral*. **10**, 149-165.

WEIL, J.A. (1993):A review of EPR spectroscopy of the point defects in alpha-quartz. *The Physics and Chemistry of SiO2 and Si-SiO2 Interface* (CR Helms & BE Deal, eds), Plenum Press, New York, 131-144.

WEIL, J.A, WERTZ J. & BOLTON J. (1994) Electron paramagnetic resonance: Elementary theory and practical applications. John Wiley & Sons, New York, NY, USA.

YIP, K.L. & FOWLER, W.B. (1975): Electronic structure of E_1' centers in SiO_2. *Phys. Rev*. **B11**, 2327-2338.

YPMA, P.J. & HOCHMAN, M.B.M. (1987): A thermoluminescence study of the role of a Middle Proterozoic unconformity in controlling uranium mineralization, as shown at Eyre Peninsula, South Australia. *Bull. Mineral*. **110**, 173-186.

ZHANG, G., WASYLIUK, K. & PAN, Y. (2001): The characterization and quantitative analysis of clay minerals in the Athabasca, Saskatchewan:

Application of shortwave infrared reflectance spectroscopy. *Can. Mineral*. **39**, 1347-1363.

ZINKERNAGEL, U. (1978): Cathodoluminescence of quartz and application to sandstone petrology. *Contrib. Sed*. **8**, 1-69.

Appendix 1: List of samples characterized by CL

Sample #	Location	Depth (m)
MAC121	McArthur River Project	15
MAC121	McArthur River Project	25
MAC121	McArthur River Project	35
MAC121	McArthur River Project	45
MAC121	McArthur River Project	55
MAC121	McArthur River Project	65
MAC121	McArthur River Project	75
MAC121	McArthur River Project	85
MAC121	McArthur River Project	95
MAC121	McArthur River Project	105
MAC121	McArthur River Project	115
MAC121	McArthur River Project	125
MAC121	McArthur River Project	135
MAC121	McArthur River Project	145
MAC121	McArthur River Project	155
MAC121	McArthur River Project	165
MAC121	McArthur River Project	175
MAC121	McArthur River Project	185
MAC121	McArthur River Project	195
MAC121	McArthur River Project	205
MAC121	McArthur River Project	215
MAC121	McArthur River Project	225
MAC121	McArthur River Project	235
MAC121	McArthur River Project	245
MAC121	McArthur River Project	255
MAC121	McArthur River Project	265
MAC121	McArthur River Project	275
MAC121	McArthur River Project	285
MAC121	McArthur River Project	295
MAC121	McArthur River Project	305
MAC121	McArthur River Project	315
MAC121	McArthur River Project	325
MAC121	McArthur River Project	335
MAC121	McArthur River Project	345
MAC121	McArthur River Project	355
MAC121	McArthur River Project	365
MAC121	McArthur River Project	375
MAC121	McArthur River Project	385
MAC121	McArthur River Project	395
MAC121	McArthur River Project	405
MAC121	McArthur River Project	415
MAC121	McArthur River Project	425
MAC121	McArthur River Project	435
MAC121	McArthur River Project	445
MAC135A	McArthur River Project	16
MAC135A	McArthur River Project	26

MAC135A	McArthur River Project	36
MAC135A	McArthur River Project	66
MAC135A	McArthur River Project	76
MAC135A	McArthur River Project	86
MAC135A	McArthur River Project	96
MAC135A	McArthur River Project	106
MAC135A	McArthur River Project	116
MAC135A	McArthur River Project	126
MAC135A	McArthur River Project	136
MAC135A	McArthur River Project	146
MAC135A	McArthur River Project	156
MAC135A	McArthur River Project	166
MAC135A	McArthur River Project	176
MAC135A	McArthur River Project	186
MAC135A	McArthur River Project	196
MAC135A	McArthur River Project	206
MAC135A	McArthur River Project	216
MAC135A	McArthur River Project	226
MAC135A	McArthur River Project	236
MAC135A	McArthur River Project	246
MAC135A	McArthur River Project	256
MAC135A	McArthur River Project	266
MAC135A	McArthur River Project	276
MAC135A	McArthur River Project	286
MAC135A	McArthur River Project	296
MAC135A	McArthur River Project	306
MAC135A	McArthur River Project	316
MAC135A	McArthur River Project	326
MAC135A	McArthur River Project	346
MAC135A	McArthur River Project	356
MAC135A	McArthur River Project	366
MAC135A	McArthur River Project	368.8
ML-7	Moon Lake Project	411.3
ML-8	Moon Lake Project	412.7
ML-9	Moon Lake Project	526.3
PK-15	Park Creek Project	81
PK-19	Park Creek Project	117
PK-25	Park Creek Project	70
WDG1-44A	Cigar Lake Mine	270.8
WDG1-46	Cigar Lake Mine	309.2
WDG1-8	Cigar Lake Mine	414.3
DDH-753	Key Lake Mine	109
DDH-930	Key Lake Mine	249
DDH-940	Key Lake Mine	139

Appendix 2: List of samples characterized by EPR

Sample #	Microwave power (dB)	Folder#	File on CD-rom#
H737.58 (RT)	1	H737.58 RT	H758RT1
H737.58 (RT)	10	H737.58 RT	H758RT10
H737.58 (RT)	15	H737.58 RT	H758RT15
H737.58 (RT)	20	H737.58 RT	H758RT20
H737.58 (RT)	30	H737.58 RT	H758RT30
H737.58(100C)	5	H737-T dep.	H58T15
H737.58(100C)	10	H737-T dep.	H58T110
H737.58(100C)	15	H737-T dep.	H58T115
H737.58(100C)	20	H737-T dep.	H58T120
H737.58(100C)	30	H737-T dep.	H58T130
H737.58(200C)	5	H737-T dep.	H58T25
H737.58(200C)	10	H737-T dep.	H58T210
H737.58(200C)	15	H737-T dep.	H58T215
H737.58(200C)	20	H737-T dep.	H58T220
H737.58(200C)	30	H737-T dep.	H58T230
H737.58(300C)	5	H737-T dep.	H58T35
H737.58(300C)	10	H737-T dep.	H58T310
H737.58(300C)	15	H737-T dep.	H58T315
H737.58(300C)	20	H737-T dep.	H58T320
H737.58(300C)	30	H737-T dep.	H58T330
H737.58(400C)	5	H737-T dep.	H58T45
H737.58(400C)	10	H737-T dep.	H58T410
H737.58(400C)	15	H737-T dep.	H58T415
H737.58(400C)	20	H737-T dep.	H58T420
H737.58(400C)	30	H737-T dep.	H58T430
H737.58(450C)	5	H737-T dep.	H58T455
H737.58(450C)	10	H737-T dep.	H58T4510
H737.58(450C)	15	H737-T dep.	H58T4515
H737.58(450C)	20	H737-T dep.	H58T4520
H737.58(450C)	30	H737-T dep.	H58T4530
H737.58(500C)	5	H737-T dep.	H58T55
H737.58(500C)	10	H737-T dep.	H58T510
H737.58(500C)	15	H737-T dep.	H58T515
H737.58(500C)	20	H737-T dep.	H58T520
H737.58(500C)	30	H737-T dep.	H58T530
H737.58(550C)	5	H737-T dep.	H58T555
H737.58(550C)	10	H737-T dep.	H58T5510
H737.58(550C)	15	H737-T dep.	H58T5515
H737.58(550C)	20	H737-T dep.	H58T5520
H737.58(550C)	30	H737-T dep.	H58T5530
H737.58(600C)	1	H737-T dep.	H58T61
H737.58(600C)	3	H737-T dep.	H58T63

H737.58(600C)	5	H737-T dep.	H58T65
H737.58(600C)	10	H737-T dep.	H58T610
H737.58(700C)	1	H737-T dep.	H58T71
H737.58(700C)	3	H737-T dep.	H58T73
H737.58(700C)	5	H737-T dep.	H58T75
H737.58(700C)	10	H737-T dep.	H58T710
H737.58(800C)	3	H737-T dep.	H58T83
H737.58(800C)	5	H737-T dep.	H58T85
H737.58(800C)	10	H737-T dep.	H58T810
H737.58 before HF	5	H737.58- HF	H7BF5
H737.58 before HF	10	H737.58- HF	H7BF10
H737.58 before HF	15	H737.58- HF	H7BF15
H737.58 after 2h HF	5	H737.58- HF	H7AF5
H737.58 after 2h HF	10	H737.58- HF	H7AF10
H737.58 after 2h HF	15	H737.58- HF	H7AF15
H737.58 after 4h HF	5	H737.58- HF	H7AF25
H737.58 after 4h HF	10	H737.58- HF	H7AF210
H737.58 after 4h HF	15	H737.58- HF	H7AF215
H737.58 after 8h HF	5	H737.58- HF	H7AF45
H737.58 after 8h HF	10	H737.58- HF	H7AF410
H737.58 after 8h HF	15	H737.58- HF	H7AF415
106	10	HF-8h	106-10
106	20	HF-8h	106-20
106	30	HF-8h	106-30
366	10	HF-8h	366-10
366	20	HF-8h	366-20
366	30	HF-8h	366-30
2217-254	10	HF-8h	254-10
2217-255	20	HF-8h	254-20
2217-256	30	HF-8h	254-30
MAC223-655	10	HF-8h	655-10
MAC223-656	20	HF-8h	655-20
MAC223-657	30	HF-8h	655-30
106	10	before HF	106-10
106	20	before HF	106-20
106	30	before HF	106-30
366	10	before HF	366-10
366	20	before HF	366-20
366	30	before HF	366-30
2217-254	10	before HF	254-10
2217-255	20	before HF	254-20
2217-256	30	before HF	254-30
MAC223-655	10	before HF	655-10
MAC223-656	20	before HF	655-20
MAC223-657	30	before HF	655-30
MAC121-385	10	121-385	385-10
MAC121-385	20	121-386	385-20
MAC121-385	30	121-387	385-30

MAC121-465	10	121-465	465-10
MAC121-465	20	121-466	465-20
MAC121-465	30	121-467	465-30
MAC121-476	10	121-476	476-10
MAC121-476	20	121-477	476-20
MAC121-476	30	121-478	476-30
MAC121-25	5	121-5	25
MAC121-125	5	121-6	125
MAC121-265	5	121-7	268
MAC121-368.8	5	121-8	368.8
MAC135A-106	15	MAC135A	106-15
MAC135A-146	15	MAC135A	146-15
MAC135A-186	15	MAC135A	186
MAC135A-236	15	MAC135A	236
MAC135A-286	15	MAC135A	286
MAC135A-356	15	MAC135A	356
MAC135A-366	15	MAC135A	366
MAC223-125	10	MAC223	125-10
MAC223-125	20	MAC223	125-20
MAC223-125	30	MAC223	125-30
MAC223-225	10	MAC223	225-10
MAC223-225	20	MAC223	225-20
MAC223-225	30	MAC223	225-30
MAC223-355	10	MAC223	355-10
MAC223-355	20	MAC223	355-20
MAC223-355	30	MAC223	355-30
MAC223-475	10	MAC223	475-10
MAC223-475	20	MAC223	475-20
MAC223-475	30	MAC223	475-30
MAC223-635	10	MAC223	635-10
MAC223-635	20	MAC223	635-20
MAC223-635	30	MAC223	635-30
MAC223-655	10	MAC223	655-10
MAC223-655	20	MAC223	655-20
MAC223-655	30	MAC223	655-30